Investigation on the Structural, Optical, Dielectric and Ferroelectric Properties of Sol-Gel Synthesized Barium Titanate and Strontium Titanate Thin Films

Thesis

Submitted in partial fulfilment of the requirements for the degree of

DOCTOR OF PHILOSOPHY

By

N. DEEPAK KUMAR

Under the supervision of

Dr. M. N. KAMALASANAN

BIRLA INSTITUTE OF TECHNOLOGY AND SCIENCE
PILANI (RAJASTHAN) INDIA

1995

BIRLA INSTITUTE OF TECHNOLOGY AND SCIENCE
PILANI (RAJASTHAN)

CERTIFICATE

This is to certify that the thesis entitled " Investigation onthe structural, optical, dielectric and ferroelectric properties of sol-gel synthesized barium titanate and strontium titanate thin films " and submitted by N. Deepak Kumar (ID. No. 92PZYF011) for the award of Ph.D. Degree of the Institute, embodies original work done by him under my supervision.

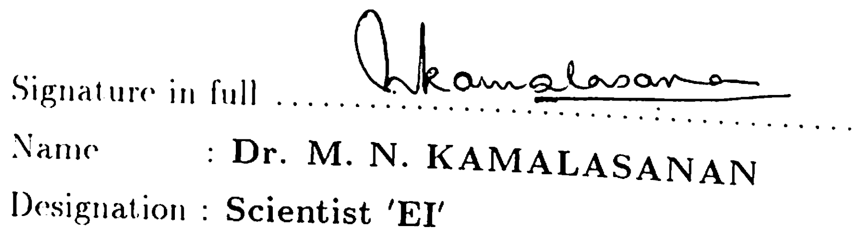

Signature in full ....

Name : **Dr. M. N. KAMALASANAN**

Designation : **Scientist 'EI'**

Date : 22-9-95

Contents

Acknowledgements xv

Abstract xvii

1 Sol-Gel Technique for Synthesis of Advanced Materials **1**

1.1 Historic Background of Sol-Gel Process 2

1.2 Sol-gel Process in the Fabrication of Ferroelectric Thin Films - A Survey 2

1.3 Different Stages in Sol-gel Processing of Materials 6

1.3.1 Hydrolysis 8

1.3.2 Condensation and Polymerization 8

1.3.3 Gelation 11

1.3.4 Aging 11

1.3.5 Drying 12

1.4 Solution Chemistry of Metal Alkoxide Precursors 12

1.4.1 Mechanism of hydrolysis and Condensation 13

1.4.2 Role of Catalyst 15

1.4.3 Chemical Modification 17

1.5 Sol-Gel Processing Applied to Thin Film Technology 19

1.6 Effect of Branching and Condensation Rate on Film Structure 20

1.7 Application of Sol-gel Processed Thin films 21

References 23

2 Ferroelectric Materials and Their Applications - A Review **30**

2.1 Ferroelectricity and related materials 30
2.2 Structural aspects of the ferroelectric phase transition 33
2.3 Symmetry and ferroelectric phase transition 37
2.3.1 Landau theory of the phase transition in ferroelectrics 38
2.3.2 Second order phase transition 38
2.3.3 First order phase transition 40
2.4 Ferroelectric Thin Films for High Tech Applications 41
2.4.1 Ferroelectric non-volatile memories 41
2.4.2 Integrated optic total internal reflection switch (TIR) 45
2.4.3 Pyroelectric Infrared detector (IR optical FET) 45
2.4.4 Erasable/Rewritable Optical Disc 45
2.5 Desired features of ferroelectric thin films for electronic applications 47
2.5.1 Dielectric breakdown 47
2.5.2 Leakage Current 48
2.6 Reliability of Time Dependent Physical Properties 48
2.6.1 Aging 48
2.6.2 Fatigue 50
2.6.3 Time dependent Dielectric breakdown 50
2.7 Advances in processing of Ferroelectric Thin Films 50
References 54

3 Experimental Techniques and Characterization **59**
3.1 Preparation of Multicomponent Oxide Thin Films of $BaTiO_3$ and $SrTiO_3$ by Sol-gel Process 59
3.1.1 Preparation of $BaTiO_3$ sol from Ti(OPr)4 and barium 2-ethyl hexanoate (EH precursor) 61

3.1.2 Preparation of $BaTiO_3$ sol from $Ti(OC_3H_7)_4$ and barium hydroxide (ME precursor) . . . 62
3.1.3 Preparation of $SrTiO_3$ sol from strontium 2 ethyl hexanoate and $Ti(OC_3H_7)_4$ . . . 62
3.2 Sample Preparation . . . 62
3.2.1 Sample preparation for structural and optical characterization 63
3.2.2 Preparation of MIM and MIS structures . . . 63
3.3 Thickness Measurements . . . 65
3.4 Characterization of Sol-gel Derived $BaTiO_3$ and $SrTiO_3$ Thin Films . 65
3.4.1 Scanning Electron Microscopy (SEM) . . . 65
3.4.2 X-ray Diffraction Analysis . . . 66
3.4.3 Auger electron spectroscopic studies on $BaTiO_3$ thin films . . 70
3.5 Optical Characterization: UV-Visible specroscopy . . . 73
3.5.1 Determination of Refractive Index and Thickness from Optical Transmission Spectra . . . 73
3.6 Determination of Optical Band Gap . . . 76
3.7 Fourier Transform Infrared (FTIR) Spectroscopy . . . 77
3.8 Electrical and Dielectric Measurements . . . 79
3.8.1 Frequency dependence of dielectric properties . . . 79
3.8.2 Temperature dependence of dielectric properties . . . 81
3.8.3 Frequency dependent C-V characteristics . . . 81
3.8.4 I-V and I-T measurements . . . 85
3.9 Ferroelectric Measurements . . . 85
3.9.1 Polarization reversal mechanism . . . 85
3.9.2 P-E hysteresis . . . 86
3.9.3 C-V butterfly loop . . . 89

3.10 Preferred Orientation in $BaTiO_3$ Thin Films Grown on Single Crystal $SrTiO_3$ (100) Substrates. 91

References 93

4 Structural and Microstructural Evolution in $BaTiO_3$ and $SrTiO_3$ Precursor Thin Films 95

4.1 Studies on Sol-gel derived Barium Titanate Thin Film 96

4.1.1 FTIR Studies 96

4.1.2 X-ray diffraction studies 100

4.1.3 Optical Studies 103

4.1.4 Scanning electron microscopy 108

4.2 Structural and Microstructural evolution in $SrTiO_3$ thin films made by sol-gel process 112

4.2.1 FTIR studies 112

4.2.2 Optical Properties: (UV-Visible) 113

4.2.3 X-ray diffraction studies 120

5 Electrical and Dielectric Properties of $BaTiO_3$ Thin Films Grown by Sol-Gel Process 125

5.1 Dielectric and electrical properties of polycrystalline $BaTiO_3$ thin films 126

5.1.1 Dielectric properties of $BaTiO_3$ thin films on stainless steel substrates 126

5.1.2 Effect of humidity on the dielectric behaviour of $BaTiO_3$ thin films on platinum substrates 128

5.1.3 Electrical conductivity in crystalline $BaTiO_3$ thin films 132

5.1.4 Mechanism of conduction in sol-gel $BaTiO_3$ thin film on platinum substrates 139

5.2 Dielectric and electrical properties of amorphous $BaTiO_3$ thin films in MIS configuration 141

5.2.1 C-V Characteristics of amorphous $BaTiO_3$ thin films on p type silicon . . . 142

5.2.2 I-V characteristics . . . 146

5.3 Ferroelectric Properties of $BaTiO_3$ Films . . . 150

5.3.1 P-E Hysteresis loop measurements . . . 150

5.3.2 C-V butterfly loop . . . 153

References . . . 156

6 Dielectric and Electrical Properties of Sol-Gel Derived $SrTiO_3$ Thin Films 158

6.1 M-I-M Capacitor Structure based on polycrystalline $SrTiO_3$ thin films on stainless steel substrates . . . 158

6.1.1 Dielectric Properties . . . 159

6.1.2 Frequency dependence of conductivity . . . 162

6.1.3 C-V Characteristics . . . 167

6.2 Conduction Mechanism in sol-gel processed $SrTiO_3$ Thin Films . . . 167

6.3 MIS structure based on $SrTiO_3$ thin films on p-type silicon . . . 173

6.3.1 C-V characteristics of $SrTiO_3$ thin films in MIS configuration 173

6.3.2 I-V characteristics . . . 175

References . . . 179

7 Conclusion 181

List of Figures

1.1 Different stages in the sol-gel processing of thin films, ceramics and glasses. 7

1.2 Formation of rings and chains by a bifunctional ligand to form oligomers. 9

1.3 Formation of fractal polymers by the branching of polyfunctional monomers with $f > 2$ (computer simulation). 10

1.4 Schematic representation of a gel structure. 10

1.5 Structure of different titanium alkoxide oligomers. 16

2.1 Typical ferroelectric hysteresis loop of Applied electric field versus polarization. 30

2.2 The perovskite crystal structure of $BaTiO_3$ 30

2.3 Projection of spontaneaous polarization $BaTiO_3$ onto one edge of the unit cell as a function of temperature. 35

2.4 Approximate ionic displacements in the cubic tetragonal distortion in $BaTiO_3$ 35

2.5 Variation of potential energy of Ti^{4+} ion along the c-axis. 35

2.6 (a) Surface charge associated with spontaneous polarization (b) Formation of 180° domains to minimize electrostatic energy. 35

2.7 Variation of saturation polarizarion and relative permittivity as function of temperature for second order phase transition. 38

2.8 Variation of saturation polarizarion and relative permittivity as function of temperature for first order phase transition. 38

2.9 (Top) A cross-sectional view of Si-CMOS device with superimposed FE thin film switching memory and (Bottom) Schematic circuit of memory structure. 12

2.10 Configuration of TIR switch using a PLZT/sapphire structure. 12

2.11 Schematic structure of IR-OPFET based on ferroelectric $PbTiO_3$ . . . 15

2.12 Schematic of Erasable/rewritable optical disc with PLZT ferroelectric thin film. 15

3.1 Flow chart showing the different stages in the fabrication of $BaTiO_3$ and $SrTiO_3$ thin films by sol-gel process. 49

3.2 Scanning electron micrographs of $BaTiO_3$ thin films deposited on Pt substrates and annealed at (a) 700 °C and (b) 750 °C for 15 minutes. 65

3.3 Scanning electron micrographs of $SrTiO_3$ thin films deposited on (a) silicon wafer (100) and (b) stainless steel by sol-gel process and annealed at 650 °C for 15 minutes. 65

3.4 XRD pattern of $BaTiO_3$ thin film deposited on silicon wafer (100). Tetragonal splitting is seen at higher θ values. 67

3.5 XRD pattern of $SrTiO_3$ thin film deposited on fused quartz. 67

3.6 Auger electron spectra of $BaTiO_3$ thin films deposited on Pt strip after etching for (a) 2 min., (b) 20 min. and (c) 25 min. 69

3.7 Auger depth profile of $BaTiO_3$ thin films as a function of etching time. 70

3.8 Schematic representation of a dielectric thin film of complex refractive index $\eta = n - ik$. 72

3.9 optical transmission spectra of polycrystalline $BaTiO_3$ thin film on fused silica subtrate. The dotted lines shows the envelope curve for calculating the optical constants by the method adopted by Manifacier et al [4]. 72

3.10 Optical transmission and absorption spectra of $SrTiO_3$ thin film on fused silica substrate made by sol-gel process. 76

3.11 Determination of band gap from the optical data. 76

3.12 A typical frequency dependence of total polarization of a dielectric material. 78

3.13 Typical C-V characteristics of an MIS capacitor. 78

3.14 Representation of accumulation, depletion, inversion and deep depletion during the voltage sweep in the C-V characteristics of an MIS capacitor. 80

3.15 Representation of sweep rate dependence of C-V characteristics. . . . 81

3.16 Effect of series resistance in the C-V characteristics of an MIS capacitor. 81

3.17 Different stages in the P-E hysteresis cycle of a ferroelectric material. 85

3.18 Typical Sawyer-Tower circuit for measuring P-E hysteresis loop. . . . 86

3.19 Typical hysteresis loop due to (a) a conducting sample (b) an insulating sample. 86

3.20 Block diagram of a modified Sawyer-Tower cicuit with compensation for sample conductivity and capacitance. 88

3.21 XRD spectra showing preferred orientation in sol-gel grown $BaTiO_3$ thin film on single crystal $SrTiO_3$ (100). 90

3.22 Scanning electron micrograph of $BaTiO_3$ thin film grown on single crystal $SrTiO_3$ (100). 90

4.1 FTIR spectrum of $BaTiO_3$ precursor thin film (EH precursor) annealed at different temperatures. 94

4.2 FTIR spectrum of $BaTiO_3$ thin film (ME precursor) annealed at different temperatures. 96

4.3 XRD spectra of $BaTiO_3$ precursor (EH) thin films coated on single crystal silicon (100) and annealed at (a) 450°C , (b) 600 °C and (c) 800°C 98

4.4 XRD spectra of $BaTiO_3$ precursor (ME) thin films coated on single crystal silicon (100) and annealed at (a) 350°C , (b) 450 °C , (c) 600 °C and (d) 800°C 99

4.5 Variation of thickness of $BaTiO_3$ precursor thin films on fused silica substrate with annealing temperature (a) EH precursor and (b) ME precursor. 101

4.6 Variation of refractive index of $BaTiO_3$ thin films on fused silica substrate with annealing temperature (a) EH precursor and (b) ME precursor. 104

4.7 Variation of band gap E_g with annealing temperature of $BaTiO_3$ precursor thin films on fused silica substrate (a) EH precursor and (b) ME precursor. 106

4.8 Optical transmission spectra of $BaTiO_3$ thin film on fused silica substrate annealed at (a) 400°C and (b) 600°C 106

4.9 Scanning electron micrograph of $BaTiO_3$ precursor thin films on fused silica substrate. (a) & (b) made using EH precursor and annealed at 450°C & 800°C , respectively and (c) & (d) made using ME precursor and annealed at 450°C & 800°C , respectively. 107

4.10 FTIR spectra of thin films of (a) $Ti(OC_3H_7)_4$ chelated using 1 mole acetyl acetone (b) $Sr(C_7H_{15}COO)_2$ at room temperature and (c) $Sr(C_7H_{15}COO)_2$ at 400°C 111

4.11 FTIR spectra $SrTiO_3$ thin film annealed at different temperatures. . . 112

4.12 Variation of thickness with annealing temperature of $SrTiO_3$ thin film on fused silica substrate. 114

4.13 Variation of refractive index with annealing temperature of $SrTiO_3$ thin film on fused silica substrate. 115

4.14 Wavelength dispersion curve of $SrTiO_3$ thin film on fused silica substrate. 115

4.15 Plot representing Didominico-Wemple single electronic model for interband transition. 116

4.16 Transmission spectra of $SrTiO_3$ thin film on fused silica substrate annealed at (a) 400°C and (b) 550°C 116

4.17 XRD spectra of $SrTiO_3$ thin film on fused silica substrate annealed at diffrent temperatures. 118

5.1 Variation of ϵ' and ϵ'' as a function of frequency of $BaTiO_3$ thin film made on stainless steel substrate. Inset : Variation of ϵ' with film thickness for frequencies (1) 1 kHz, (2) 10 kHz and (c) 100 kHz. . . . 123

5.2 Variation of ϵ' with temperature for various frequencies in ambient air. Dotted lines represent the corresponding cooling down curves. 125

5.3 Variation of ϵ'' with temperature for various frequencies in ambient air. 126

5.4 Variation of ϵ' as a function of the time for which oxygen has been flown through the sample holder. 127

5.5 Variation of ϵ'' as a function of the time for which oxygen has been flown through the sample holder. 127

5.6 Variation of ϵ' as function of temperature for $BaTiO_3$ on Pt for different frequencies in dry conditions. 129

5.7 Variation of ϵ'' as function of temperature for $BaTiO_3$ on Pt for different frequencies in dry conditions. 130

5.8 Dependence of ϵ' and ϵ'' as a function of frequency of ac signal at different temperatures. 131

5.9 Frequency dependence of ac conductivity of $BaTiO_3$ thin film on Pt substrate. 132

5.10 Variation of conductivity with $1000/T$ for various frequencies. 134

5.11 (a) Schematic diagram of the cross section of $BaTiO_3$ thin film in MIM configuration and (b) the equivalent electrical circuit. 134

5.12 C-V characteristics of MIS capacitor based on amorphous $BaTiO_3$ thin film measured at a signal frequency of (a) 100 Hz and (b) 10 kHz respectively. 139

5.13 Dielectric dispersion in amorphous $BaTiO_3$ thin film (a) variation of capacitance with frequency and (b) variation of loss factor with frequency. 110

5.14 V-I characteristics of amorphous $BaTiO_3$ on silicon substrate for different thicknesses (a) 140 nm and (b) 280 nm. 114

5.15 Plot representing Poole-Frenkel conduction mechanism. 115

5.16 P-E hysteresis loop for $BaTiO_3$ thin film on Pt:Si substrate without compensation. 147

5.17 P-E hysteresis loop for $BaTiO_3$ thin film on Pt:Si substrate with compensation. 147

5.18 P-E hysteresis loop for $BaTiO_3$ thin film on Pt:Si substrate with compensation at different fields. 148

5.19 P-E hysteresis loop for $BaTiO_3$ thin film on Pt:Si substrate without compensation under humid conditions. 148

5.20 C-V butterfly loop for a 1μm $BaTiO_3$ thin film on Pt:Si substrate at 1 MHz. 150

5.21 C-V characteristics of a 2.5μm $BaTiO_3$ thin film on Pt substrate at (a) 10 kHz, (b) 100 kHz and (c) 1 MHz. 151

6.1 Variation of dielectric constant of $SrTiO_3$ thin film on stainless steel substrate with thickness for different frequencies. 156

6.2 Variation of ϵ' and $\tan\delta$ with frequency for $SrTiO_3$ thin film on stainless steel substrate. 156

6.3 Variation of ϵ' and $\tan\delta$ for $SrTiO_3$ thin film on stainless steel substrate with temperature at various frequencies. 158

6.4 Variation of ϵ'' with temperature at various frequencies (1) 2 MHz, (2) 1 MHz, (3) 250 kHz, (4) 100 kHz, (5) 25 kHz, (6) 10 kHz, (7) 2.5 kHz and (8) 1 kHz. 159

6.5 Relaxation time as a function of temperature. 160

6.6 Variation of conductivity as a function of frequency. 161
6.7 Variation of conductivity as a function of temperature. 163
6.8 C-V characteristics of $SrTiO_3$ thin film on stainless substrate in MIM configuration. 164
6.9 (a) Model of MIM capacitor based on $SrTiO_3$ thin film showing crystalline and amorphous regions and (b) equivalent network of crystalline regions and barriers. 167
6.10 C-V characteristics of $SrTiO_3$ MIS thin film capacitor at a frequency of 10 kHz. 169
6.11 Dielectric dispersion in a $SrTiO_3$ MIS capacitor (a) variation of capacitance with frequency and (b) variation of loss factor with frequency. 171
6.12 I-V characteristics of a 200 nm thick $SrTiO_3$ MIS capacitor. 172
6.13 Curve representing Poole-Frenkel conduction mechanism in $SrTiO_3$ MIS capacitor. 173

List of Tables

1.1 Positive partial charge $\delta(M)$ for metals in various alkoxides. 15

2.1 Different types of ferroelectric crystals 33

2.2 Some ferroelectric materials, their applications and basic phenomena utilized. 42

2.3 History of FE thin film fabrication techniques, their comparison and important features 51

4.1 comparison of the properties of $BaTiO_3$ thin films deposited using barium 2-ethyl hexanoate (EH precursor) and barium hydroxide dissolved in 2-methoxy ethanol (ME precursor) as two different barium sources 111

Acknowledgements

I wish to express my deep sense of gratitude towards my research supervisor, Dr. M. N. Kamalasanan, for his encouragement, keen interest, many stimulating discussions, and able guidance during the course of my research. I am also grateful to Dr. Subhas Chandra for his encouragement and timely support as the group leader of the Display Devices Division.

I want to thank Professor E. S. Rajagopal, Director, National Physical Laboratory, New Delhi for his interest in my research work and for providing the laboratory facilities available for me to pursue this work.

I wish to express my sincere thanks to Dr. A.M. Biradar, Dr. S. S. Bawa, Dr. S. A. Agnihotri, Dr. S. C. K. Misra, and Dr. B. D. Malhotra for their useful criticism and valuable suggestions. I am also thankful to Prof. L. K. Maheswari, Prof. K. E. Raman and other faculty members of the Instrumentation and Material science division, BITS, Pilani and Prof. P. K. C. Pillai of Physics Department, IIT, Delhi.

I am highly indebted to V. N. Moorty and E.P. Haridas for their friendship, encouragement, help, and selfless devotion during my entire Ph.D. thesis writing. I am also grateful to Deepak Varandhani, Indu Dhingra, and Kapil Bajaj for their sincere support.

I will like to acknowledge the useful discussions and help in acquiring experimental data by R. N. Sharma, Pavas Asthana, Manoj K. Ram, R. Kumaran, Manju Verghese, C. Mukerjee, K. Chakraborty, D. Sarangi, S. Dhara, and S. Saha.

I am thankful to X-ray and Electron Microscopy Division at NPL for their help in the present work. I wish to thank Dr. Ravi Mehrothra and other staffs of Central Computer Facility at NPL. My thanks are also due to NPL library and workshop staffs. I express my gratefulness to the Council of Scientific and Industrial Research (CSIR) for awarding me with a junior and senior research fellowship.

Finally, I express my indebtedness to my parents and family members for being with me at hard times and their encouragement through these years.

N. Deepak Kumar

Abstract

Sol-gel process is emerging as one of the most important material processing technologies due to its versatility in producing entirely new class of materials. Sol-gel process is capable of producing new phases of materials and a veriety of composite materials from ceramics, organics, inorganics, polymers and metals. These sol-gel processed materials possess unique properties which can be useful in applied technologies. Sol-gel process has been extensively used in the past decade for the developement of ceramics, glasses and thin films. Sol-gel process gives better structural and microstructural control over the production of these materials there by attaining better reproducibility and homogeneity.

One of the major activity in the field of sol-gel research is the fabrication of thin films. A variety of thin film coating for electronic, optical, sensor, protective and mechanical applications have been realised using sol-gel process. Fabrication of ferroelectric thin films for application in microelectronics and integrated optics is gaining more interest in recent times. A large number of ferroelectric thin films such as $PbTiO_3$, $Pb(Zr,Ti)O_3$, $BaTiO_3$, $SrTiO_3$, $LiNbO_3$, $(Sr,Ba)Nb_2O_6$, $KNbO_3$ has been deposited on a variety of substrate using sol-gel process by researchers world-wide.

This thesis is about the fabrication of ferroelectric thin films of $BaTiO_3$ and $SrTiO_3$ on different substrates using sol-gel process and their characterization. The content of the different chapters of this thesis is summerized in the following pragraphs.

A formal introduction to the different aspects of sol-gel process is depicted in chapter 1. A general survey of the different sol-gel processed ferroelectric thin films made by other workers in the field and thier major achievements are discussed. The principle of sol-gel process and the different stages involved in the processing of thin films are also summerised. The chapter also deals with the different physical and chemical changes occuring during the sol-gel process. The chapter gives a brief description about the rheological nature of the hydrolysed and condensed products

during the films formation. Finally the application of the sol-gel process in the field of thin film fabrication is discussed.

Ferroelectric materials in general and their important applications in different emerging technologies are reviewed in chapter 2. The origin of ferroelectricity in materials and how they depend on the structure of the materials are discussed in this chapter. A brief survey has been done in this chapter about the devices which utilizes the ferroelectric behaviour of materials. The devices which has been developed on a commercial basis and those developed to a prototype are also discussed. The commonly used ferroelectric thin film fabrication techniques such as sputtering, laser ablation and chemical vapor deposition techniques are discussed for comparison with the sol-gel process.

Chapter 3 is about the sol-gel fabrication of ferroelectric thin films of $BaTiO_3$ and $SrTiO_3$ used in the present study, the experimental techniques and the characterization of the above films. Thin films of $BaTiO_3$ and $SrTiO_3$ are made using alkoxide and metal salt sol-gel route. Thin films of $BaTiO_3$ are made from two different sets of precursors and are characterized. X-ray diffraction, Scanning Electron Microscopy, Auger Electron Spectroscopy, Fourier Transform Infrared Spectroscopy, and Optical Spectroscopy are the major characterization techniques used. X-ray diffraction studies on the $BaTiO_3$ thin films made from titanium isopropoxide and barium 2-ethyl hexanoate shows a tetragonal structure, which is the requirement for ferroelectricity in these films. $BaTiO_3$ thin films made from titanium isopropoxide and barium hydroxide dissolved in 2-methoxyethanol crystallised in the cubic form. The comparitive study of the $BaTiO_3$ thin films made from the two sets of precursors are discussed in chapter 4. The ferroelectricity in the $BaTiO_3$ thin films are confirmed from the P-E hysteresis measurements made on $BaTiO_3$ M-I-M capacitors using Sawyer-Tower circuit.

The structural and microstructural evolution in $BaTiO_3$ thin films grown from titanium isopropoxide and barium 2-ethyl hexanoate and titanium isopropoxide and barium hydroxide dissolved in 2-methoxyethanol are studied in chapter 4. The microcrystals of $BaTiO_3$ grown above 550^oC from the first set of precursor is found to be tetragonal in nature and that from the later crystallized in cubic form. FTIR analysis

of the above precursor systems in the thin film form are coupled with the uv-visible spectroscopy analysis to investigate on the evolution in the precursor structure with heat treatment of the thin films to form the final ceramic oxide thin films. Scanning electron microscopic studies of these thin films are done to reveal the microstructure of the final product. $SrTiO_3$ thin films are also subjected to similar studies to identify the general behaviour of sol-gel grown dielectric thin films.

The electrical, dielectric and ferroelectric properties of the so-gel deposited $BaTiO_3$ thin films are studied in chapter 5. The substrates used in this study are stainless steel, silicon wafer, platinum plate, and platinized silica. The films grown on stainless steel show electrode barrier effect and has large dielectric dispersion. Thin films of barium titanate made on platinum plates are very sensitive to the ambient humidity. The effect of humidity on the dielectric measurements are confirmed by carrying out the measurements in both ambient and humid free conditions. The measurements show that the presence of moisture gives rise to large dielectric losess. The a.c conduction mechanism in the thin films of $BaTiO_3$ on platinum plates are found to be frequency dependent and are attributed to the bound charge carriers trapped in the intercrystalline barriers. The electron micrograph of the films show the presence of a mixed amorphous and crystalline phases in these films. A model for the M-I-M $BaTiO_3$ capacitor based on the above observations has been proposed and the electrical properties are in good agreement with the model. The ferroelectric properties of the $BaTiO_3$ thin films are done on the samples made on platinized silicon wafer. The measurements were both done in ambient atmospheric and in humid free conditions. The sample conductivity and capacitance are compensated in the measurements using a modified Sawyer-Tower circuit. The M-I-S capacitor configuration based on amorphous $BaTiO_3$ thin films are investigated in this chapter to identify their use in Dynamic Random Access Memory (DRAM) devices as a substitute for conventional silicon dioxide capacitors. The large dielectric constant of $BaTiO_3$ may make it a better choice for such devices.

In chapter 6 the electrical and dielectric properties of sol-gel grown $SrTiO_3$ thin films on stainless steel and silicon wafer are discussed. The M-I-M thin film capacitor based on $SrTiO_3$ shows little dielectric dispersion in the frequancy range investigated

in the work. They also have a very small temperature coefficient of dielectric constant. This makes $SrTiO_3$ an excellent candidate for precesion applications regardless of the changes in the environment. The electrical properties of the sol-gel grown $SrTiO_3$ thin films were found to depend on the microstructure of the film. The films used in the present study has a crystalline phase embeded in the amorphous phase as seen from the electron micrographs. The electrical conduction in these films were explained on the basis of the above structure. $SrTiO_3$ thin films are also investigated in the M-I-S configuration. The analysis showed that they can be better substitute of conventional dielectric layers used in the present memory elements.

The last chapter is used to present the major conclusions derived from the present work. The important outcome of the above studies are critically analysed to find the relevance of the studies done during the course of this thesis work.

Chapter 1

Sol-Gel Technique for Synthesis of Advanced Materials

During the past two decades there has been considerable advances in the processing of electronic materials. Ceramic materials used in the modern electronic industry as thin films and bulk have a controlled crystal chemistry to achive desired physical and electronic properties. However, the electronic properties of the ceramic thin films strongly depends on the the purity and the microstructure of these films. Therefore, technologies that preserves purity of materials and provides room for manipulation of microstructure have a clear edge over the others in modern material science. In this regard sol-gel processing is considered to be very promising.

Sol-gel process is identified as one of the major material processing technology in recent years due to its versatility in synthesizing new materials for a variety of applications. Fabrication of ceramic oxide thin films by sol-gel process has become an important activity in the area of thin film technology due to its ease of fabrication, better reproducibility, cost effectiveness and high purity of end products. The structutal and physical properties of the thin films made by sol-gel process strongly depends on the selection of starting materials, the rate of hydrolysis and condensation, the chemical modification of the sol-gel system and other processing parameters. In fact these parameters can be precisely controlled to tailor the properties of the sol gel derived materials.

1.1 Historic Background of Sol-Gel Process

The principle of sol-gel process involves the hydrolysis and condensation of an alkoxide followed by polymerization to form metal oxide at elevated temperature. The first ever alkoxide was prepared from $SiCl_4$ and alcohol by Ebleman [1], who found that the compound gelled on exposure to atmosphere. However these materials remained of interest only to chemist for a century. It was finally recognized by Geffken [2] in 1930's that alkoxides could be used in the preparation of oxide thin films. The process was developed by Schott glass company in Germany and was well understood, as explained in an excellent review by Schroder [3].

Ceramic industry began to show interest in sol-gel process in late sixties. Controlled hydrolysis and condensation of alkoxides for preparation of multicomponent glasses were independently developed by Levene and Thomas [4] and Dislich [5]. Thin films and coatings represent the earliest commercial applications of sol-gel technology. Thin films generally prepared by dipping or spinning consumes small amount of material and prepared without cracking in a short time make it advantageous for lot of applications. Sol-gel technique were first used to make optical coating as reviewed by Schroder [3]. Since then many new uses and applications of the sol-gel films has appeared in the area of microelectronics, applied optics and sensors. The current application of sol-gel thin films and coatings have been studied in detail by various groups worldwide [6-12].

1.2 Sol-gel Process in the Fabrication of Ferroelectric Thin Films - A Survey

One of the major activity in the sol-gel processing of thin films is the fabrication of ferroelectric thin films. Sol-gel process is a low temperature process which provides very good reproducibility of stoichiometry, thickness and composition for the thin films. However, more research is needed to evaluate the factors which affects the evolution of microstructure during hydrolysis and condensation, which in turn controls the stoichiometry and crystallinity of the films. Another advantage of the

sol-gel processing is that it can provide materials of composition that are difficult to obtain by other methods. Chemical modification and doping are some time necessary to achieve special properties for special applications [13]. Sol-gel proces has been used for the fabrication of various types of ferroelectric thin film, which includes titanates, zirconates and niobiates such as $BaTiO_3$, $SrTiO_3$, $PbTiO_3$, $Pb(Zr,Ti)O_3$, $(Sr,Ba)Nb_2O_6$, $LiNbO_3$, $KNbO_3$ in the past years. These materials are very important for application in a variety of new devices and instruments [14].

The first report was on the fabrication of ferroelectric $PbTiO_3$ by Budd etal [14,15] in 1985-86. They have used a mixture of titanium methoxyethoxide and dehydrated lead acetate dissolved in 2-methoxy ethanol. This was then modified by Aegerter et al.[16] by using acetyl acetone modified titanium isopropoxide and lead acetate dissolved in acetic acid. In these earlier films the dielectric constant obtained was of the order of 25 to 30. It was found that the film refractive index depends on the thermal processing conditions. Amorphous $PbTiO_3$ thin films of refractive index 2.35 were fabricated at 300^oC by Pyne etal. [17] in 1990. The refractive index of these films increased to 2.65 after annealing at 450^oC . The large value of refractive index of $PbTiO_3$ was utilised by Aegerter [16] in fabricating planer optical wave guides. Schwartz et al. [18] has fabricated $PbTiO_3$ thin films on GaAs substrate and studied their electrical properties. They found that a fast heat treatment was necessary, while annealing, to avoid the diffusion of As in to the $PbTiO_3$ layer, which degrades their electrical properties.

Another ferroelectic material, $LiNbO_3$ is found to be very useful in optical modulators, electrooptic switches and transducers due the large value of its electrooptic coefficient [19]. However, some of their outstanding properties such as Curie point and refractive index etc. are found to be very sensitive to their composition and growth conditions and it is very expensive to grow the single crystals of $LiNbO_3$. This has lead the researchers to look in to the feasibility of fabrication of thin films of $LiNbO_3$ by sol-gel process, which is very inexpensive and give good control over composition and stoichiometry. $LiNbO_3$ sol has been made by Hirano et al. [20] using alkoxides of Li and Nb based on ethanol and methoxyethanol. These films were crystallized at temperature as low as 400^oC . Polycrystalline $LiNbO_3$ films were

found to grow on Si (100) and Si (110) due to the presence of native SiO_2 layer on silicon [21]. Heteroepitaxial growth with preferred orientation was achieved by adding a small amount of water for hydrolysis. The grain size of the $LiNbO_3$ films were found to depend on the heating rate [22]. A refractive index value of about 2.15 was obtined for these film, which was less than the single crystal value presumably due to residual porosity in the film [23]. The dilelctric constant of $LiNbO_3$ film made by sol-gel process was about 23 at audio frequancies and a loss factor of 0.005 was measured at 1 MHz [24]

One of the most important ferroelectric thin film which has been deeply investigated is PZT (lead zirconate titanate). PZT subtituted with lanthanum (PLZT) is also very important from the application point of view. The first sol-gel PZT composition $PbZr_{0}.5Ti_{0}.5)_3$ was made by Fukushima etal. in 1984 [25] using lead 2-ethylhexanoate, zirconium acetyl acetonate and titanium tetrabutoxide. Pyne etal. in 1986 [26] made PZT thin films using lead acetate and alkoxides of zirconium and titanium in 2-methoxyethanol. They made crystalline PZT thin films after annealing at 500^oC . Quek etal. [27] reported for their PZT thin films a coercive field 4×10^6 V/m and a remanent polarization of 0.36 C/m^2. Similar results were also reported by Chen et al [28].

Sol-gel PZT thin films are extensively investigated for the fabrication of thin films capacitors for integration with GaAs junction field effect transitors to develop non-volatile, programmeble random access memories [29,30]. It is found that processing conditions are very important for getting good quality PZT films by sol-gel process. 5% excess of lead and faster heating rate during annealing are necessary to get perovskite PZT thin films [31]. A slow heating rate was found to increase the content of undesired, non ferroelectric pyrochlore phase in PZT material.

PLZT thin films are very useful in electro optic applications. Depending on the composition and processing conditions the crystal strucrure of PLZT will be either rhombohedral or tetragonal [32] and the unit cells of the material will be similar to reversible dipoles. This reversible dipole behaviour makes them useful in making non-volatile I-C memories. A field applied across the film can pole the material and align the randomly oriented dipoles in one of the two possible directions, which will

correspond to the binary 0 or 1 of a digital memory [19]. Only very few reprts are available on the fabrication of PLZT by sol-gel process [33,34].

Another class of ferroelectric materials with enormously large value of dielectric constant which are gaining more interest in capacitor technology are relaxor ferro electrics. They have a complex perovskite structure $(A_1,A_2)B_1,B_2)O_3$, where different cations occupy A and B sites. The relaxor behaviour is generally associated with the dissorder in site occupation. Okawada and co-workers in 1989-90 [35,36] developed lead magnesium niobiate (PMN) and lead iron niobiate (PFN) relaxor thin films, which crystallized in to perovskite phase above an annealing temperature of 600°C . The phase transformation was found to depend on annealing rate and the type of substrates. The dielectric constant measured was about 1800, which is much less than the bulk value of 16000. For preparing PMN they have used lead acetate and a double alkoxide of Mg and Nb. Other compositions like Lead zinc niobiate (PZN) and Lead magnesium niobiate titanate(PMNT) were also developed by sol-gel process.

$BaTiO_3$ is one of the widely used ferroelectric material in capacitor technology for developing high density thin film capacitors. Thin films of $BaTiO_3$ has not been investigated in detail for the understanding of their structural and microstructural evolution during sol-gel process. In fact sol-gel process has been used in the recent past for making ceramic powder of $BaTiO_3$ [16]. Recently sols for making $BaTiO_3$ thin films has been prepared by mixing a solution of titanium isopropoxide diluted with isopropanol [37-39] or Titanium ethoxide [40,41]with aquous solution of Barium acetate. Acetic acid or acetyl acetone was also added to avoid precipitation[42]. Films deposited were amorphous upto 500°C and have electrical breakdown strength 9×10^6 V/cm which is larger than that for crystalline films (10^5V/cm.) [43]. In these films ferroelectricity has been reported only after annealing above 800°C . A grain size of about 0.1μm was obtained in these films. The dielectric constant and loss factor measured were 50 to 90 and 2 to 3 respectively with a broad Curie point around 118°C [44,45]. Tuchiya et al. [42] obtained large dielectric constant for crackfree $BaTiO_3$ thin films deposited on platinum substrates and heat treated at 1000°C . The value of saturation polarization and coercive field obtained were about 2.3 $\mu C/cm^2$ and 2.8 kV/cm respectively. Recently Kamalasanan et al. has fabricated

$BaTiO_3$ thin films using barium 2-ethylhexanoate and titanium butoxide [46] and titanium isopropoxide [47]. These films were highly tansparent with good dielectric and ferroelectric properties. The dielectric constant and the loss factor measured for these films were about 600 and 0.01 respectively at 10 KHz.

$SrTiO_3$ thin films are found to be good candidate for fabricating memory capacitors due to their high dielectric constant values and high breakdown strength [48,49]. They can effectively replace conventional oxide materials like silicon dioxode and tantalum dioxide for the fabrication of MOS memory elements. There are few reports on the fabrication of $SrTiO_3$ thin films by sol-gel process. K. Y. Chen et al. have made $SrTiO_3$ thin films using hydroxide-alkoxide precursor system [51]. They found the films were severely cracked after annealing above 600^oC . The electrical properties of sol-gel derived $SrTiO_3$ thin films were studied in detail by Kamalasanan at al.[51]. The starting materials used in this study was strontium 2-ethylhexanoate and titanium isopropoxide.

The lower production cost for sol-gel processing of materials combined with the high degree of compositional homogeniety make the process superior over other thin film processing technologies.

1.3 Different Stages in Sol-gel Processing of Materials

A sol is a colloidal suspension of solid particle in liquid which can be used to make glasses and ceramics by the process of condensation and polymerization. The sol-gel processing of a material generally starts with the hydrolysis of an alkoxide. An alkoxide is a metalorganic compound which consists of a metal atom surrounded by a ligand. The general formula of an alkoxide is $M(OR)_n$, where M is the metal atom, R any alkyl group and n represents the valency of the metal atom.

The different mechanism taking place from the hydrolysis of metal alkoxides to form metal oxides are indicated in figure 1.1. The different stages of the sol-gel process are explained below in detail.

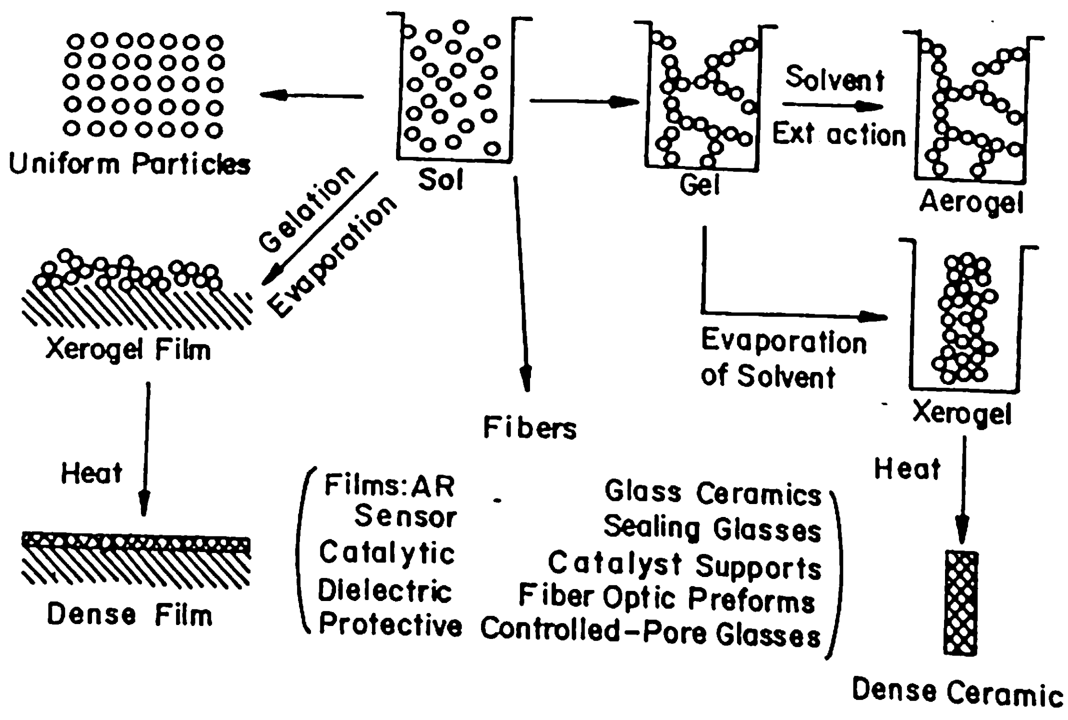

Figure 1.1: Different stages in the sol-gel processing of thin films, ceramics and glasses.

1.3.1 Hydrolysis

Metal alkoxides are popular precursors in the sol-gel processing of materials because they react readily with water. The reaction is called hydrolysis, because the hydroxyl group will be attached to the metal atom as shown below :

$$M(OR)_n + H_2O \longrightarrow HO - M(OR)_{n-1} + ROH \qquad (1.1)$$

The hydrolysis may go to completion under the presence of sufficient amount of water and catalyst:

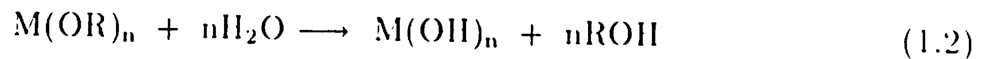

$$M(OR)_n + nH_2O \longrightarrow M(OH)_n + nROH \qquad (1.2)$$

Some times the reaction may end up in partially hydrolyzed products such as $M(OR)_{n-m}(OH)_m$.

1.3.2 Condensation and Polymerization

The two partially or fully hydrolyzed products can link together in a condensation reaction as

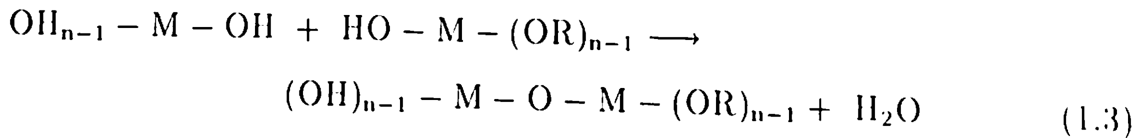

$$OH_{n-1} - M - OH + HO - M - (OR)_{n-1} \longrightarrow$$
$$(OH)_{n-1} - M - O - M - (OR)_{n-1} + H_2O \qquad (1.3)$$

or

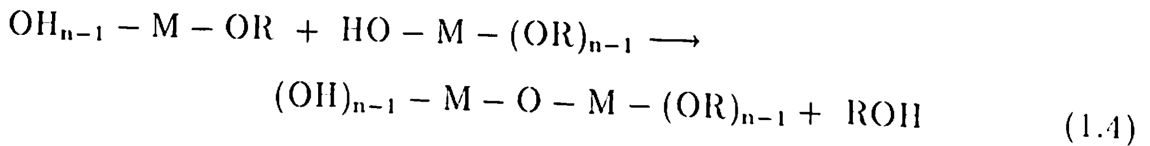

$$OH_{n-1} - M - OR + HO - M - (OR)_{n-1} \longrightarrow$$
$$(OH)_{n-1} - M - O - M - (OR)_{n-1} + ROH \qquad (1.4)$$

The condensation usually liberates H_2O or ROH as condensation product. This type of reaction can continue to build larger molecules by the process of polymerization. Hence condensation followed by polymerization is some times called as polycondensation. This polycondensation produces huge molecules by the linkage of thousands of small units called monomers, which are capable of forming at least two bonds. The number of bonds a monomer can form is called its functionality. Consider a metal atom with four ligands $MR_2(OH)_2$, of which two are unreacted R (alkyl) groups and two reactive (OH) groups. Such a compound can polymerize in chain or ring without

Dimer

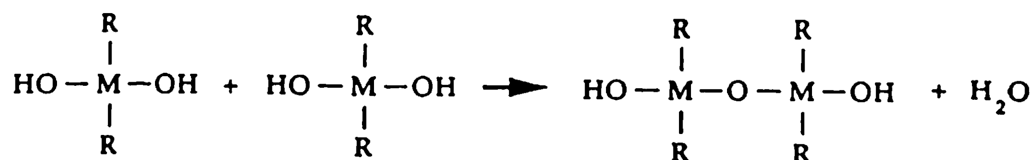

Chain

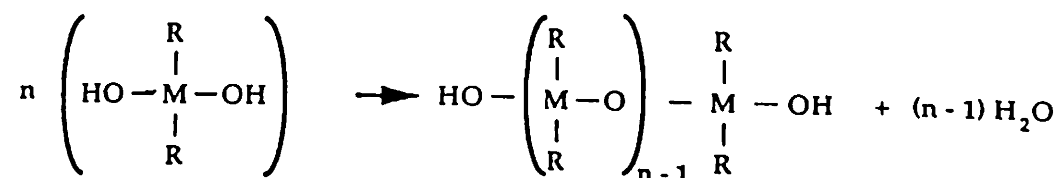

Ring

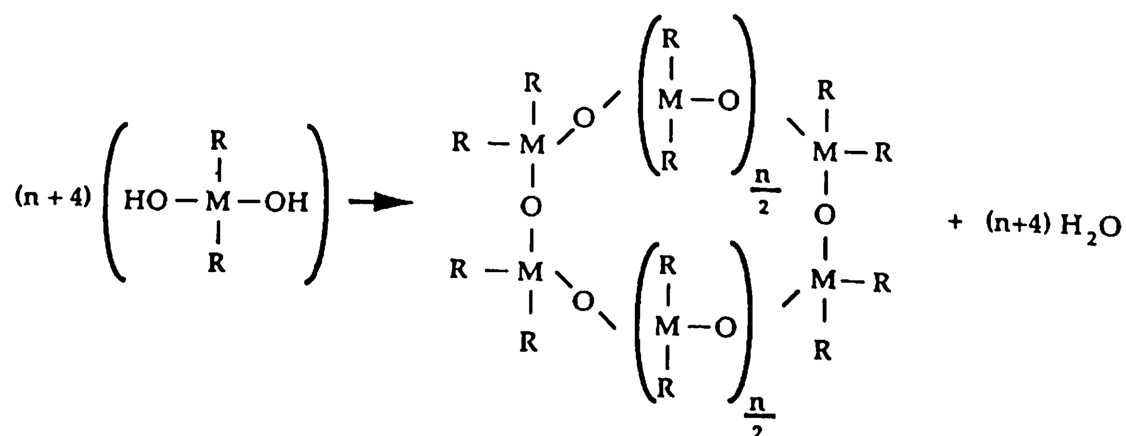

Figure 1.2: Formation of rings and chains by a bifunctional ligand to form oligomers.

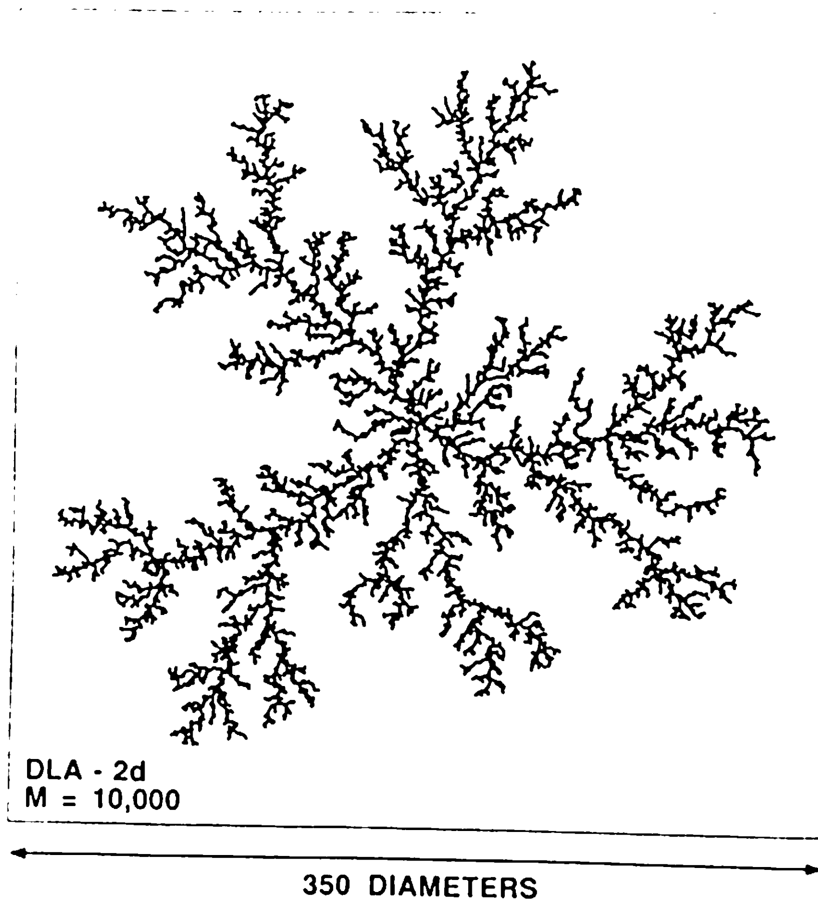

Figure 1.3: Formation of fractal polymers by the branching of polyfunctional monomers with $f > 2$ (computer simulation).

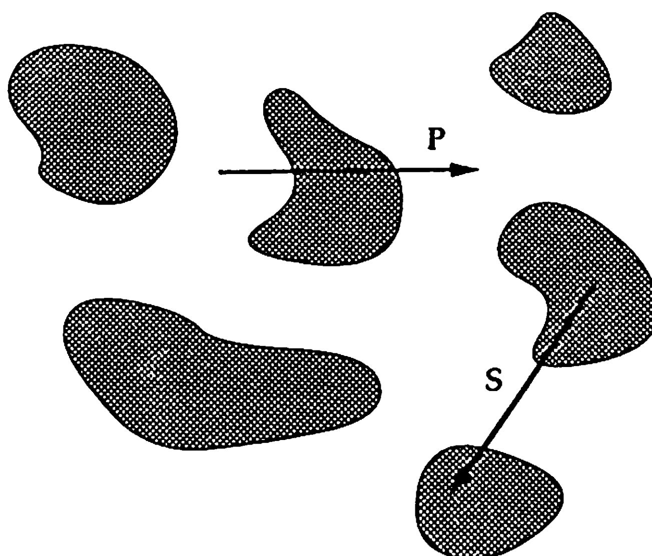

Figure 1.4: Schematic representation of a gel structure.

any branching.The formation of rings and chains by a bifunctional ligand is represented in figure 1.2 [52]. A polyfunctional unit (n > 2) can cross link to form three dimensional structure. Thus a fully hydrolysed molecule of polyfunctionality can form a complex branched fractal structure as shown in figure 1.3 [53]. The extent of branching controls the porosity of the sol-gel derived glass, monoliths and thin films.

1.3.3 Gelation

If a monomer can form more than two bonds there is no limit on the size of the molecule that can form. If one such molecule reaches macroscopic dimension so that it extent through the solution, then the substance is said to be a gel. The gel point is thus referred as the time at which the last bond is formed, that completes the giant molecule. Thus the gel is a substance that contains a continuous solid skeleton enclosing a continuous liquid phase. This way a gel is interpreted as some thing that have a continuous solid and liquid phases coexisting in colloidal dimension (1 μm), so that a line segment originating in a pore and running perpendicularly through the nearest solid surface must re-emerge in another pore in less than 1 μm distance and vice versa. The schematic representation of a gel structure is shown in figure 1.4.

It is found that the process of gelation starts with the fractal aggregates that grow in size until they begin to impinge one another. Then these clusters link together as described by the theory of percolation applied to gelation [54,55] i.e., near the gel point, bonds form at random between nearly stationary clusters, linking them together to form a network. The gel point corresponds to the percolation threshold, when a single cluster appears that extends through out the sol.

Gelation can occur, after the sol is cast in to a mould, which will transform to a gel of the shape of the mould or after casting a thin film on a substrate. Gelation can also occur by the rapid evaporation of solvent, as in the case of film formation.

1.3.4 Aging

Bond formation do not stop at gel point. The segment of gel network can still move close enough to allow further condensation. Moreover, there is still sol with in the gel

network and these smaller polymers themselves get attached to the main network. This process in which the structure and properties of the gel changes is called aging. Aging involves further phase transformation and condensation within solid and liquid phases. Some gels exhibit spontaneous shrinkage called syneresis, as bond formation induces contraction of the network and expulsion of liquid from the pores. Shrinkage of the gel involves deformation of network and transport of liquid through pores, which induces stress in the gel.

1.3.5 Drying

Drying by evaporation of the gel under normal condition gives rise to capillary pressure that causes shrinkage of the network. The resulting dried gel is called a xerogel which usually reduces in volume by a factor of 5 to 10 of the original volume. Under super critical conditions, the solvent can be extracted without the shrinkage of the gel network. This geves rise to what is called an aerogel, in which the solid fraction is as low as 1% of the total volume and remaining part consist of pores.

Most of the gels are amorphous even after drying, but many crystallizes after heating. The dried gel of silica is generally amorphous, but the gel of titanium dioxide crystallizes after heat treatment. For making pore free ceramics, the dried gel has to be heated to high enough temperatures to cause sintering. Once a gel has been densified, unique microstructures and properties can be achieved which are of far better quality than ceramics made by conventional means. The most advantageous feature of sol- gel process is that by controlling the hydrolysis, condensation and aging processes, one can tailor the microstructure of the material and hence achieve different desired properties.

1.4 Solution Chemistry of Metal Alkoxide Precursors

Transition metal alkoxides $M(OR)_n$, especially that of the d^o transition metal (Ti,Zr) are widely used as molecular precursors for making glasses and ceramics. Metal alkoxides are in general very reactive due to highly electronegative OR groups that stabilize

the metal atom(M) in its highest oxidation state and render M very susceptible to nucleophilic attack [56,57]. The lower electronegativity of transition metals cause them to be more electrophilic and thus less stable towards hydrolysis, condensation and other nucleophilic reactions. Transition metals often exhibit several stable coordinations and when co- ordinatively unsaturated, they are able to expand their co-ordination through nucleophilic association mechanism. For e.g., transition metal alkoxides dissolved in non polar solvent often form oligomers via alkoxy bridging,

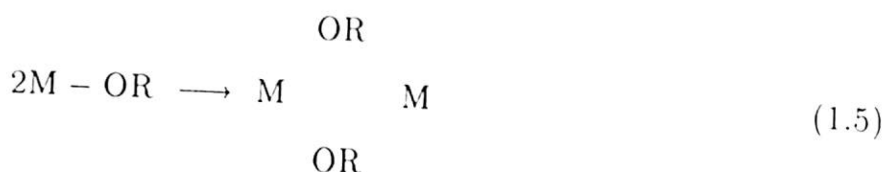

(1.5)

In polar solvents such as alcohol, either alkoxy bridging or alcohol association can occur. The greater reactivity of transition metal alkoxides (TMA) requires that they be processed with stricter control of moisture and conditions of hydrolysis in order to prepare homogeneous gel rather than precipitates. The rapid reaction kinetic of TMA reactions make it difficult to study their reaction mechanisms very difficult. In this regard Berghund and co-workers developed the rapid mixing apparatus to study chemical and structural changes occurring at very short time [58].

1.4.1 Mechanism of hydrolysis and Condensation

For co-ordinatively saturated metals in the absence of catalyst, hydrolysis and condensation both occurs by nucleophilic substitution (SN) mechanism involving nucleophilic addition (SA) followed by proton transfer from the attacking molecule to an alkoxide or hydroxo ligand within the transition state and removal of protonated species as either alcohol (alcoxolation) or water (oxolation) [56,59,60].

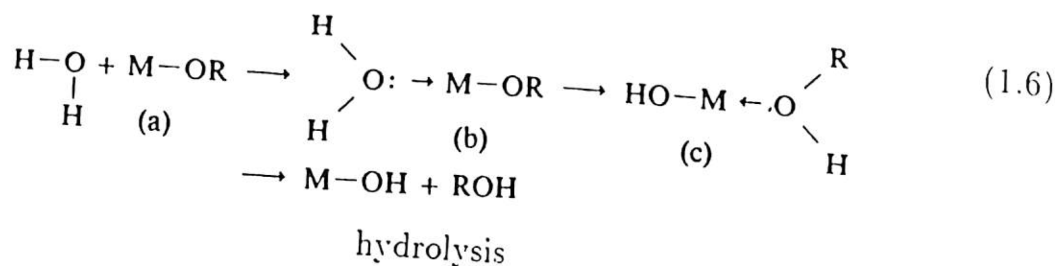

(1.6)

hydrolysis

(1.7)

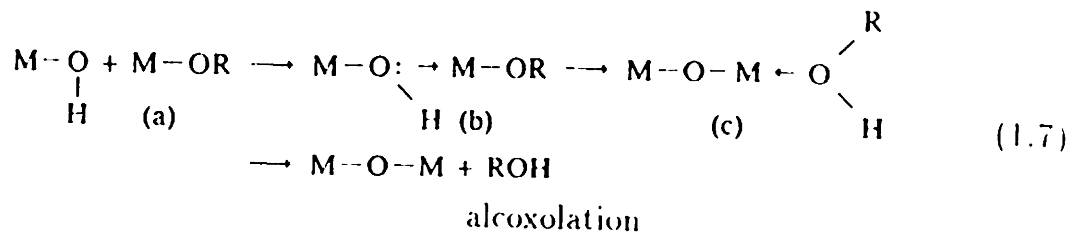

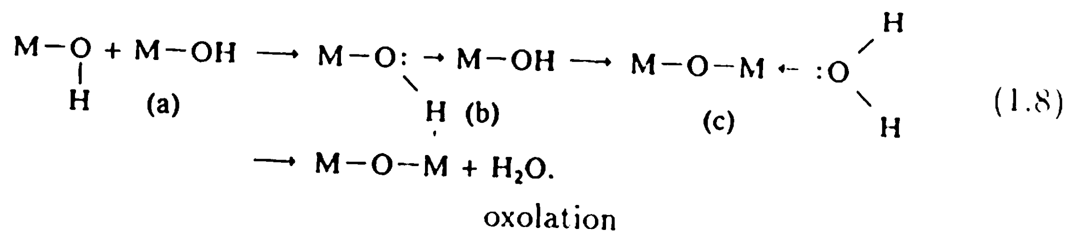

When $N-Z >$ 0, condensation occurs by olation,

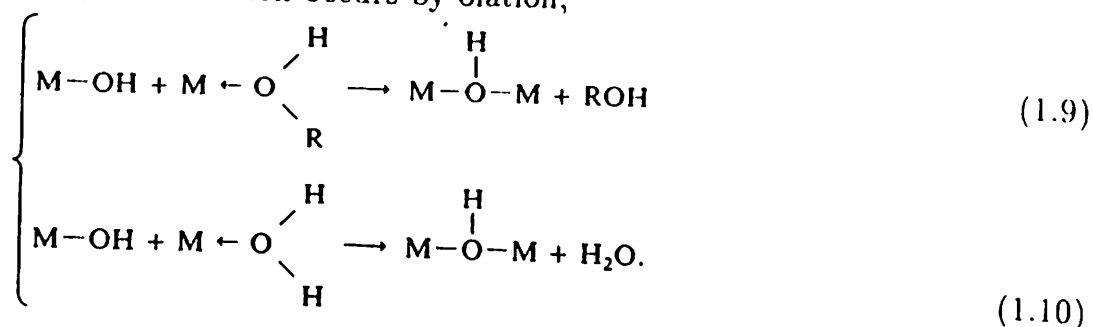

The thermodynamics of all these reactions are governed by the strength of the entering nucleophilic, electrophilicity of the metal atom and partial charge and stability of the leaving group. These reactions are favoured when $\delta(O) \ll 0$, $\delta(M) \gg 0$ and $\delta(H_2O)$ or $\delta(ROH) > 0$ [56]. Calculation of charge distribution within transition state of a titanate dimer pertaining to either oxolation or alkoxolation, $[Ti_2(OEt)_6(OH)_2]$ indicates that protonation of OEt produces a more positively charged leaving group ($\delta(EtOH) = +0.02$) than protonation of $OH(\delta(HOH)) = -0.25$ [56]. Thus oxolation should be the favoured condensation reaction between partially hydrolyzed coordinatively saturated titanate precursors.

Since the transition state involves an associative mechanism accompanied by a proton transfer, kinetics are governed by the extent of co-ordination saturation of the metal $N-z$ and the transfer ability of proton. Larger value of $N-z$ and greater acidities of the proton reduces the associated activation barriers and enhance the kinetics. Transition metals are very electropositive, which gives a partial positive charge to corresponding alkoxides and makes them very reactive. The $\delta(M)$ values for various transition metal alkoxides are given in the table 2.1.

Another factor which affects the reaction kinetics is the extent of oligomerization (molecular complexity) of metal alkoxide. The molecular complexity depends on

Table 1.1: Positive partial charge $\delta(M)$ for metals in various alkoxides.

Alkoxide	$\delta(M)$	Alkoxide	$\delta(M)$
$Zr(OEt)_4$	+0.65	$VO(OEt)_3$	+0.46
$Ti(OEt)_4$	+0.63	$W(OEt)_6$	+0.43
$Nb(OEt)_5$	+0.53	$Si(OEt)_4$	+0.32
$Ta(OEt)_5$	+0.49		

the nature of metal atom. Within a particular group it increases with atomic size of the metal (see table 2.1). Molecular complexity also depends on the alkoxide ligand, for e.g., $Ti(OEt)_4$ exhibits an oligomeric structure, where as $Ti(OPr)_4$ remains monomeric. Structure of several titanium alkoxide oligomers are shown in figure 1.5. It is observed that alkoxy bridges are more stable towards hydrolysis than associated solvent molecule and in some cases terminal OR ligands. Therefore, starting from a particular alkoxide, the kinetics and resulting structure can be controlled by choice of solvent [56]. Thus alkoxy-bridging allows controlled hydrolysis of alkoxide whereas alcohol association results in rapid hydrolysis and formation of highly condensed product.

1.4.2 Role of Catalyst

Acid or base catalyst can both influence the hydrolysis and condensation rates and structure of condensed product. Acid serves to protonate negatively charged alkoxy groups, enhancing reaction kinetics by producing good leaving groups,

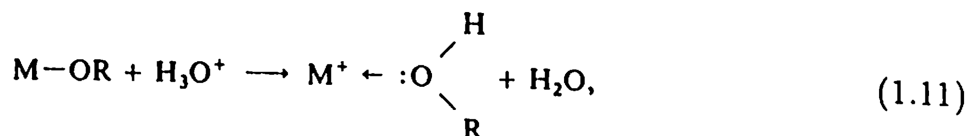

$$M{-}OR + H_3O^+ \longrightarrow M^+ \leftarrow :O\begin{smallmatrix} H \\ R \end{smallmatrix} + H_2O, \qquad (1.11)$$

and eliminates the requirement of proton transfer within the transition state. Hydrolysis goes to completion when sufficient water is added. Acid catalyzed condensation results in more extended less branched polymers.

Alkaline conditions produce strong nucleophilic by the deprotonation of hydroxo ligand. Condensation kinetics are systematically enhanced under basic conditions. The

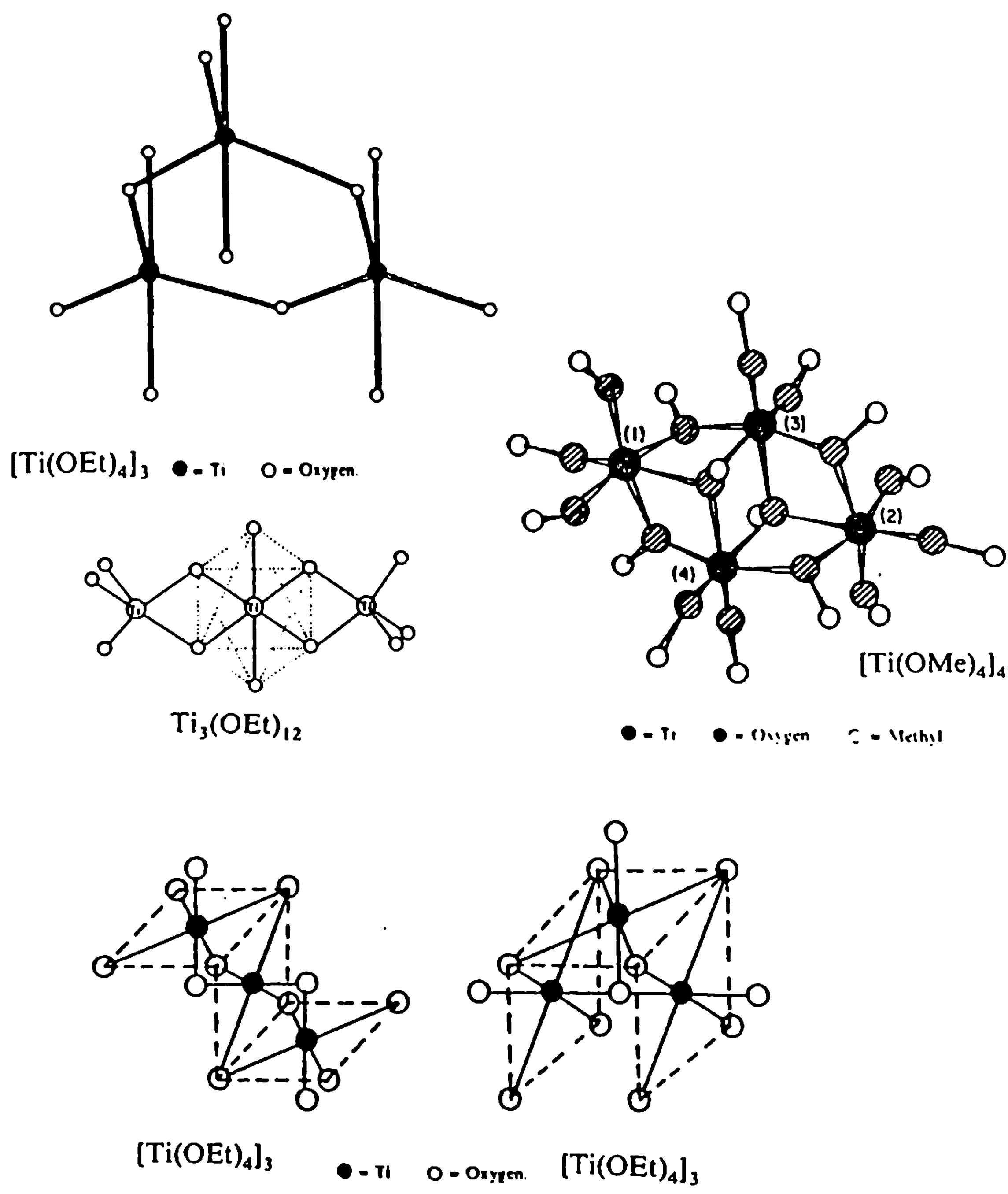

Figure 1.5: Structure of different titanium alkoxide oligomers.

base catalyzed hydrolysis and condensation leads to more compact highly branched systems.

1.4.3 Chemical Modification

Chemical modification of transition metal alkoxides with alcohols, acids, bases or chelating agents are commonly employed to retard the hydrolysis and condensation reaction rates in order to control the condensation pathway of evolving polymers [56,59].

In most cases the modification occurs by an SN reaction between a nucleophilic reagent (XOH) and metal alkoxide to produce a new molecular precursor [60].

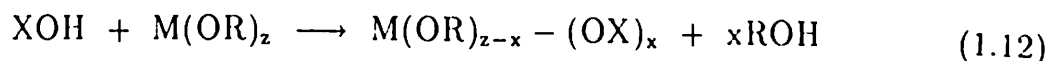

$$XOH + M(OR)_z \longrightarrow M(OR)_{z-x} - (OX)_x + xROH \quad (1.12)$$

The hydrolysis and condensation of modified precursor depends on the stability of the modifying ligands. Generally less electronegative ligands are removed during hydrolysis, where as more electronegative ligands will be removed slowly during condensation [56]. In substituted precursors, stable modifying ligands cause the effective functionality towards condensation to be reduced, resulting in less condensed products and promoting gelation.

Alcohol exchange reaction readily occurs with metal alkoxide precursors as

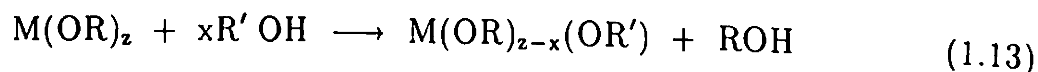

$$M(OR)_z + xR'OH \longrightarrow M(OR)_{z-x}(OR') + ROH \quad (1.13)$$

This makes alcohol exchange to be a common method of alkoxide synthesis [61]. Ti(OPr)4 is monomeric and the Ti atom exhibits a coordination number, N=4. The addition of glacial acetic acid causes an exothermic reaction and X-ray absorption near edge spectroscopy (XANES) experiments indicate that N increases to 6 [62]. During hydrolysis, ^{1}H and ^{1}3C NMR and IR spectroscopy indicate that OPr groups are preferentially hydrolyzed [63], where as the bridging acetate ligands remain bonded to titanium during condensation process. Since they are not hydrolysed, the bridging acetate ligands effectively alter the condensation pathway, there by promoting the formation of linear polymers composed of edge shared octahedra.

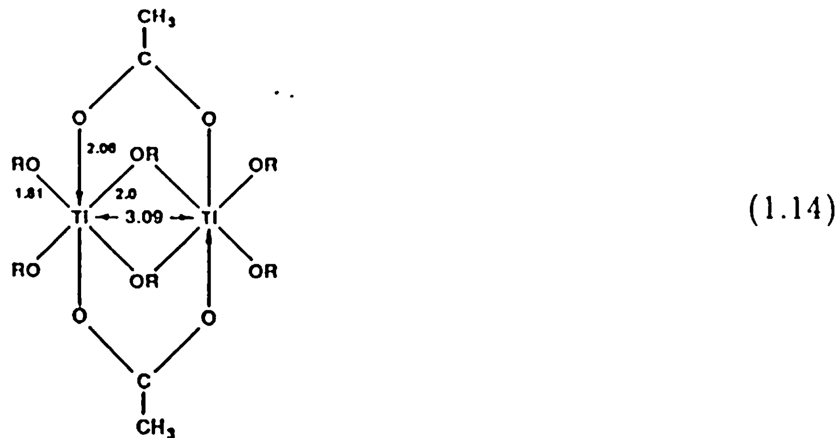

(1.14)

An equimolar mixture of acetyl acetone (acac) and Ti(OPr)4 results in an exothermic reaction and a clear yellow solution is obtained, showing a complexation by the bonding of acac to titanium. Addition of acac increases the coordination number of titanium from 4 to 5. There is no Ti-Ti correlation. A 1:1 molar ratio of Ti(OPr)4 and acac results in the following complex.

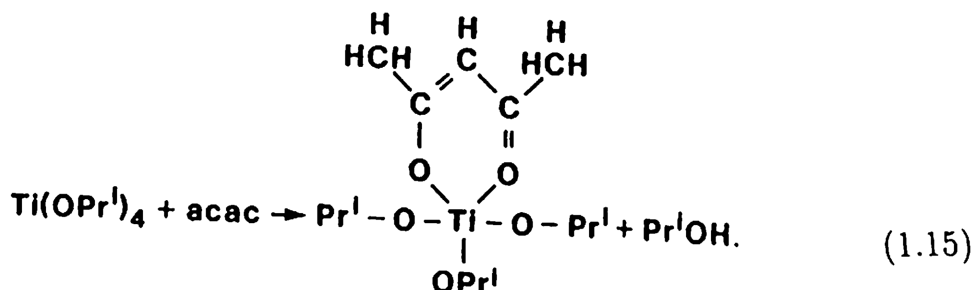

(1.15)

A 2:1 molar ratio of Ti(OPr) and acac results in an octahedrally coordinated dichelated precursor.

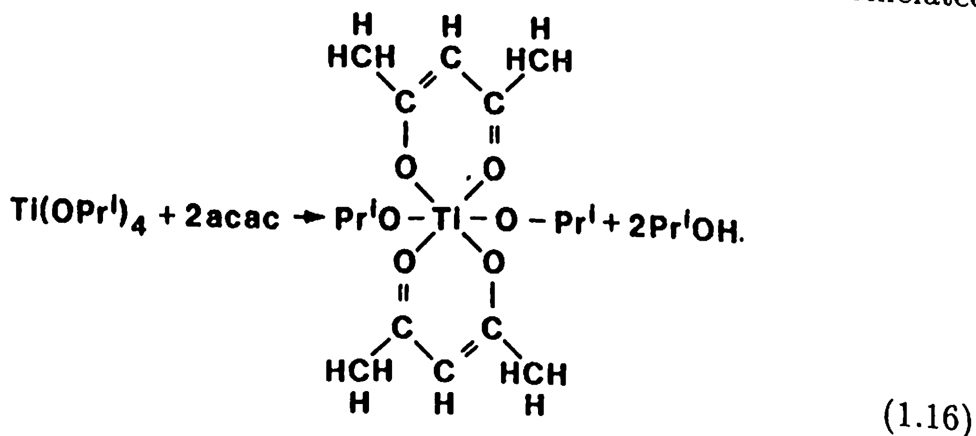

(1.16)

The addition of water to $Ti(OPr)_3acac$ precursor causes OPr ligands to be preferentially hydrolyzed [64].

1.5 Sol-Gel Processing Applied to Thin Film Technology

One of the most technologically important aspect of sol-gel processing is that prior to galation, the sol is ideal for preparing thin films by spinning or dipping. Compared to other conventional methods such as evaporation, sputtering or CVD, the sol-gel process for thin film fabrication requires very less equipment and it is very cost effective. The most important advantage of sol-gel technology in thin film fabrication is invariably its ability to control precisely the microstructure of the deposited film i.e., pore volume, pore size, surface area, and grain size.

The structure of inorganic precursor influences the structure of the deposited film. The structure of the inorganic precursor can affect the relative rate of hydrolysis and condensation and the structure of gel. The film microstructure depends upon the size and extend of branching of the solution species prior to the film deposition. Control on these parameters helps to tailor the film porosity. During deposition (spinning or dipping) the sol undergoes vigorous evaporation and condensation. The solution concentration increases to 20 to 30 times the initial concentration and the viscosity increases drastically. The gelation in this case is said to be occurred when the condensing network is sufficiently stiff to withstand the flow due to gravity or fly off due to centrifugal force while dipping or spinning. Further, evaporation may collapse the film or generate porosity with in the film.

Although the physical and chemical factors that govern the polymerization and gelation are essentially same for films as that of bulk gels, several factors distinguish structural evolution in gel [65]. (1) The overlap of deposition and evaporation stages established a competition between evaporation and condensation. Evaporation tries

to compact the structure and condensation tries to stiffen the structure, thereby creating resistance to compaction. In bulk system gelation and drying stages are normally separated. (2) In the case of thin films, aggregation, gelation and drying occurs in seconds to minutes during dipping or spinning. The short duration of deposition and drying stages causes the film to experience considerably less aging (cross- linking) than bulk gels. This results in more compact dried structure.

1.6 Effect of Branching and Condensation Rate on Film Structure

During deposition and drying different polymeric species or particles rapidly concentrate on the surface of the substrate. The effective packing of these species on the surface of the substrate and hence the volume fraction of the solid phase depends on the extend of branching or aggregation of the solution species and the condensation rate.

In weakly branched system (lower condensation), due to limited condensation during film formation, it allows the precursor to inter-penetrate in response to the decreasing solvent concentration promoting dense packing and low pore volume. In highly branched system, i.e. aged sols, the deposited films normally have higher porosity. Aging leads to more cross linking in the network leading to a stiff structure, which inhibits the collapse of the polymer network and there by resulting in porous structure.

The porosity of the sol-gel films again depends on the relative rates of condensation and evaporation. Slower rate of condensation, coupled with faster evaporation leads to compact structures. The condensation rate can be controlled by adjusting the pH of the sol, while the evaporation rate can be controlled by adjusting the partial pressure of the solvent in the coating ambient.

The control of both precursor structure and deposition conditions results in precise tailoring of the film microstructure and properties such as porosity, pore size, surface area, grain size and refractive index. These tailored properties have been exploited in numerous applications of sol-gel derived thin films, ceramics and glasses.

1.7 Application of Sol-gel Processed Thin films

Various applications of sol-gel process derive from the various products obtained directly from gel state (monoliths, films, fibers, monosized powders for ceramic processing) combined with compositional and microstructural control and low processing temperatures. The reproducibility and purity makes sol-gel process, most important in materials processing. Low processing temperature which results from microstructural control expands the glass forming region by avoiding crystallization or phase separation, making new materials available to technologist in exploring new frontiers in material science.

Thin films and coatings represents the earliest commercial application of sol-gel technology [65]. The early applications of sol-gel films were in optical coatings as reviewed by Schroeder [54]. Since then many applications have appeared in electronic, protective, membrane and sensor applications.

Optical coatings alter the reflectance, transmission, or absorption of the substrate. TiO_2/Pd coated architectural glass is the best example of the current state of art [66]. TiO_2 controls the reflectivity and Pd content controls the absorption. In this manner buildings appear outwardly uniformly reflective, while light transmission is controlled in accordance with sun exposure to minimize summer cooling costs. Another most important optical oxide coating is the SiO_2-TiO_2 binary system of alternate layers of SiO_2 and TiO_2, whose refractive index can very from 2.2 to 1.4. By controlling the porosity of the film one can reduce the refractive index of SiO_2 thin films down to 1.2 [67]. The absorption of these films can be modified by incorporating transition metals to produce coloured coatings on various substrates [68,69]. In addition to reflective coatings, oxide coatings on glass and silicon substrates have been used extensively as anti reflective coatings (AR) in solar cell fabrications to improve efficiency. They are also been used as laser damage resistant coatings for laser optics [70].

Different electronic thin films fabricated using sol-gel technology includes high temperature super conductors [71,72], tin oxide and vanadium pentoxide [73,74] as transparent conducting thin films, ferroelectric thin films of barium and lead ti-

TH-4876

tanates, PZT [75-78] etc. Sol-gel process gives precisely controlled stoichiometry combined with well crystallized crackfree microstructures and high purity.

Protective film coatings are another major field of application of sol-gel process [79-82]. Protective coatings impart corrosion and abrasion resistance, promote adhesion, increase strength or provide passivation or planarization.

References

1. J. J. Ebelmen, Ann. 57, 331(1846).
2. W. Geffcken and E. Berger, German Patent 736411(May 1939).
3. H. Schroeder, Phys. Thin Films 5, 87-141(1969).
4. L. Levene and I. M. Thomas, U.S. Patent 3,640,093(Feb. 8, 1972).
5. H. Dislich, Angewandt Chemie 10 [6], 363-370(1971).
6. H. Dislich, *Transformation of Organometallics into Common and Exotic Materials: Design and Activation*, NATO ASI series E. no. 141, ed. R.M.Laine (Martinus, Nijhoff, Dordrecht, 1988), p.236.
7. D. R. Uhlmann, and G. P. Rajendran, *Ultrastructural processing of advanced ceramics*, eds. J .D .Mackenski and D.R.Ulrich (Wiley, New York, 1988), p.223.
8. C. J. Brinker, *Transformation of Organometallics into Common and Exotic Materials: Design and Activation*, NATO ASI series, E. no. 141, ed. R.M.Laine (Martinus Nijhoff, Dordrecht, 1988), p.261.
9. H. Dislich, J. Non-Cryst. Solids 73, 599-612(1985).
10. D. L. Segal and J. L. Woodhead *Novel Ceramic Fabrication Process and Application*, ed., R. W. Davidge, Br. Ceramic, Proc., 38 (1986) 245.
11. H. Schmidt and B. Seiferling *Better Ceramics Through Chemistry*, II, eds. C. J. Brinker, D. E. Clark, and D. R. Ulrich (Mat.Res.Soc., Pittsburgh, Pa., 1986), p.739.
12. H. Dislich *Sol-Gel Technology of Thin Films: Fibers, Preforms, Electronics, and Speciality Shapes*, ed. L. C. Klein (Noyes, Park Ridge, N.J., 1988) p.50.
13. Laural M. Sheppard, Ceram. Bull. 71, 85 (1992).
14. K. D. Budd, S.K. Dey and D.A. Payne, Proc. Br. Ceram. Soc. 36, 107 (1985).

15. K. D. Budd, S. K. Dey and D. A. Payne, Mater. Res. Soc. Symp. Proc. 73, 711 (1986).

16. M. A. Aegerter, Y. Charbouillot, N. Mohallem, A. A. da Silva and L. H. De Godoy, *Ultrastructure Processing of Ceramics glasses and composites*, Tucson, AZ, (1989).

17. K. D. Budd and D. A. Pyne, Sol-gel Optics, Proc. SPIE, 450 (1990).

18. R. W. Schwartz, Z. Xu, D. A. Payne, T. A. de Temple and M. A. Bradley, Mater. Rec. Soc. Symp. Proc. 200, 167 (1990).

19. G. H. Haertling *Electro-optic Ceramics aand Devices in Electronic Ceramics*, ed. L. M. Levinson (Dekker, New York, 1988) p. 371.

20. S. Hirano and K. Kato, Adv. Ceram. Mater. 2, 148 (1987).

21. K. Nishimoto and M. J. Chima, Meter. Lett. 10, 348 (1991).

22. D. J. Eichorst and D. A. Payne, Sol-gel Optics, Proc. SPIE 1328, 456 (1990).

23. Y. Xu, C. J. Chen, R. Xu J. D. Mackenzie, Mater. Res. Soc. Symp. Proc. 200, 13 (1990).

24. D. S. Hagberg, D. A. Payne, Maater. Res. Soc. Proc. 200, 19 (1990).

25. J. Fukushima, K. Kodaira and and T. Matsuhita, J. Mater. Sci. 19, 595 (1984).

26. K. D. Budd, S. K. Dey and D. A. Payne, Mater. Res. Soc. Symp. Proc. 73, 711 (1986).

27. H. M. Quek, M. F. Yan, Ferroelectrics 74, 95 (1987).

28. R. A. Lipeles, N. A. Ives and M. S. Leung *Science of Chemical Proccssing*, ed. L. L. Hench and D. R. Ulrich,(Wiely-Interscience, New York, 1986) p.320.

29. S. K. Dey and R. Zuleeg, Ferroelectrics108, 1643 (1990).

30. L. E. Sannches, D. T. Dion, S. Y. Wu and I. K. Naik, Ferroelectrics 116,1 (1991).

31. C. Sudhama, C. J. Carrono, L. H. Parker, V. Chikarmane, J. C. Lee, A. F. Tasch, W. Miller, N. Abt and W. H. Shepherd, Mater. Res. Soc. Symp. Proc. 200, 331 (1990).

32. J. M. Herbert, Ceramic Dielectrics and Capacitors, Electrocomponent Science Monographs, Vol 6 (Gordon and Breach, New York, 1985).

33. V. K. Seth and W. A. Schulze, Ferroelectrics 112B,283 (1990).

34. S. L. Swartz, S. J. Bright, P. J. Melling and T. R. Shrout, Ferroelectrics 108, 1677 (1990).

35. K. Okawada, M. Imai and K. Kakunao Jpn. J. Appl. Phys. 28, 1271 (1989).

36. K. Okawada, S. Nakamura, M. Imai and K. KakunaoJpn. J. Appl. Phys. 29, 1153 (1990).

37. N. D. S. Mohallem and M. AA. Aegerter, Mater. Res. Soc. Symp. Proc. 121, 515 (1988).

38. P. P. Phule and S. H. Risbud, Mater. Res. Soc. Symp. Proc. 121, 275 (1988).

39. P. P. Phule and S. H. Risbud, Adv. Ceram. Mater. 3, 183 (1988).

40. A. Mosset, I. Gauthier-Luneau, J. Galy, P. Strehlow and H. Schmidt, J. Non-cryst. Solid 100, 339 (1998).

41. G. Tomandl, H. Rosch and A. Stiegelschmitt, Mater. Res. Soc. Symp. Proc. 121, 281 (1988).

42. T. Tuchiya, T. Kawano, T. Sei and J. Hatano, J. Carem. Soc. Jpn. 98, 743 (1990).

43. R.G. Dosch, Mater. Res. Symp. Proc. 32, 157 (1984).

44. M. I. Yanovskaya, N. Ya. Turova, E. P. Turevskaya, A. V. Novoselova, Y. N. Venevtsave, S. I. Sigitove and E. M. Soboleva, Inorg. Mater. 17, 221 (1981).

45. N. D. S. Mohallem, PhD. thesis, University of Sao Paulo (1990).

46. M. N. Kamalasanan, S. Chandra, P. C. Joshi and A. Mansingh, Appl. Phys. Lett. 59, 3547 (1991).

47. M. N. Kamalasanan, N. Deepak Kumar and S. Chandra, J. Appl. Phys. 74, 5679 (1993).

48. G. Mohan Rao and B. S. Krupanidhi, J. Appl. Phys. 75, 2604 (1994).

49. Josef Gerblinger and Hans Meixner, J. Appl. Phys. 67, 7453 (1990).

50. Kung-Yean Chen, Lang-Luen and Dah-Shyang Tsai, J. Mater. Sci. Lett. 10, 1000 (1991).

51. M. N. Kamalasanan, N. Deepak Kumar and S. Chandra, J. Appl. Phys. 74, 679 (1993).

52. C. J. Brinker, G. W. Scherer *Sol-gel Science: Physics and Chemistry of Sol-Gel Processing.* (Academic, New York, 1990)

53. P. Meakin, Ann. Rev. Phys. Chem. 39, 237(1988).

54. R. Zallen, *The Physics of amorphous solids* (Wiley, New York, 1983), Chapter 4.

55. D. Stauffer, A. Conigalio, and M. Adam, Advances in Polymer Science 44, 103(1982).

56. J. Livage, M. Henry and C. Sanchez, *Sol-gel Chemistry of Transition Metal Alkoxides* in progress in solid state chemistry, 18, 259 (1988).

57. L. G. Hubert, Pfalzgraf, New J. of Chem. 11, 663(1987).

58. R. W. Hartel and K. A. Burglund,*Better Ceramic Through Chemistry*, Mater. Res. Soc. Symp. Proc. 73, eds. C. J. Brinker, D. E. Clarll and D. R. Ulrich (Mater. Res. Soc., Pittsburgh, Pa.,633(1986).

59. L. Livage and M. Henry, *Ultrastructure Processing of Advanced Ceramics*, eds. J. D. Meckenzie and D. R. Ulrich (Wiley, New York, 1988), p. 183.

60. C.Sanchez, J.Livage, M.Henry and F.Babomean, J.Non- Cryst.Solids, 100, 65 (1988).

61. D. C. Breadley, R. C. Mehrotra, and D. P. Gany, *Metal Alkoxides* (Academic Press, London, 1978).

62. J. Livage and M. Henry *Ultrastructure Processing of Advanced Ceramics*, eds. J. D. Mackenzie and D. R. Ulrich (Wiley, New York, 1988) p.183.

63. J. Livage, C. Sanchez, M. Henry and D. S. Doeuff, Solid State Ionics 32/33, 633 (1989).

64. C. Sanchez, F. Babanneu, S. Doeuff and A. Leaustic *Ultrasturcture Processing of Advanced Ceramics* eds. J. D. Mackenzie and D. R. Ulrich (Wiley, New York, 1988).

65. C. J. Brinker, A. J. Hurd and K. J. Ward *Ultrastructure Processing of Advanced for Ceramics* eds. J. D. Mackenzie and D. R. Ulrich (Wiley, New York, 1988) p.223.

66. S.Dislich and E.Hussmann, Thin Solid Films 77 (1981), 129.

67. W. Gefficken and E. Berger, Deutsches Reichspatent 736411 (May 6, 1939), assigned to Jenaer Glaswrke Schott & Gen. Jenta.

68. A. Duran, J. M. Fernandez Navarro, P. Mazon and A. Joglar, J.Non- Cryst.Solids 82, (1986), 391.

69. F. Orgaz and H. Rawson, J.Non-Cryst.Solids 82 (1986) 378.

70. R. B. Pettit, C. S. Ashley, and C. J. Brinker *Sol-Gel Technology for Thin Films, Fibers, Preforms, Electronics and Specialty Shapes*, ed. L. C. Klein (Noyes, Park Ridge, N.J., 1988) pp. 80-109.

71. P. Srehlow, H. Schmidt and M. Birkhahn *Better Ceramics Through Chemistry III*, eds. C. J. Brinker, D. E. Clark, and D. R. Ulrich (Mat.Res.Soc., Pittsburgh, Pa. 1988), p.791.

72. M. Tatsumisago, H. Sago and T. Minami, Chem Express 3 (1988) 311-314.

73. J. Livage and J. Lemerle, Am.Rev.Mater. Sci. 12(1982) 103-122.

74. H. Dislich and P. Hinz, J.Non-Cryst. Solids 48 (1982) 11.

75. J. Fukushima, Yogyo Kyoaishi 83(1975), 204.

76. K. D. Budd, S. K. Dey and D. A. Payne *Better Ceramics Through Chemistry II*, eds. C. J. Brinker, D. E. Clark and D. R. Ulrich (Mat.Res.Soc., Pittsburgh, Pa, 1986), p.711.

77. R. A. Lipeles, D. J. Coleman, and M. S. Leung *Better Ceramics Through Chemistry II*, eds. C. J. Brinker, D. E. Clark and D. R. Ulrich (Mat.Res.Soc., Pittsburgh, Pa, 1986), p.665.

78. R. A. Lipeles and D. J. Coleman *Ultrstructure Processing of Advnced Ceramics*, eds. J. D. Mackenzie and D. R. Ulrich (Wiley, New York, 1988), p.919.

79. C. G. Pantano, R. K. Brow and L. A. Carman *Sol-Gel Technology for Thin Films, Fibers, Preforms, Electronics and Specially shapes* ed. L. C. Klein (Noyes, Park Edige, N.J., 1988), p.110.

80. M. Masashi, B. Yamagishi, M. Noshiro, Y. Jitsurgiri and K. Ohnishi, European Patent Appl. 85107552.3, June 19, 1985.

81. R. B. Pettit and C. J. Brinker, SPIE Optical Coatings for Energy Efficiency & Solar Applications, 324 (1982) 176.

82. S. T. Reed and C. S. Ashley *Better Ceramics Through Chemistry III*, eds.C. J. Brinker, D. E. Clark and D. R. Ulrich, (Mat. Res. Soc. Pittsburgh, Pa, 1988) p.631.

Chapter 2

Ferroelectric Materials and Their Applications - A Review

2.1 Ferroelectricity and related materials

Ferroelectric state of material is characterized by the existence of a spontaneous polarization, which can be reversed by the application of an external electric field. The ferroelectric materials possess a non linear relation between the polarization and applied electric field giving rise to a hysteretic behaviour[1]. In simple terms a ferroelectric material can be switched between two stable states of polarization with same magnitude but opposite direction.

A typical ferroelectric hysteresis loop between applied field and electric polarization is shown in the figure 2.1. $+P_r$ and $-P_r$ represent the remanent polarization and P_s the saturation polarization. E_c is the coercive field, the opposite electric field required to bring the polarization to zero. Ferroelectric materials are generally characterized by a transition temperature at which the material changes from a non centrosymmetric polar state of lower symmetry to higher order non polar symmetric state[2,3]. A permanent polarization in the low temperature phase of the ferroelectric represents a modification of lattice compared to the more symmetric high temperature form of the material. Cochran[4] and Anderson[5] in 1959 introduced the concept that the ferroelectricity result from the instability of one of the normal lattice vibrational modes. The characteristic frequency of the so called soft mode, referring to the unstable lattice vibration, decreases on decreasing the temperature to the transition

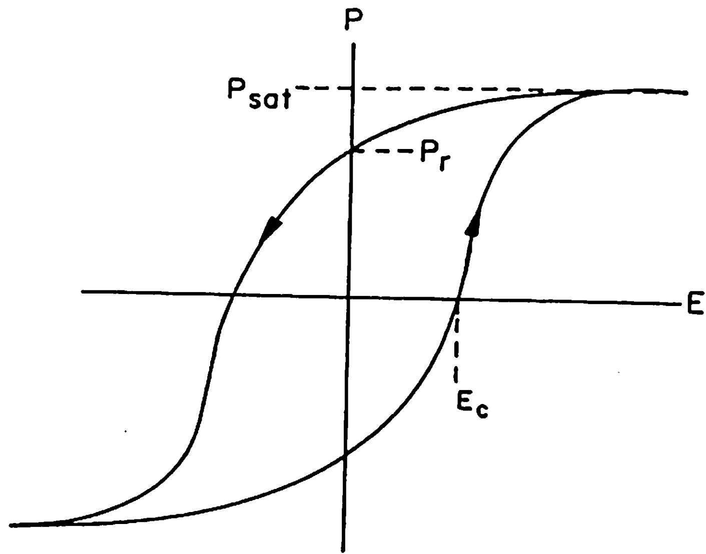

Figure 2.1: Typical ferroelectric hysteresis loop of Applied electric field versus polarization.

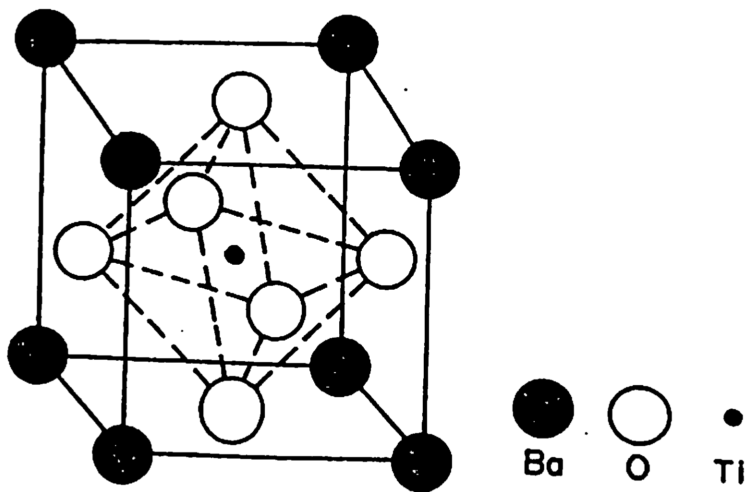

Figure 2.2: The perovskite crystal structure of $BaTiO_3$.

temperature, T_c, and restoring force tending to restore the displaced atoms to their normal position approaches zero. The soft mode then freezes and the atoms become permanently displaced, resulting in the ferroelectric state.

The origin of ferroelectricity lies in the interaction between the local polarization and macroscopic electric field E_L of the dielectric. The dipole moment induced in the material due to the local field can be written as

$$p = \alpha E_L \tag{2.1}$$

Considering all the polarizable entity are of same type and have a number density N, then the total polarization is given as

$$P = Np = N\alpha E_L \tag{2.2}$$

The local electric field experienced by the dipole by the application of an external field E will be represented as

$$E_L = E + \frac{P}{3\epsilon_o} \tag{2.3}$$

Where ϵ_o is the permitivity of free space. Solving Eq.2.2 and Eq.2.3 leads to the result

$$P = \frac{N\alpha}{[1-(1/3\epsilon_o)]N\alpha} E \tag{2.4}$$

The orientational polarization typically increases as $1/T$ as the temperature decreases leading eventually to an enormous value of polarization at a particular temperature, implying spontaneous polarization. Here the local field produced by the dipole has a sufficiently strong effect on the neighboring dipoles that all the dipoles prefer to orient in the same direction, even in the absence of an external field. This critical temperature is the Curie temperature or the transition temperature, T_c of the ferroelectric and the dielectric susceptibility takes the form

$$\chi = \epsilon_r - 1 = \frac{C}{T - T_c} \tag{2.5}$$

where C is a constant called Curie constant.

Ferroelectrics are unique among the family of materials as they possess individually and collectively, a large number of physical properties such as piezoelectric, pyroelectric and electro-optic effect. These properties are especially useful since they are

Table 2.1: Different types of ferroelectric crystals

Type	Material	T_c(K)	P_s in esu/cm^2
KDP	KH_2PO_4	123	16,000
TGS	Triglycine sulphate	322	8,400
Perovskite	$BaTiO_3$	393	78,000

highly sensitive to external stimuli, and hence, useful for device applications in bulk and thin film form.

Discovered by Valesek in 1920 in Rochelle salt, ferroelectricity underwent significant development with the discovery of new materials such as single crystal and ceramic barium titanate [6]. In 1954, the ferroelectric lead zirconate titanate ceramic compositions were developed [6] and a few years later complex compositions called relaxor ferroelectric with enormously high dielectric constant were found [7].

Table 2.1 shows some different types of ferroelectric materials and their transition temperatures and saturation polarization P_s .

2.2 Structural aspects of the ferroelectric phase transition

Ferroelectric phase transition can either be displacive or order-disorder type. If the ferroelectric phase is realized by minute displacement of atoms or molecules in the paraelectric phase, then such transition is said to be displacive. In order-disorder transition, the ferroelectric phase result because of the ordering of certain atoms or molecules in paraelectric phase. Most common ferroelectric materials like $BaTiO_3$, $SrTiO_3$, $PbTiO_3$ and PZT are of displacive type having a crystal structure identical with mineral perovskite ($CdTiO_3$) and is so referred to as a perovskite. Above Curie temperature their unit cell is cubic with the ions arranged as in figure 2.2. Below Curie temperature the structure is slightly distorted to tetragonal form with a dipole moment along the c-axis.

In the case of barium titanate [8] the Curie temperature is 120°C . Other transformations occur at temperatures close to 0°C and -80°C ; below 0°C the unit cell is

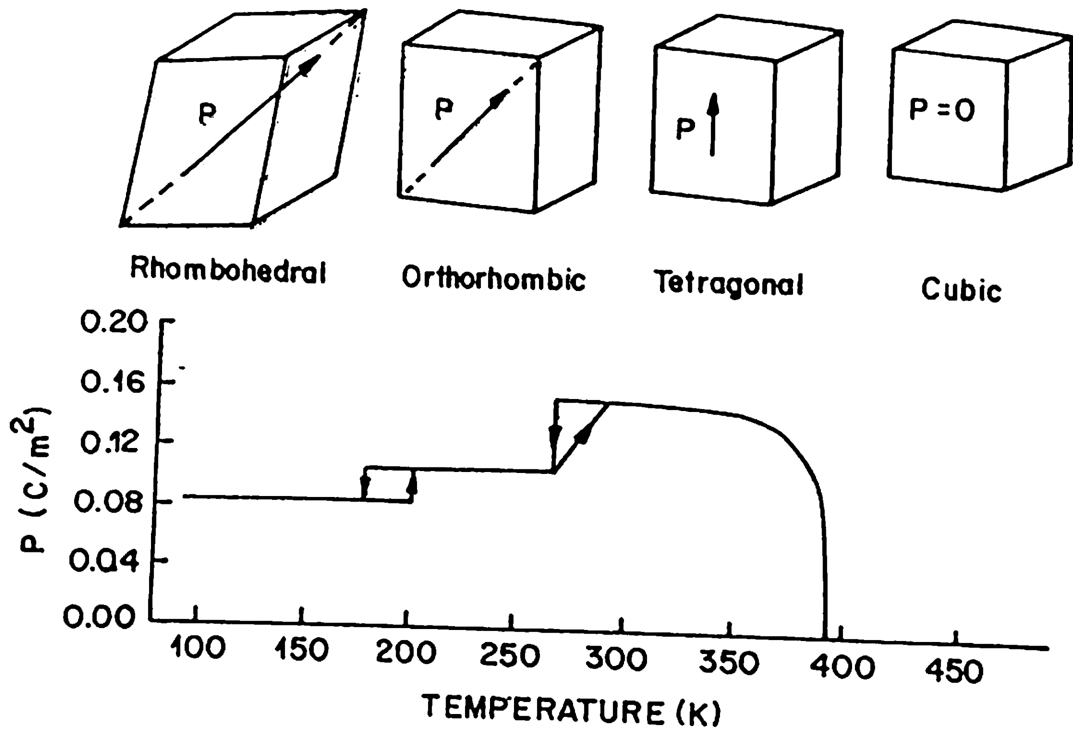

Figure 2.3: Projection of spontaneaous polarization $BaTiO_3$ onto one edge of the unit cell as a function of temperature.

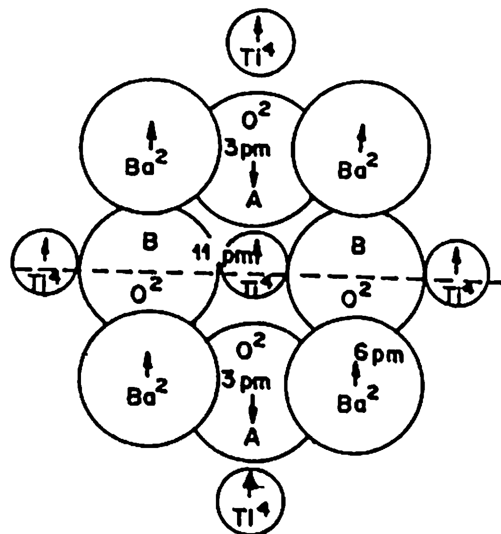

Figure 2.4: Approximate ionic displacements in the cubic tetragonal distortion in $BaTiO_3$.

orthorhombic with polar axis parallel to the face diagonal and below -80°C it is rhombohedral with polar axis along the body diagonal. The transformation are illustrated in figure 2.3.

The displacement of ions in the crystal structure of $BaTiO_3$ accompanying the cubic-tetragonal phase transition can give insight as to how the spontaneous polarization might be coupled from unit cell to unit cell. X-ray diffraction studies [9] have established that in the tetragonal form, taking the four central oxygen ions in the cubic phase as origin the other ions are shifted slightly as shown in figure 2.4. It is evident that, if the central Ti^{4+} ions is closer to one of the O^{2-} ion marked as A it will be energetically favourable for the Ti^{4+} ion on the opposite side of A to be located more distantly from that O^{2-} ions, thus inducing a similar displacement of all Ti^{4+} ions in a particular column in same direction. Coupling between neighboring columns occur in $BaTiO_3$ so that all O^{2-} ions are displaced in the same direction.

In tetragonal $BaTiO_3$ the energy of Ti^{4+} ions in terms of its position along c-axis can be represented by a double potential well as in figure 2.5. An applied field in opposite direction to the polarization may enable. Ti^{4+} ions to passover the energy barrier between two states and so reverse the direction of polarity at that point. This effects in the reduction of energy barrier for neighbouring ions and the entire region affected by the field will eventually switch to the new direction. An immediate consequence of spontaneous polarization in a body is the appearance of an apparent surface charge density and an accompanying depolarizing field E_D as shown in figure 2.6(a). The energy associated with the polarization in depolarizing field is minimized by twinning, a process in which the crystal is divided into may oppositely polarized region as shown in figure 2.6(b). These regions are called domains and the whole configuration shown comprises 180° domains. Thus the surface will develop in to a mosaic of areas carrying apparent charges of opposite sign, resulting in a reduction in E_D and in energy. This multidomain state can be transformed into a single domain by applying an electric field parallel to one of the polar direction. The domain with their dipole moment in the direction of the field grow at the expense of those aligned oppositely until only a single domain remains.

The presence of mechanical stress in the crystal results in the development of

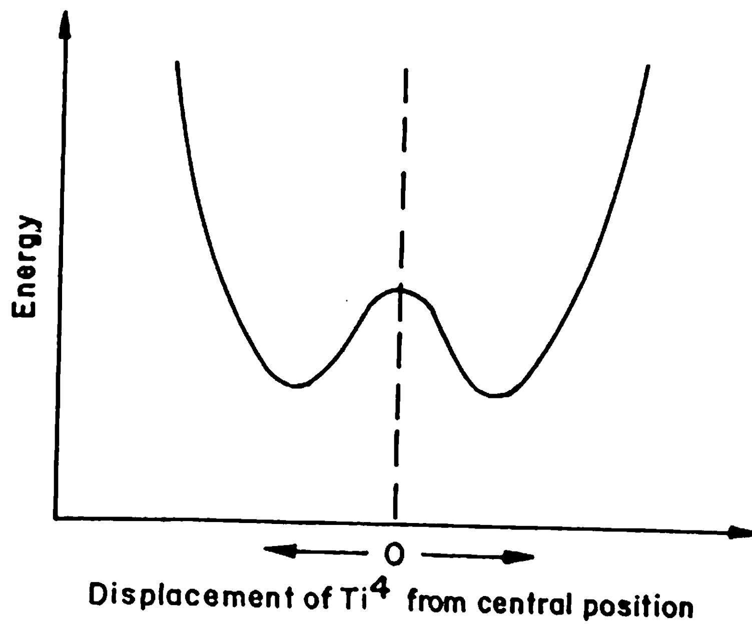

Figure 2.5: Variation of potential energy of Ti^{4+} ion along the c-axis.

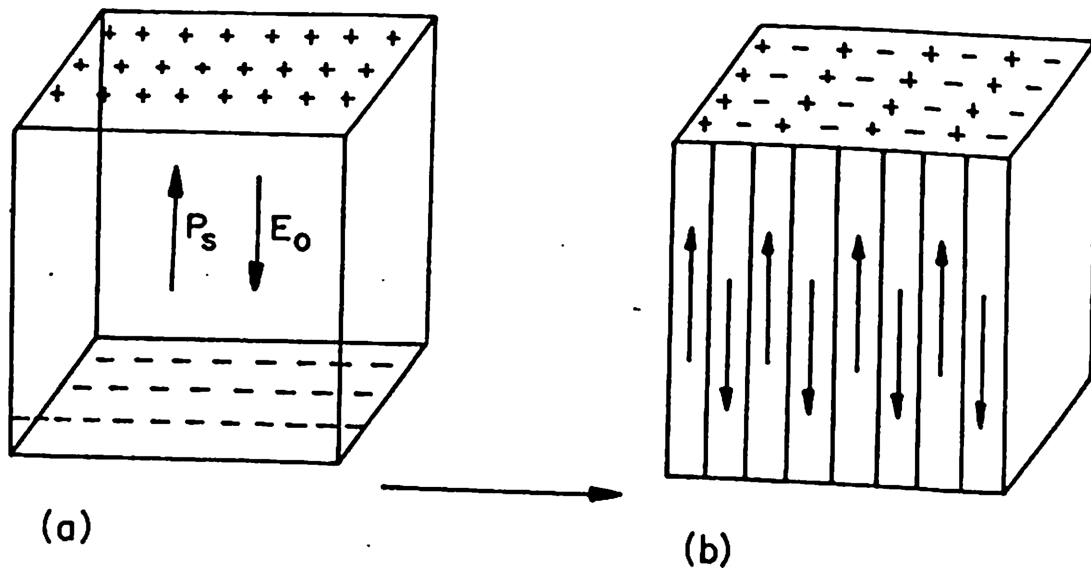

Figure 2.6: (a) Surface charge associated with spontaneous polarization (b) Formation of 180° domains to minimize electrostatic energy.

90° domains configured so as to minimize the strain. These type of domain usually present in ceramics where a transition from paraelectric to ferroelectric phase will lead to a large mechanical stress leading to the development of 90° domains. A polycrystalline ceramic that has not been subjected to an electric field behaves as a non polar material even through the crystal comprising it are polar. One of the valuable feature of the ferroelectric behaviour is that ferroelectric ceramics can be transformed in to polar material by applying a static field. This process is called poling.

The random direction of the crystallographic axes of the crystallites of a ceramic limit the extend to which the spontaneous polarization can be developed. It has been calculated that the fraction of spontaneous polarization of the single crystal polarization value that can be attainable in a ceramic are 0.83, 0.91 and 0.87 for perovskite with tetragonal, orthorhombic or rhombohedral structure respectively. In tetragonal $BaTiO_3$ ceramic the saturation polarization is about half the single crystal value. The value attainable is limited by the inhibition of 90° switching by internal strain although 180° switching can be almost complete.

2.3 Symmetry and ferroelectric phase transition

In general FE phase transition can be classified as continuous and discontinuous phase transitions. In case of continuous phase transition, the spontaneous polarization varies continuously with temperature and tends to zero at the transition temperature. A discontinuous phase transition is characterized by an abrupt change in the spontaneous polarization at the transition temperature. Normally the continuous phase transition are of the second order while the discontinuous ones are of the first order. In the case of a continuous phase transition the symmetry groups of FE phase is a sub group of one in the paraelectric phase. For discontinuous phase transition no such simple relations hold between the symmetry of the two phases.

A FE crystal can be considered as a slight modification of a certain non FE ideal crystal which is referred to as prototype. Accordingly, the prototype will be higher in the crystallographic symmetry than the FE crystal. Thus knowing the symmetry

of a prototype crystal and a given direction of spontaneous polarization, the possible symmetry group of the ferroelectric phase can be determined [9].

2.3.1 Landau theory of the phase transition in ferroelectrics

On thermodynamical consideration, the behaviour of a ferroelectric crystal can be obtained from the expansion of energy as a function of the polarization P. The Landau free energy in one dimension can be expressed as :

$$F(P,T) = \frac{1}{2}\alpha P^2 + \frac{1}{4}\beta P^4 + \frac{1}{6}\gamma P^6 + \ldots \quad (2.6)$$

The co-efficient α , β , γ are in general function of temperature. The expression do not contain the odd powers of P because the free energy of the crystal will not change by the polarization reversal (P to −P) This phenomenological formula can be applied for all the temperature range through paralectric and ferroelectric state.

Then the equilibrium polarization in an electric field E satisfies,

$$\frac{\partial F}{\partial P} = E = \alpha P + \beta P^3 + \gamma P^5 \quad (2.7)$$

To obtain the FE state, the co-efficient of the terms in P^2 must be negative, in which the polarization state is stable, while in a paraelectric state it must be +ve passing through zero at some temperature (Curie-Weiss temperature):

$$\alpha = \frac{(T - T_o)}{(\epsilon_o.C)} \quad (2.8)$$

where C is taken as a positive constant and T_o is equal to or lower than the actual transition temperature T_c (Curie temperature). The variation of α with temperature is explained microscopically by thermal expansion and other effects of anharmonic lattice interactions.

2.3.2 Second order phase transition

When β is positive, γ is often neglected because nothing special is added by this term. Using Eq.(7) polarization for zero field is obtained by considering either $P_s = 0$ or $P_s{}^2 = (T_o - T)/\beta\, \epsilon_o\, C$

$$\frac{T - T_o}{\epsilon_o\, C} + \beta\, P_s^3 = 0 \quad (2.9)$$

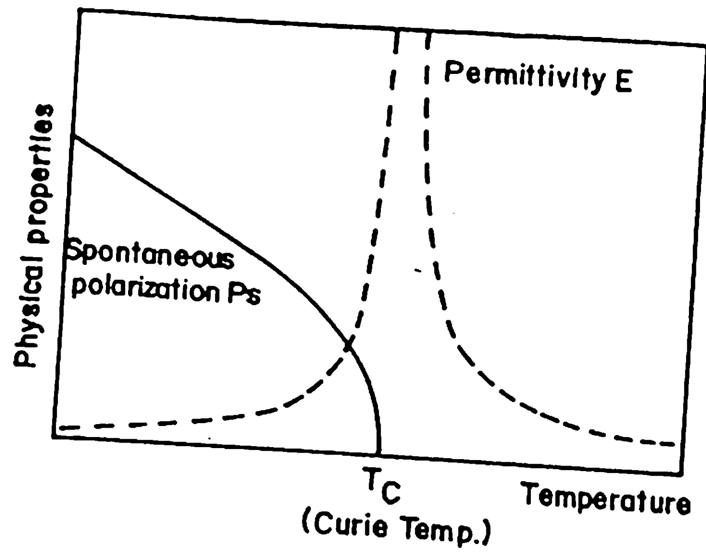

Figure 2.7: Variation of saturation polarizarion and relative permittivity as function of temperature for second order phase transition.

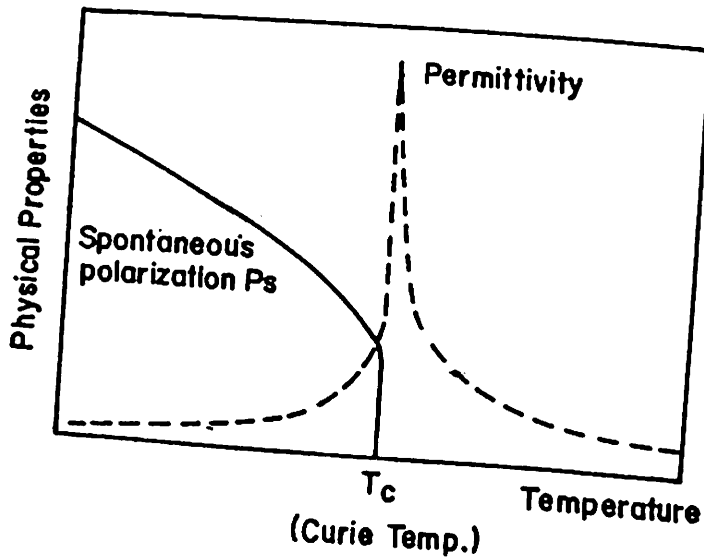

Figure 2.8: Variation of saturation polarizarion and relative permittivity as function of temperature for first order phase transition.

For $T \geq T_o$, the unique solution $P_s = 0$ is obtained. For $T < T_o$ the minimum of the Landau free energy is obtained as

$$P_s = \sqrt{(T_o - T)/(\beta \epsilon_o C)} \tag{2.10}$$

The phase transition occurs at $T_c = T_o$ and polarization goes continuously to zero at this temperature, this is called the second order phase transition.

Relative permittivity ϵ_r is calculated as:

$$\frac{1}{\epsilon_r} = \frac{\epsilon_o}{\partial P/\partial E} = \epsilon_o(\alpha + 3\beta P^2) \tag{2.11}$$

Then,

$$\epsilon_r = \begin{cases} C/(T - T_o) & (T > T_o) \\ C/[2(T_o - T)] & (T_o < T) \end{cases} \tag{2.12}$$

Figure 2.7 shows the variation of P_s and ϵ_r with temperature for second order phase transition. It is notable that the permittivity becomes infinite at the transition temperature. Trigylcine sulphate is an example of FE crystal possessing second order phase transition.

2.3.3 First order phase transition

When β is negative in equation 2.6. and γ is taken positive, the transition becomes first order. The equilibrium condition for E = 0 is obtained by considering either

$$P_s = 0 \quad \text{or} \quad \frac{(T - T_o)}{\epsilon_o C} P_s + \beta P_s^3 + \gamma P_s^5 = 0$$

Then,

$$P_s^2 = [-\beta + \sqrt{\beta^2 - \frac{4\gamma(T - T_o)}{\epsilon_o C}}]/(2\gamma) \tag{2.13}$$

The transition temperature T_c is obtained from the condition that the free energies of the paraelectric and FE phases are equal: i.e., F = 0, or:

$$\frac{(T - T_o)}{\epsilon_o \epsilon_r} + \frac{1}{2}\beta \mathbf{P}_s^2 + \frac{1}{3}\gamma \mathbf{P}_s^4 = 0 \tag{2.14}$$

Therefore,

$$T_C = T_o + \frac{3}{16}(\beta^2 \epsilon_o C/\gamma) \tag{2.15}$$

which indicates that the curie temperature T_c is higher than curie Wiess temperature by factor $(\frac{3}{16}(\beta^2\epsilon_o C/\gamma))$, and the discrete jump of the P_s appear at T_c . Also, the permittivity exhibits a finite maximum at T_c for a first order phase transition. The classical example for the first order phase transition in FE is $BaTiO_3$. Figure 2.8 represent the variation of P_s and ϵ_r with temperature for a first order phase transition.

2.4 Ferroelectric Thin Films for High Tech Applications

The present day quest towards miniaturization and integration of discrete electronic components had led to the development of thin film materials for a wide variety of applications. Among these, ferroelectric thin film are gaining more importance because of their versatile qualities for important application such as non-volatile radiation hard random access memories, high K capacitors, actuators, SAW (surface acoustic wave) devices, ac TFEL (thin film electroluminescent displays), and electro-optic devices [10-17].

Some of the most important ferroelectric thin film materials, their application and underlying phenomena useful in developing new devices are given in table (2.3). Many of the above mentioned devices based on FE thin film are under developing stage. These devices, which are of most recent interest and have been developed to a prototype state are summarized below.

2.4.1 Ferroelectric non-volatile memories

Ferroelectric materials in bulk were evaluated as non volatile memories in early times, but found less adequate due to (1) requirement of high operating voltage, (2) Fatigue and (3) a memory set problem. With the advent of integrated silicon technology and development of FE thin films, it has been overcome most of the problems which are there with bulk materials. This was accomplished by fabricating the FE memory element as a thin film at each memory site (2x2 μm) and superimposing it on top of the Si CMOS circuitry. With the development of planar MOS transistor technology for the switching transistors utilizing the FE material at each memory

Table 2.2: Some ferroelectric materials, their applications and basic phenomena utilized.

Materials	Phenomena	Applications
Perovskites (Titanates) $BaTiO_3$, $(Ba,Sr)TiO_3$, $SrTiO_3$	Dielectric Pyroelectric, PTCR	Capacitor, Sensor Phase shifter Pyrodetector, Thermistor
$PbTiO_3$	Pyroelectric, Piezoelectric	Pyrodetector Acoustic transducer
$Pb(Zr,Ti)O_3$	Dielectric Pyroelectric Piezoelectric, Electrooptic	Nonvolatile memory Pyrodetector SAW substrates
$(Pb,La)(Zr,Ti)O_3$	Pyroelectric Electrooptic	Pyrodetector Waveguide, optical memory display, SHG
(Niobates) $Pb(Mg_{1/3},Nb_{2/3})O_3$	Dielectric Electrooptic	Capacitor, memory Waveguide
$LiNbO_3$ $LiTaO_3$	Piezoelectric Electrooptic	Pyrodetector, waveguide optical modulator, SAW, SHG
$KNbO_3$	Electrooptic	Waveguide, frequency doubler holographic storage
$K(Ta,Nb)O_3$	Pyroelectric Electrooptic	Pyrodetector Waveguide

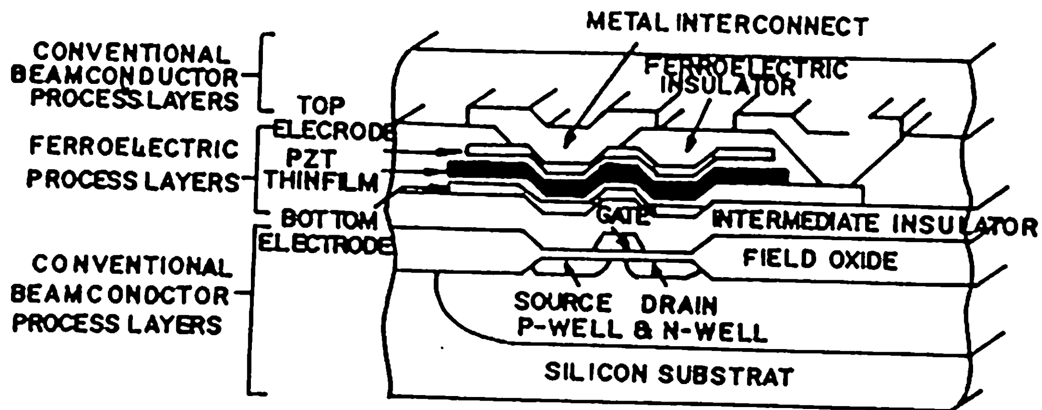

Figure 2.9: (Top) A cross-sectional view of Si-CMOS device with superimposed FE thin film switching memory and (Bottom) Schematic circuit of memory structure.

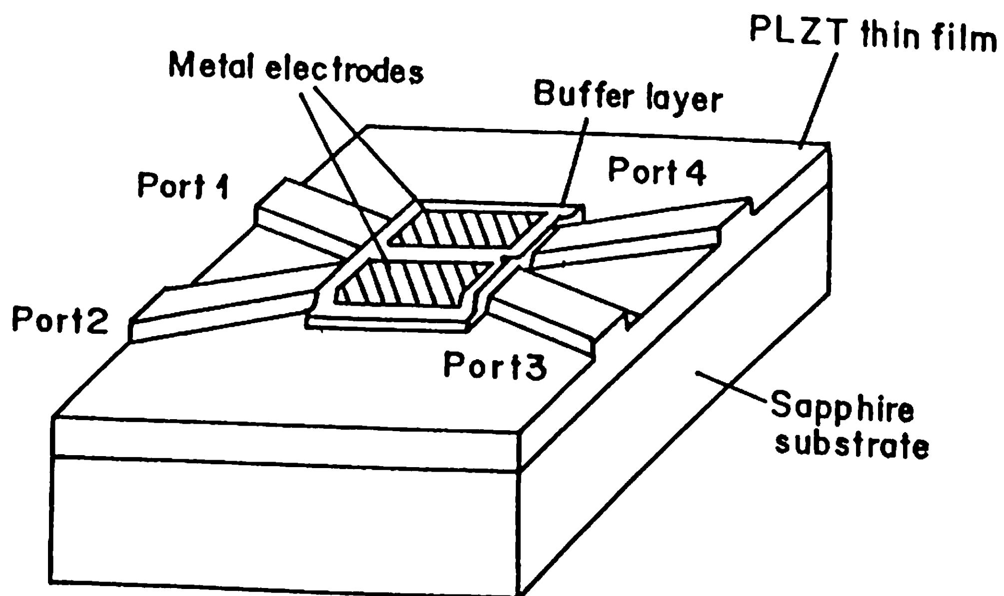

Figure 2.10: Configuration of TIR switch using a PLZT/sapphire structure.

sites are realized. The operating voltages were reduced from several 100 V to 5 V by reducing the thickness of the FE film from 0.1 mm for polished bulk wafers to 0.1-1 μm for thin films. The fatigue was reduced in the thin film compared to the bulk by virtue of a reduction in the piezoelectrically induced switching strain/stress resulting from the smaller size of the memory element.

An illustration of the FE random access memory (FERAM) cell cross section and a schematic diagram of the electrical circuit are given in figure 2.9. As seen from the schematic, the film serves as a memory switching capacitor in series with a transistor where source is connected to the bit line, the gate to the word line and the drain to the pulsed 5 V common. The polarization of the FE film switches to the opposite polarity when the transistor in turned on by the appropriate voltage on the gate. In order to interrogate the memory, it is pulsed and monitored for a given current/time wave form envelop, which is indicative of its polarization. Since the polarization state is directly readout (DRO), that state must be read back in to the cell again in order to preserve the original memory state.

An alternate memory scheme, whereby the FE film is placed in the gate area of the transistor is under development and has shown promising results. They are called FEMFET (FE memory field effect transistor). Its advantage is that it does not destructively readout the memory when it is interrogated. Hence they are referred to as non destructive type readout (NDRO) device [18].

In another memory device, a conventional DRAM, the capacitor consists of a diffuse phase, non memory FE film which replaced the present day SiO_2 capacitor with the exception that the FE films possess much higher dielectric constant and thus occupies much less area than SiO_2 [19]. This technology may be used in the future for multi megabit DRAM memories. The realization towards the above device is in progress.

All of the above devices have definite advantage for being both used a FE material and a thin film. These advantages include (1) no power required for memory (2) memory is permanent (3) fast switching at less than 10 ns (4) low operating voltage (5 V), (5) processing is compatible with silicon technology, (6) high dielectric constant from 200 to 2000 (7) high value of remanent polarization, 20-30 $\mu C/cm^2$, for

ease of memory state detection, (8) good dielectric breakdown strength 30-100 V/μm , (9) wide temperature range of operation from -55 to +125°C and (10) radiation hard characteristic. Some disadvantages of these devices are (1) temperature sensitive properties, (2) switching fatigue limited to 10^5 read/write cycle etc.

2.4.2 Integrated optic total internal reflection switch (TIR)

Thin film of PLZT and lithium niobate are excellent candidates for integrated optic circuits [16,17]. Figure 2.10 illustrates the typical configuration of a PLZT thin film TIR switch [20]. Optical wave guiding is confined to the stepped channel (500Åhigh) which is ion milled in to the PLZT film. Laser light input at port No.1 proceeds to port No.3 when no voltage is applied to the surface electrode but is switched to port No.4 with voltage applied. Speed of operation of thin device is in GHz with optical loss of 6dB/cm at wavelength of 1.06 microns.

2.4.3 Pyroelectric Infrared detector (IR optical FET)

The large value of pyroelectric coefficient for $PbTiO_3$ and PZT materials makes them very useful in IR imaging and detecting applications. The basic structure of a IR-OPFET (Infra Red-Optical Field Effect Transistor) is similar to that of a metal ferroelectric semiconductor FET structure having an IR absorbing gate electrode. This works on the principle that the IR absorbing gate electrode, which is sensitive to the infrared light, undergoes a polarization change induced by pyroelectric effect and thus modifies the drain current. The structure of an IR-OPFET is illustrated in figure 2.11 [21]

2.4.4 Erasable/Rewritable Optical Disc

PLZT thin films have shown their potential for application as optical information storage media, such as an erasable/rewritable optical disc. The large longitudinal electro-optic effect and high photosensitivity makes them very useful in developing this device. Due to the smaller grain size of these film, a storage bit size of the order of 1 μm may be feasible with this material. In this device optical information storage

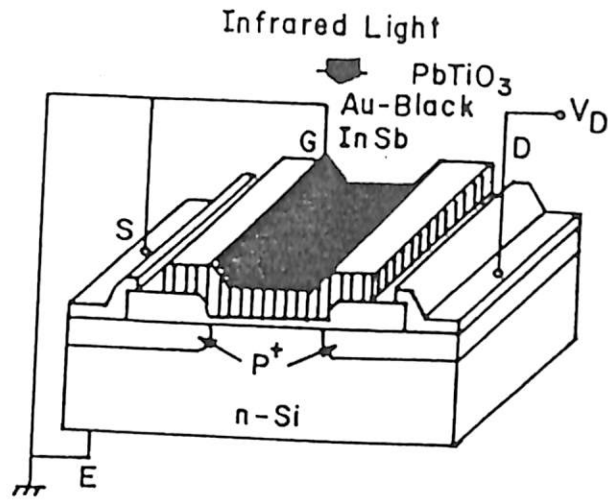

Figure 2.11: Schematic structure of IR-OPFET based on ferroelectric $PbTiO_3$.

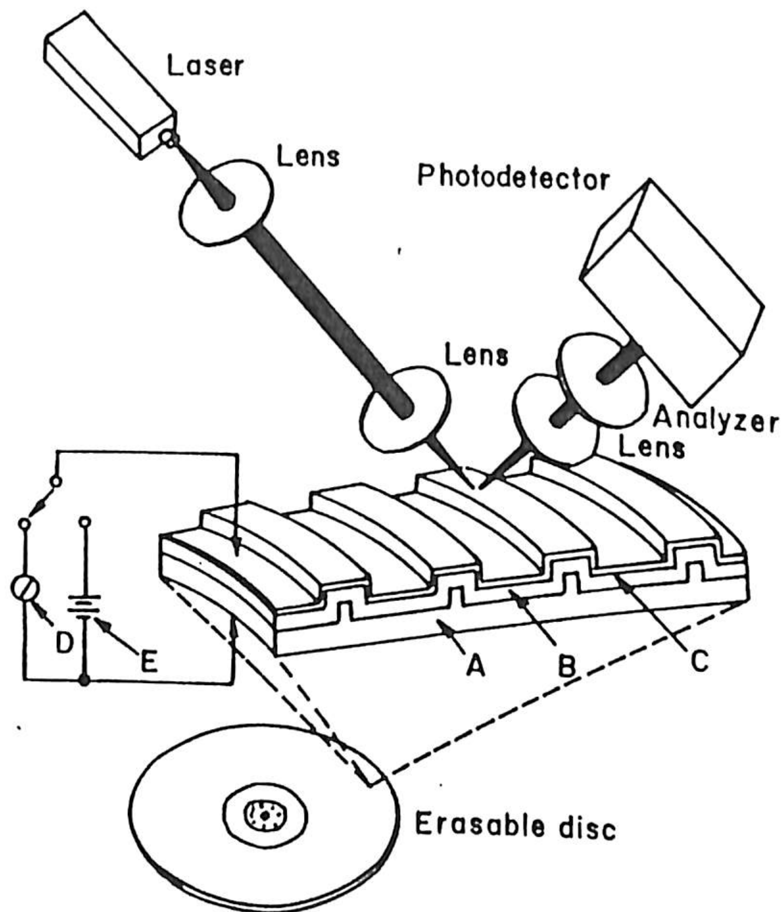

Figure 2.12: Schematic of Erasable/rewritable optical disc with PLZT ferroelectric thin film.

is achieved by applying a biasing field to induce a metastable ferroelectric phase, in antiferroelectric material like PLZT. The thin film is then exposed to write beam to store digital data in the desired areas. The illuminated regions undergoes a transition from FE to AFE phase, while the dark areas remain in the FE phase even after the removal of biasing field. Binary information is therefore stored in the metastable FE and stable AFE phase, and this stored information is nonvolatile . In other words the optical information is stored on as sequence of bits, whose phase is either AFE (digital 1) or FE (digital 0). To selectively erase optical information, the polarity of the dc voltage is reversed and the AFE bit to be erased are exposed to the write laser light. Thus new data can be recorded in the same areas. Figure 2.12 represents the schematic diagram of an eraseble/rewritable optical disc.

2.5 Desired features of ferroelectric thin films for electronic applications

The most important characteristic of a ferroelectric material for their efficient use in device fabrication is its spontaneous polarization behaviour and the ability of polarization reversal leading to bistability. There are many other parameters, which are to be considered while selecting them for technological applications.

2.5.1 Dielectric breakdown

The electric field at which the dielectric breaks down E_{Br} is an important parameter in the characterization of ferroelectric DRAM capacitors. The operating field across the capacitor must be designed to be less than the breakdown field if the capacitor is to be operated reliably. Limited data regarding this parameter indicates that in sputtered $BaTiO_3$ thin films the breakdown field decreases as the crystallinity of the film increases [22]. In polycrystalline films, the breakdown field is much smaller than that in the amorphous film. This seem to indicate that the breakdown field will decrease as the film thicknesses decreases because there are fewer grain boundaries and thus there are grater crystallinity (unless the film is amorphous).

On the other hand, some studies on ceramic samples indicate that thermal

mechanism contribute to the dielectric breakdown, and that thinner samples exhibits larger breakdown fields because there is less internal heating to contribute to breakdown [23,24]. Thin 100-600 nm KNO_3 film have also exhibited a breakdown field that increases with decreasing film thickness [25].

2.5.2 Leakage Current

One of the most important parameter to be considered during the material selection for DRAM capacitor cell is the leakage current of the dielectric material. If the leakage in the thin film is large, the stored charge will be lost from the storage capacitor over a period of time. This means the content of the memory cell will vanish with time and the cell has to be refreshed periodically to avoid this. From the available data for sputtered $BaTiO_3$ thin films, it is observed that the leakage current decreases as the crystallinity of the film decreases [22]. In amorphous $BaTiO_3$ thin films, the leakage current is atleast two orders of magnitudes less than in polycrystalline films. This is hold true for other ferroelectric materials also. Low leakage current thus prefers amorphous films but at the same time due to smaller value of dielectric constant of amorphous films, the charge storage density will be considerably reduced.

2.6 Reliability of Time Dependent Physical Properties

Similar to any other capacitor dielectric, there are many physical properties of a ferroelectric material that change with time like dielectric constant, remanent and saturation polarizations, coercive field, shape of hysteresis loop, dielectric breakdown field, loss tangent and leakage current. These time dependent mechanism that can affect the physical properties of ferroelectric materials are aging, fatigue and time dependent dielectric breakdown.

2.6.1 Aging

In an aged ferroelectric, the remanent polarization [26-28], coercive field [26-30], and loss tangent [31-33] are usually reduced. In some materials the saturation polarization

is found to remain constant in time [28]. The aging generally occurs in the ferroelectric phase [34] of the material. There are two dominant theories regarding the aging phenomena. They are based on (1) domain relaxation and (2) the development of space charge field. Both mechanism can clamp the domain of an aged sample so that the domain donot move and grow as they do in fresh samples [33]. This reduce their ability to contribute to the macroscopic polarization. The reorientation and clampings of the domain walls are due to lattice strain at the domain walls and grain boundaries [35]. Over time these strains are relieved through reorientation of domains [12,20,36-39]. The materials with larger internal strain age faster than those with smaller internal strains. As these samples are aged internal strain was found to be reduced [35]. Materials with smaller grains age very slowly because there is less room with in a grain to accommodate domain splitting and reorientation [40,41].

Second aging mechanism occurs due to the movement and pinning of charges at either the domain walls [42,43], grain boundaries or dielectric electrode interfaces. This mechanism has been found to have a larger effect in samples with smaller grain size [44,45]. In ferroelectric phase with zero external bias, this charge, which could be due to dopants, other impurities or vacancies aligns itself with the remanent polarization and creates an internal electric field in the direction opposite to the electric field associated with P_r .

When an external field is applied to reverse the polarization, the space charge field opposes the applied field. This effectively increase the magnitude of the applied field E_c required to induce polarization reversal. Once the polarization is reversed and the applied field is removed, the space charge field causes the part of remenant polarization to switch back to its original direction. This effect is called retention failure and this may effect in the reduction of P_r . Another effect of space charge is that it can prevent the domain from growing, which is required for polarization reversal thereby reducing the maximum polarization

If the material is in paraelectric phase, aging due to reorientation of domains should not be an issue, but if the material is under a constant dc bias as in DRAM's then free charges drift to the grain boundaries and setup an internal space charge field.

2.6.2 Fatigue

Fatigue occurs when the polarization in continuously reversed. The material response to fatigue is similar to the aging response. The remenant and maximum polarization may decreases and coercive field may increase [34,46,47] or decrease [47,48], the hysteresis loop loses its squareness [48,49] and microcracks often appears in the material [46,48,50]. If the polarization is never reversed, fatigue never occurs or is reduced to an insignificant level.

The mechanism behind fatigue is not well understood as that of aging and are not appreciably treated in the literature. Internal strain may be a fundamental cause for the change in the electrical properties. During polarization reversal there is an even grater strain within a sample because of the continuous structural change. Some of the strain is relieved through orientation and twinning of domains, and large strain may be relieved by spontaneous microcracking [48]. These microcracks can cause a permanent change in electrical parameters and might well produce catastrophic failure of the dielectric. As the grain size decreases or as the cell distortion decreases due to compositional variations, the microcracking has been found to reduce [51-53].

2.6.3 Time dependent Dielectric breakdown

Under a sufficient electrical stress, the dielectric material will breakdown over a time period. This property is the characteristic of intrinsic material, the procedures and quality of processing and the nature of electrode material [54-56]. Only very few information are available in this regard on ferroelectric materials.

2.7 Advances in processing of Ferroelectric Thin Films

Ferroelectric thin film synthesis is becoming an important field of activity due to its wide range of applications. The availability of new synthesis techniques [2] such as sol-gel , laser deposition, and metal organic chemical vapour deposition techniques (MOCVD) are stimulating new research and the knowledge obtained in the past years

Table 2.3: History of FE thin film fabrication techniques, their comparison and important features

Technique(Period)	Cost	Wet/Dry	Rate nm/min	T(°C) Substrate	Anneal	Problems
ARE (1990→)	High	Dry	—	—	—	—
Laser (1985→)	High	Dry	5–100	RT–700	500–700	Debris Uniformity
MOD (1982→)	Low	Wet	300/C	RT	500–800	High T_a
Sol-Gel (1982→)	Low	Wet	100/C	RT	500–800	Multiple coating
MOCVD (1980→)	High	Dry	5–100	400–800	600	High T_s
Magnetron (1975→) sputtering	High	Dry	5–30	RT–700	500–700	Target surface
Ion beam (1975→) sputtering	High	Dry	2–10	RT–700	500–700	Uniformity
RF-sputtering (1972→)	High	Dry	0.5–5	RT–700	500–700	Negative ions
Thermal (1956→) evaporation	High	Dry	10–100	RT–700	500–700	Rate control
Electron beam (1965→) evaporation	High	Dry	10–100	RT–700	500–700	Rate control

on the growth conditions suggest promising future.

The first synthesis of micron thick films were realized by flash evaporation of $BaTiO_3$ in 1955 [57]. Since then numerous materials and techniques have been developed [2,3]. Film deposition techniques which are numerous influence the composition and the microstructures of the film. The thin film deposition techniques can be genarally divided into dry process and wet process. Dry process include evaporation, sputtering, Laser techniques and CVD. They usually require hot substrates. They are relatively slow and expensive but allows grater ease of epitaxial film growth and are used widely. On the other hand wet process include metal organic decomposition (MOD), sol-gel etc. use unheated substrates. They are fast and inexpensive since they allow the preparation of 100-300 nm thick film per coating with good stoichiometry [58]. The history of ferroelectric thin films and comparison of most important features of technique of preparation are summarized in table 3 [59]. Some of the common deposition techniques used for making ferroelectric thin films are sputtering, laser ablation, MOCVD and hydrothermal process.

Ceramic materials can be evaporated by irradiating them with high power laser beam to make ceramic thin films. The evaporation may be done in ambient pressure or controlled partial pressure of oxygen [60]. The incident energy is localized within the optical absorption region and there is high probability that all species with in a small volume are evaporated simultaneously. A laser beam of wavelength usually in the near uv region is generally used for irradiation [60]. The laser beam is focused through a uv grade planoconvex lens on to the target at an angle 45° to the normal. The beam energy density of efluance can be varied by changing the laser spot size on the target by altering the distance between the focusing lens and the target. The evaporated target species are then deposited on to a substrate which is preheated or can be post annealed after deposition. By suitably selecting a substarte and maintaining a proper substrate temperature, epitaxial thin films of a veriety of ferroelectric thin films can be grown by laser ablation. The most important advantage of laser ablation is that it allows good epitaxial growth and the process is compatiable with the existing semiconductor technology.

Growth of different ferrolelectric thin films with good epitaxy has been reported

to be achieved by sputtering techniques such as rf and magnetron sputtering [61,63]. Sputtering of ferroelectric thin film is genarally done in oxygen/argon atmosphere. A sinterd target material of appropriate composition is used as the cathode of the sputtering system, in which a low discharge is established in an inert gas such as argon under reduced pressure by the application of high voltage. The substrate on which the film is to be deposited is placed on the anodeof the system. The stochiometry and the composition of the deposited films depends on the composition sputtering gas mixture and substrate temperature [61].

Metal Organic Chemical Vapour Deposition (MOCVD) is another major technique used in the deposition of high quality ferrolelectric thin films[64,65]. In this technique different volatile metallorganic compounds are sublimed separatly, mixed and allowed to decompose on the surface of a suitably preheated substrate. The success of MOCVD process depends on the volatility and the stability of the precursor material. Hydrocarbons based on β-diketonates are the most common precursor used in this techniques for oxide materials. The difficulty in contolling the stoichiometry is the major disadvantage of this technique.

Compared to the above discussed techniques, sol-gel process has may advantages. Sol-gel process is relatively less costlier and does not require complex instrumentation. Sol-gel process provides better homogeniety and stiochiometry. Sol-gel process allows the fabrication of large area coatings at low temperatures. Sol-gel can be easly tailored to achive desired final products with different properties. The major disadvantage of the sol-gel process in thin film preparation is the difficulty in achiving epitaxy in the grown films.

References

1. IEEE standard definition of primary ferroelectric terms. ANSI/IEEE std. 180, 1986.

2. G. H. Haertling *Ceramic Materials for Electronics*, ed. R. C. Buchanan (Dekker, New York 1986) P.139.

3. J. M. Herbert, *Ceramic Dielectrics and Capacitors: Electrocomponent Science Monograph*, vol. 6 (Jordan and Breach, New York, 1985).

4. W. Cochran, Phys. Rev. Lett. 3, 412 (1959).

5. P. W. Anderson *Fizica Dielektrikov*, ed. G. I. Skanavi (Moscow, Akad. Nauk. SSR. p.290).

6. W. Cook Jr. and H. Jaffer, *Piezoelectric ceramics* (Academic Press, New York, 1971).

7. G. A. Smolenskii and V. A. Isapov, Dok.Akad, Navk, SSR 97(1954) 653.

8. W. J.Merz, Phys.Rev. 76, 1221 (1949).

9. I. S. Zheludev and L. A. Shuvalov, Soviet Phys. Crystllogr. 1, 537 (1956).

10. J. F. Scott and C. A. Paz de Arauja, Science, 246 (1989) 1400.

11. G. C. Messenger and F. N. Coppage, IEEE Trans. Nac. Sci. 35 (1988) 1461.

12. M. Okayama and Y. Hamakawa, Ferroelectrics 63, 243 (1985).

13. K. Iijima, R. Takayama, Y. Tomita and I. Ueda, J. Appl. Phys. 60, 2914 (1986)

14. K. Screenivas and M. Sayer, J. Appl. Phys. 64, 1484 (1988).

15. D. R. Uhlmann, J. M. Boulton, G. Teowee, L. W. Weisenbach and B. J. Zelinski, Sol-Gel Optics, Proc. SPIE 1328 (1990) 270.

16. T. Kawaguchi, H. Adachi, K. Setsune, O. Yamazaki and K. Wasa, Appl. Opt. 23, 2187 (1984).

17. A. Wu. Proceedings of the Fourth SAMPE Conference, Albuquerque NM, June, 1990 pp.722.

18. D. Lampe, S. Sinharoy, E. Steipke, and H. Bubay, Proceeding of ISAF 90, Urbana, 11, June 1990 .

19. B.S anto. IEEE Spectrum 26, 47 (1980).

20. S. B. Krupanidhi, Proceedings of the Second Symposium on Integrated Ferro-electric, Monterey, Ca, March, 1990

21. K. Tanaka, Y. Higuma, K. Yokoyama, T. Nakagawa and Y. Hamakawa, Jpn. J. Appl. Phys. 15, 1381 (1976).

22. I.H. Pratt and S. Firestone, J. Vac. Sci. Tech. 8, 256 (1971).

23. R. Gerson and T. C. Marshall, J. Appl. Phys. 30, 1650 (1959).

24. B. C. Shin and H. G. Kim, Ferroelectrics, 77, 161 (1988).

25. F. Scott et al. ISAF, Bethlehem, Pa, pp. 569-71, June 8-11 (1986).

26. M. McQuarrie, J. Appl. Phys.24, 1334-35 (1953).

27. Z. Pajak and J. Stankowski, Acta Phys. Polom. pp. 1144-46 (1958).

28. K. Carl and K. H. Hardtl, Ferroelectrics 17, 473 (1978).

29. G. H. Jonker, J. Am. Cer. Soc. 55, 57 (1972).

30. W. Pan et al, J. Mat. Sci. Lett. 5, 647 (1986).

31. W. A. Shulze and J. V. Biggers, Ferroelectrics 9, 203 (1975).

32. K. W. Plessner, Proc. Phys. Soc. 69B, 1261 (1956).

33. S. Ikegami and J. Ueda, J. Phys. Soc. Jap. 22, 725 (1967).

34. R. C. Bradt and G. S. Ansell, J. Am. Ceram. Soc. 52, 192 (1969).

35. G. W. Taylor, J. Appl. Phys. 38, 4697 (1967).

36. A. Cohen et al., J. Am. Cerm. Soc. 53, 396 (1970).

37. G. Arlt, Ferroelectrics, 76, 451 (1987).

38. P. V. Lambeck and G. H. Jonker, J. Phys. Chem. Solids 47, 53 (1986).

39. K. Tsuzuki, Jap. J. Appl. Phys. 24 (Suppl. 24), 126 (1985).

40. M. Kuwabara et al., J. Am. Ceram. Soc. 71, C 110 (1988).

41. C. A. Miller, Brit. J. Appl. Phys. 18, 1689 (1967)

42. M. Takahashi, Jap. J.. Appl. Phys. 9, 1236 (1970).

43. S. Takashashi, Jap. J. Appl. Phys. 20, 95 (1981).

44. K. Okazaki and K. Nagati, J. Am. Ceram. Soc. 56, 82 (1973).

45. H. Neumann and G. G. Artt, Ferroelecttrics 76, 303 (1987).

46. W. R. Salaneck, Ferroelectrics, 4, 97 (1972).

47. D. B. Fraser and J. R. Maldonado, J. Appl. Phys.41, 2172 (1970).

48. W. C. Stewart and L. S. Consentino, Ferroelectrics 1,149 (1970).

49. J. R. Anderson et al., J. Appl. Phys. 26, 1387 (1955).

50. V. G. Gavrilyachenko et al., Sov. Phys. State 12, 1203 (1970).

51. R. W. Rice and R. C. Pohanka, J. Am. Ceram. Soc. 62, 559 (1979).

52. S. S. Chiang et al., Comm. Amer. Ceramic Soc. C141-43, Oct. 1981.

53. H. T. Chung and H. G. Kim, Ferroelectrics 76, 327 (1987).

54. T. N. Nguyen et al., Proc. of. Symp. on rel. of semiconductor Dev. and interconnection and Multilevel metallization, Interconnection, and Contact Tech. vol 86-9, 185 (1989).

55. P. Hiegrgeist et al., IEEE Trans. Elec. Dev. 36, 913 (1989).

56. I. C. Chen et al., IEEE Trans. Elec. Dev. ED-32, 413 (1985).

57. R. A. Roy., K. F. Etzdd and J. J. Cuomo, in Ferroelectric Thin Films, Mater. Res. Soc. Symp. Proc. 200, 141 (1990).

58. C. Feldman Rev. Sci. Instrum. 26, 463 (1955).

59. M. A. Aegerter, J. Non. Cryst. Solids 151, 195 (1992).

60. G. M. Davis, and M. C. Gower, Appl. Phys. Lett. 55 (2), 112 (1989).

61. K. Sreenivas, A. Mansing and M. Sayer, J. Appl. Phys. 62, 4475 (1987).

62. V. S. Dharmadhikari and W. W. Grannemann, J. Appl. Phys. 53, 8988 (1982).

63. J. K. Park and W. W. Grannemann, Ferroelctrics, 10, 217 (1976).

64. L. A. Wills, B. W. Wessels, D. S. Richeson, and T. J. Marks, Appl. Phys. Lett. 60 (1), 41 (1992).

65. B. S. Kwak, K. Zhang, E. P. Boyd, A. Erbil and B. J. Wilkens, J. Appl. Phys. 69 (2), 767 (1991).

Chapter 3

Experimental Techniques and Characterization

Thin dielectric films of $BaTiO_3$ and $SrTiO_3$ are prepared by sol-gel process and are characterized for their efficient use in a variety of new applications in microelectronics and integrated optics. Two diferrent combinations of starting materials are used in preparing $BaTiO_3$ thin films to understand the effect of starting materials on the structural and microstructural properties of these films. $BaTiO_3$ and $SrTiO_3$ thin films are characterized by X-ray diffraction(XRD), Scanning electron microscopy (SEM), Auger electron spectroscopy (AES) and optical transmission and absorption spectroscopy. FTIR spectroscopy has been used to analyze the structural changes occurring in the precursor films as they are cured at different temperatures. The electrical, dielectric and ferroelectric properties of these thin films are studied in MIS and MIM configurations.

3.1 Preparation of Multicomponent Oxide Thin Films of $BaTiO_3$ and $SrTiO_3$ by Sol-gel Process

For the preparation of sols for making multicomponent oxide thin films by sol-gel process, a variety of combination of starting materials can be used. In the production of two component systems, one can use (1) a mixture of metal alkoxides (2) one metal alkoxide and other metal salt. However, the mixture of two alkoxides is inconvenient

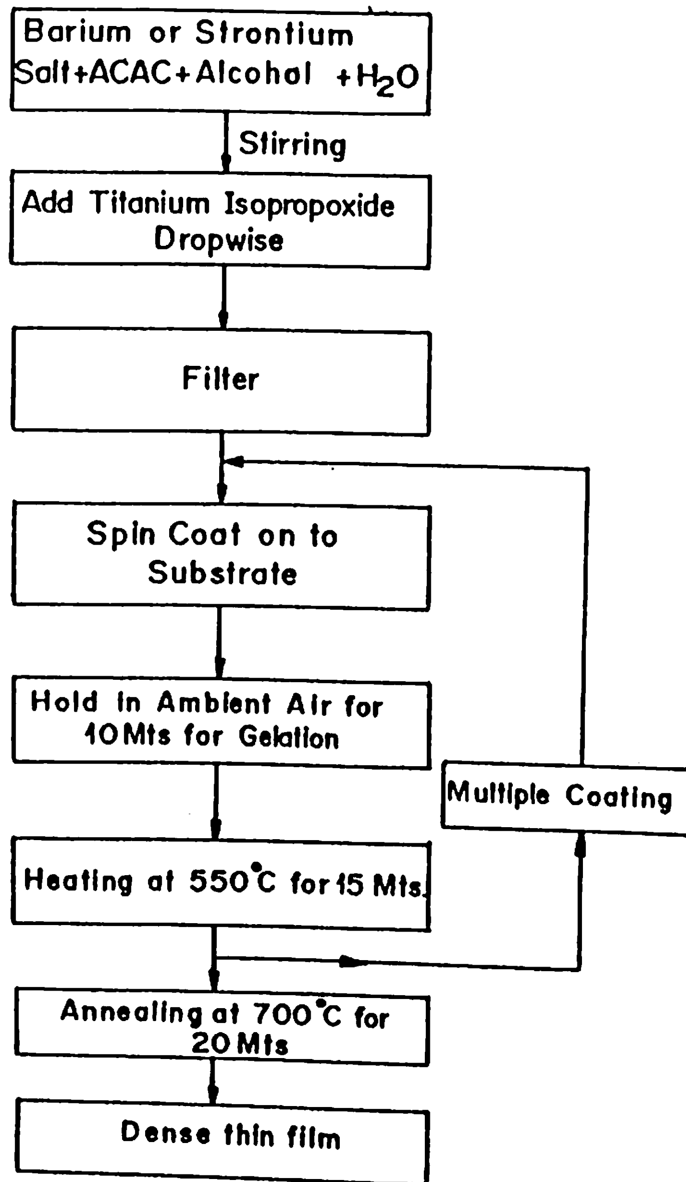

Figure 3.1: Flow chart showing the different stages in the fabrication of $BaTiO_3$ and $SrTiO_3$ thin films by sol-gel process.

for preparing multicomponent oxides thin films.This is due to the fact that the metal alkoxides vary in hydrolyzing ability, as well as solubility in common solvent depending on the kind of metal atom and the alkoxy group(s) presents in it. The use of metal alkoxide together with suitable metal salt generally give acceptable results. The quality of the film can be improved by using some chelating agents like acetylacetone, dibenzo acetyl acetone etc. Figure 3.1 represent the flow chart for making $BaTiO_3$ and $SrTiO_3$ thin films by sol-gel process used in this study.

3.1.1 Preparation of $BaTiO_3$ sol from Ti(OPr)4 and barium 2-ethyl hexanoate (EH precursor)

Sol for making $BaTiO_3$ thin films were prepared by using titanium isopropoxide and barium 2-ethyl hexanoate as precursors, referred to as EH precursor. Barium 2-ethyl hexanoate was synthesized by reacting 0.1 mol of $Ba(OH)_2.8H_2O$ (31.54 grams) and 0.2 mol of ethyl hexanoic acid (C_7H_15COOH) in 200 ml of methanol. The reaction takes place as following:

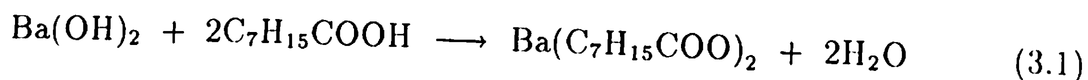

$$Ba(OH)_2 + 2C_7H_{15}COOH \longrightarrow Ba(C_7H_{15}COO)_2 + 2H_2O \qquad (3.1)$$

The clear solution obtained by the above reaction was filtered to remove unreacted particulates. Methanol was distilled off from the solution and residue was dried in an oven at 110°C for 24 hrs. to give barium 2-ethyl hexanoate as a white waxy substance soluble in methanol. This has been used as the barium precursor along with $Ti(OC_3H_7)_4$ for making $BaTiO_3$ sol. 4.23 grams of barium 2-ethyl hexanoate was dissolved in 24 ml of methanol and 1 ml acetyl acetone. 0.02 mol of water was added for hydrolysis. To this mixture 2.95 ml of $Ti(OC_3H_7)_4$ was added under constant stirring. Addition of acetyl acetone helps in getting clear solution. The solution was then refluxed at 80°C for 2 hrs and the filtered using Whatmans glass micro fiber filters GF/C and stored in sealed bottles.

3.1.2 Preparation of $BaTiO_3$ sol from $Ti(OC_3H_7)_4$ and barium hydroxide (ME precursor)

31.5 gms of barium hydroxide (GR, Loba, Chemie, India) was dehydrated by keeping it in an oven at 250°C for 24 hrs in vacuum and dissolved in 20 ml 2-methoxyethnol (GPR, BDH, India) by refluxing the mixture at 110°C for 1 hour. The solution is then cooled down and titanium isopropoxide was added dropwise to get a clear brown solution. It was reflexed at 80°C for 2 hrs. and then filtered using glass fiber filters. The filtered sol was then spin coated on to substrate at 3000 rpm for making $BaTiO_3$ thin films.

3.1.3 Preparation of $SrTiO_3$ sol from strontium 2-ethyl hexanoate and $Ti(OC_3H_7)_4$

Strontium 2-ethyl hexanoate was prepared by dissolving 0.1 mol of dehydrated $Sr(OH)_2.8H_2O$ in 0.2 mol of ethyl hexanoic acid. The reaction takes place according to the reaction,

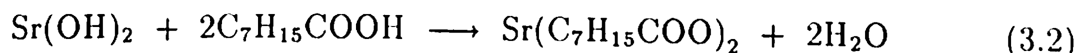

$$Sr(OH)_2 + 2C_7H_{15}COOH \longrightarrow Sr(C_7H_{15}COO)_2 + 2H_2O \qquad (3.2)$$

Ethanol is used as a solvent for the above reaction. After the reaction was complete, the solution was distilled to remove ethanol and the residue was dried at 110°C for 24 hrs in vacuum oven. Strontium ethyl hexanoate obtained in this way was a white crystalline powder. 3.74 grams of (0.01 mol) of strontium ethyl hexanoate was then dissolved in 25 ml ethanol and 1 ml acetyl acetone. 0.2 ml of water was added for hydrolysis. To this solution 2.95 ml of $Ti(OC_3H_7)_4$ was added under constant stirring. The final solution was then reflexed at 80°C for 1 hour to make the reaction complete. The solution is then filtered and spin coated on different substrates at 3000 rpm.

3.2 Sample Preparation

Samples for different studies were made by spin coating corresponding sols on appropriate substrates. Thin films of desired thickness were made by multiple coatings of the precursor solution.

3.2.1 Sample preparation for structural and optical characterization

Samples for studying XRD, SEM and UV-visible optical spectroscopy are made on fused silica and single crystal silicon substrates. For FTIR studies samples were made on high purity, KBr single crystals. The compositional analysis on $BaTiO_3$ thin films were done on samples made on platinum strips. The precursor solution for $BaTiO_3$ and $SrTiO_3$ are spin coated on to these substrates at 3000 rpm and kept at ambient atmosphere for about 10 minutes for hydrolysis of the alkoxide. The films were then fired at about 400°C to remove organics from the film. For making thicker films this coating-firing cycles were repeated number of times. The thickness of a single coating generally obtained was from 0.15 to 0.3μm .

3.2.2 Preparation of MIM and MIS structures

For making MIM structures, the substrates used for depositing films were platinum strips, platinized silicon wafers and stainless steel plates. Films of thickness varying from 0.5 to 2.5μm were deposited on to these substrates by multiple coating and firing of the precursor solution. After obtaining a film of desired thickness it was then annealed at temperature 600°C to 800°C to make them crystalline. The films were generally annealed at the above temperature range for 15 minutes. Gold or silver dots of 1 mm diameter were then vacuum evaporated on to these films at 150°C using a mask to make the top electrode. The substrate serves as the bottom electrode and the silver or gold dots as the top electrode of the MIM structure.

P-type silicon wafers having a resistivity of about 10 ohm-cm were used to deposit insulating thin films for making MIS structures. To make VLSI grade MIS structure, the cleaning of silicon wafer is very important. The silicon wafers were etched in 10% hydrofluoric acid prior to film deposition for the removal of SiO_2 from the surface. The etched silicon wafers were then held above isopropanol vapour and then dried in nitrogen gas jet. The sol gel precursor solution was then spin coated on to silicon wafers at 3000 rpm. After deposition the samples were held in humid and dust free atmosphere for 10 minutes for hydrolysis. The films were then fired at

$400^{o}C$ to remove organics. Multiple coatings were done to get desired thickness of the film. The thickness of the films can vary from 100Åto 2000Åby adjusting the amount of solvent used for making the sol. After obtaning a film of desired thickness, it was then annealed at higher temperatures to get desired phase. For making crystalline $SrTiO_3$, the films were annealed above $650^{o}C$ and amorphous $BaTiO_3$ thin films were made by annealing the films around $400^{o}C$.

The selection of gate electrode is very important for making a device grade MIS structure. The important parameters which must be considered for a proper choice of a material for gate electrode are (1) The difference in work function of the silicon substrate and gate electrode material, (2) adherence of gate material to the silicon and the dielectric thin film,and (3) the processing temperature should be compatibile with silicon technology. In the present study aluminum is used as the gate electrode material in fabricating MIS structure, for its low work function ensure ohmic contact with silicon and its good adherence with silicon and oxide dielectric materials. Circular aluminum gate of diameter 1 mm and thickness $1\mu m$ were deposited on the dielectric by vacuum evaporation using proper masks. Evaporation was carried out in high vacuum unit by thermal heating from tungsten filament.

Ohmic back contacts to p-type silicon was formed by depositing $1\mu m$ thick aluminum film on the back of the wafer by thermal evaporation, followed by low temperature annealing ($150^{o}C$) for a short duration (5 min). Aluminum was used to make back contact due to the fact that, Al can makes p-type silicon even stronger p-type and thus reduce the barrier height for holes to surmount. This reduces the resitance for current flow in both directions. Again to make the ohmic contact proper, silicon wafers with rough back side were used. Some times the wafer has to be abraded using emery cloth to create surface damage or roughness. In addition, the damaged region, electrically equivalent to a diffused degenerated layer, helps in achieving good ohmic contact.

3.3 Thickness Measurements

The thickness of the sol-gel derived thin films were first determined with the help of a Surfometer SF 200 and the result were then compared with the thickness calculated from the optical transmission spectra. For measuring the thickness of the films using the Surfometer, first a single coating of the precursor solution was made on a glass substrate and annealed at 400°C . The surface of the film was then covered with a small rectangular strip of Cello tape and the exposed region was dissolved in concentrated hydrochloric acid. The film was then washed and annealed at 500°C . The thickness of the multiple coated films were determined multiplying the thickness value obtained for a single coating by the total number of coatings made. The value of the thickness of the film after making a number of coatings was also mesured with the Surfometer to compare with the previous result. The thickness values measured from different methods mentioned were in good proximity with each other.

3.4 Characterization of Sol-gel Derived $BaTiO_3$ and $SrTiO_3$ Thin Films

For the efficient use of dielectric thin films for a various of applications, it has to be properly characterized for the reproducibility and optimization of process parameters. Different experimental methods are currently used for the characterization of thin films for electronic, optical, mechanical and sensor applications. Structural and microstructural characterization of thin films were done using Scanning electron microscopy, X-ray diffraction spectroscopy, FTIR spectroscopy, UV visible transmission spectroscopy and Auger electron spectroscopy.

3.4.1 Scanning Electron Microscopy (SEM)

Scanning electron microscopy has been used to study the microstructure and surface morphology of the films used in the present study. Due to the insulating behaviour of the $BaTiO_3$ and $SrTiO_3$ thin films, the surface of the films were coated with a thin layer of gold of about 100Åthickness. The coating has been done by R.F sputtering

in argon atmosphere at a pressure of about 10^{-6} torr. To see the microstructure and surface morphology of the samples, a JOEL JSM 35 CF Scanning electron microscope was used, which gave a direct observation of the crystallites and diffrent phases existing on the sample surface.

Figure 3.2(a) and (b) shows the electron micrograph of $BaTiO_3$ thin films made on platinum substates at 700°C and 750°C from EH precursor solution. Both the films show a smooth surface without any cracks or voids. The films annealed at 700°C shows formation of small crystallites whereas that annealed at 750°C shows bigger crystallites and comparatively larger area of the surface covered with crystallites than that annealed at 700°C . In general, crystalline and amorphous phases were found to coexist on the film surface. The mechanism of electrical conduction in these films are explined on the basis of a model suggested by the electron micrographic observations. The detailed discussion on the electrical properties of the sol-gel derived $BaTiO_3$ thin films used in the present investigation is given in chapter 5. Figure 3.3(a) and (b) show scanning electron micrograph of the surface of the sol-gel grown $SrTiO_3$ thin films on silicon wafer and stainless steel respectively. The films were annealed at 700°C for 15 minutes and allowed to cool down to room temperature in 1 hour. The films did not show any cracks but very fine pores of about $0.1\mu m$ size could be seen on the surface. Well defined $SrTiO_3$ microcrystals of about $0.5\mu m$ in size were seen on the film grown on both the substrates. The film surface shows, in general, a mixture of crystalline and amorphous phase. On the basis of SEM observations the electrical properties of the $SrTiO_3$ thin films grown by sol-gel process are explined by considering the film as a series combination of amorphous and crystalline regions of differnt conductivities. Here, a conduction mechanism of Maxwell-Wagner type due to the inhomogenieties existing in the material is found satisfactory in explaining the observed electrical properties. The electrical properties of the $SrTiO_3$ thin films used in this study are disscused in chapter 6.

3.4.2 X-ray Diffraction Analysis

To analyze the crystallographic structure of the samples X-ray diffraction techniques was used. The X-ray diffraction spectra of the samples were recored with Seimens

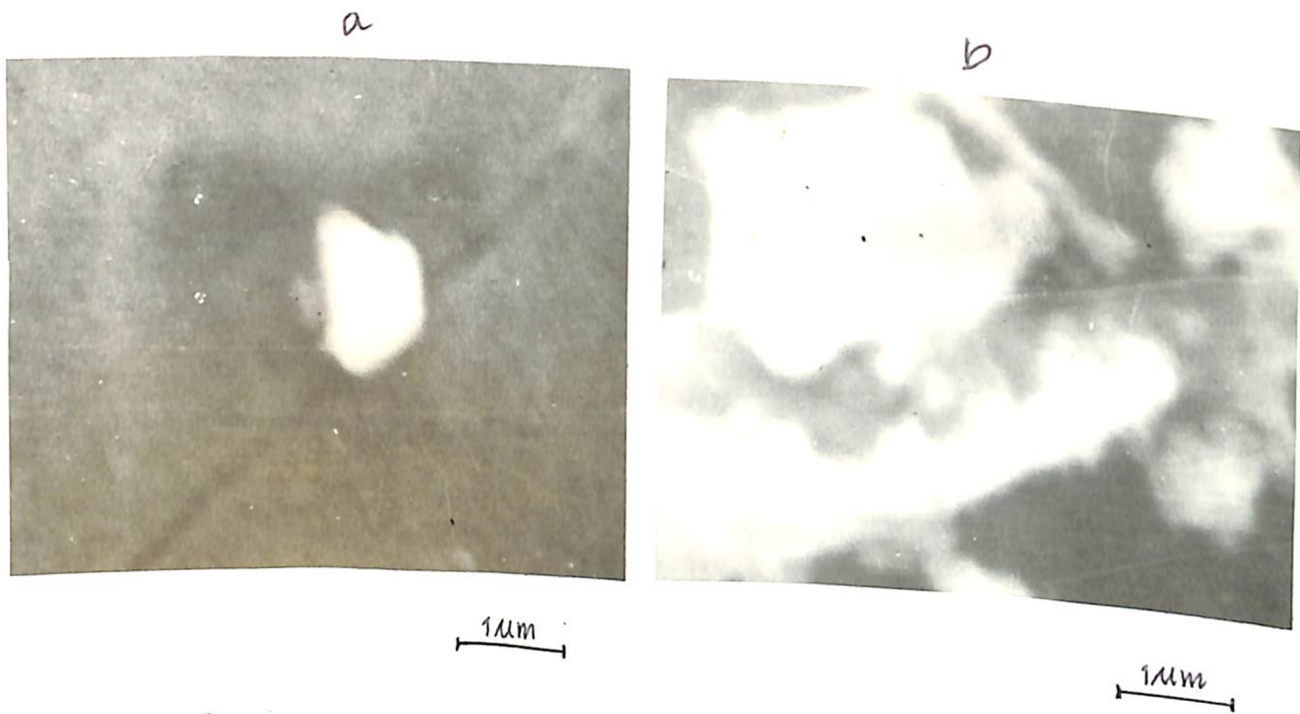

Figure 3.2: Scanning electron micrographs of $BaTiO_3$ thin films deposited on Pt substrates and annealed at (a) 700 °C and (b) 750 °C for 15 minutes.

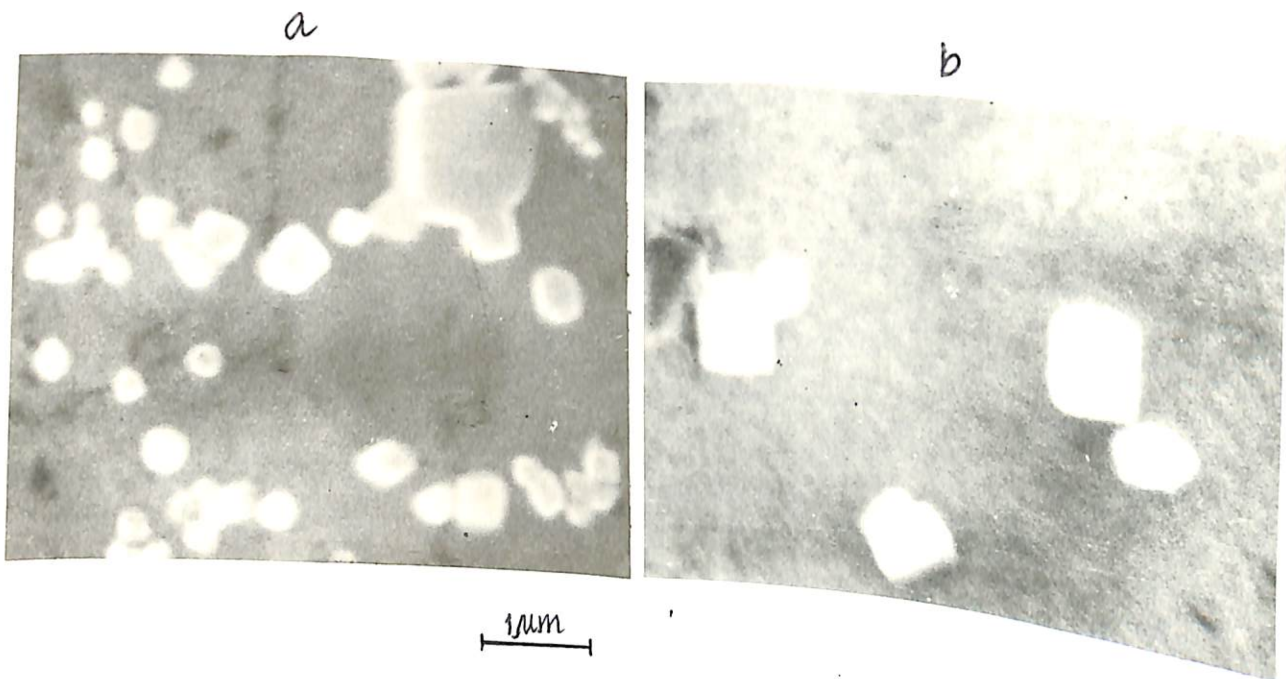

Figure 3.3: Scanning electron micrographs of $SrTiO_3$ thin films deposited on (a) silicon wafer (100) and (b) stainless steel by sol-gel process and annealed at 650 °C for 15 minutes.

Investigation on the Structural, Optical, Dielectric and Ferroelectric Properties of sol-Gel Synthesized Barium Titanate and Strontium Titanate Thin Films

Thesis
Submitted in partial fulfilment of the requirements
for the degree of

DOCTOR OF PHILOSOPHY

By

N. DEEPAK KUMAR

Under the Supervision of
DR. M.N. KAMALASANAN

[illegible]A INSTITUTE OF TECHNOLOGY AND SCIENCE
PILANI (RAJASTHAN) INDIA

1995

500 D X-ray diffractometer and Phillips PW 1840 X-ray diffractometer using K_α x- ray radiation of wave length 1.54A. In Phillips PW 1840 X-ray diffractometer, the diffraction pattern were recorded with an X-Y recorder from higher θ values to lower θ values. From the position of the diffraction peaks in the spectra, the d values were calculated using the Bragg's relation $n\lambda = 2d\sin\theta$. Seimens 500 D X-ray diffractometer used was interfaced with computer which directly gives the d values corrsponding to the diffraction peaks.

Figure 3.4 represents the X-ray diffraction pattern of $BaTiO_3$ thin film deposited on singlecrystal silicon wefer (100) using barium 2-ethyl hexanoate and $Ti(OC_3H_7)_4$ as starting materials. The films were annealed at 700°C for 15 minutes. The d values corresponding to XRD peaks were in good agreement with that of ASTM (American Standard for Testing and Materials) values (data card no. 5-626) for tetragonal barium titanate powder diffraction data. There is no unaccounted peaks observed in the crystallized films spectra showing that no unwanted crystallographic phases such as BaO, Ba_2CO_3 and $Ba_2Ti_9O_20$ were formed. Even though the peaks corresponding to (001) and (100) were not resolved to show the tetragonal nature of the crystallites, the combination of (002) and (200) peaks were sufficientlyy broadened to suggest that the crystallites may have a tetragonal structure. Further, the observation of ferroelectricity in the films used in this study also confirms the tetragonal structure. The d values calulated from the XRD spectra were a=b=3.995Åand c=4.05Å. X-ray diffraction spectra of sol-gel derived $SrTiO_3$ thin films deposited on fused silica substartes and annealed at 700°C for 15 min. at ambient atmospheric conditions is shown in figure 3.5. The diffractogram shows well defined peaks indicating a good deal of crystallinity. The d values of diffraction and the peak intensities agree very well with those given in the ASTM data cards (#5-643) for $SrTiO_3$, suggesting that the films were polycrystalline and microcrystals were of cubic structure having lattice constant a=b=c=3.90Å.

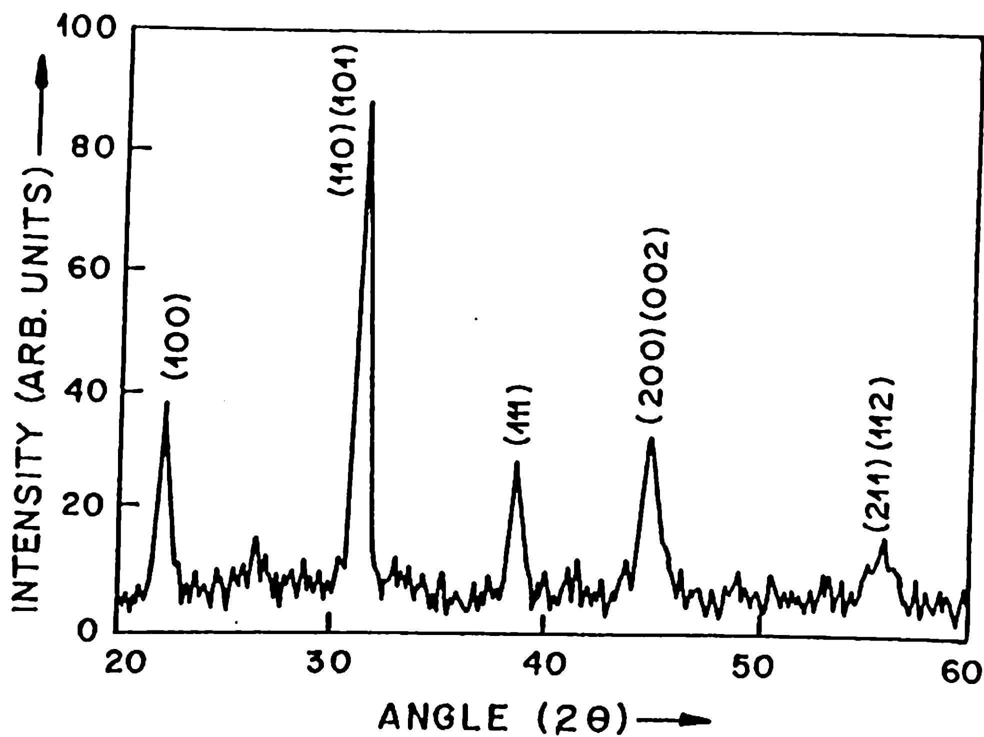

Figure 3.4: XRD pattern of $BaTiO_3$ thin film deposited on silicon wafer (100). Tetragonal splitting is seen at higher θ values.

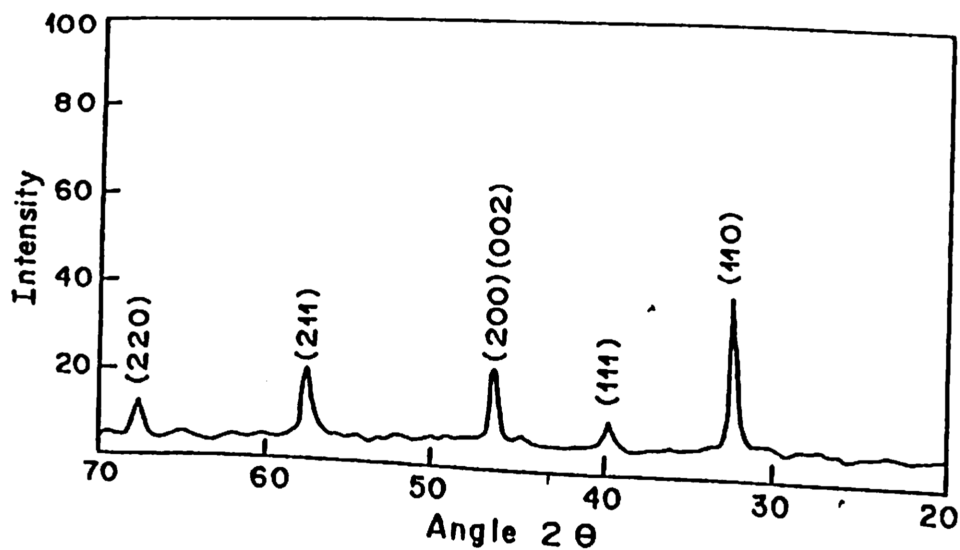

Figure 3.5: XRD pattern of $SrTiO_3$ thin film deposited on fused quartz.

3.4.3 Auger electron spectroscopic studies on $BaTiO_3$ thin films

The compositional analysis of the film and the interface were performed using Auger electron spectroscopy (AES), in conjunction with ion sputtering. AES is one of the most effective tools for the compositional analysis of thin films, surfaces and interfaces. The energy of Auger electrons is characteristic of the atom emitting it and hence the electron flux can be measured for chemical analysis. For the analysis of the buried interfaces, the upper layers are sputtered away using 3 kV argon ions. The experiments were performed in an ultrahigh vacuum system (Varian Associates VT-112) at a base pressure of $10^{-}10$ mbar. A single pass cylindrical mirror analyzer (CMA) Varian model 981-2707 (Energy resolution 0.18% and energy measurement accuracy better than 0.5 eV) with an integral coaxial 0-10 kV electron gun whose incident beam was at an angle 30° to the sample normal was used to obtain AES spectra.

Auger electron spectroscopic studies were carried out on 200 nm thick $BaTiO_3$ thin films deposited on platinum substrates at 700^oC . The surface of the film was cleaned by sputtering off a very thin layer of the film by argon ion bombardment. The spectra were then recorded after every 2 minutes of etching until the characteristic peaks due to the platinum substrate were prominent.

Figure 3.6(a) shows the Auger electron spectra of the sample recorded after 2 minutes of etching. The calculation of percentage composition showed that the thin films made by sol-gel were having good stoichiometry. The figure 3.6(b) shows the spectra of the sample recorded after 20 minutes etching. The figure shows a reduction in intensity of the peaks due to Barium, titanium and oxygen along with the emergence of characteristic peak due to platinum. Figure 3.6(c) indicates the spectra recorded after 25 minutes of etching. There is hardly any peak corresponding to the constituents of the film seen in the spectra, but it shows a very prominent peak due to platinum along with an enhanced peak due to carbon. It is clear from the profile that carbon was present in the platinum substrate as an impurity.

To understand about the compositional homogeneity in the film, the arbitrary

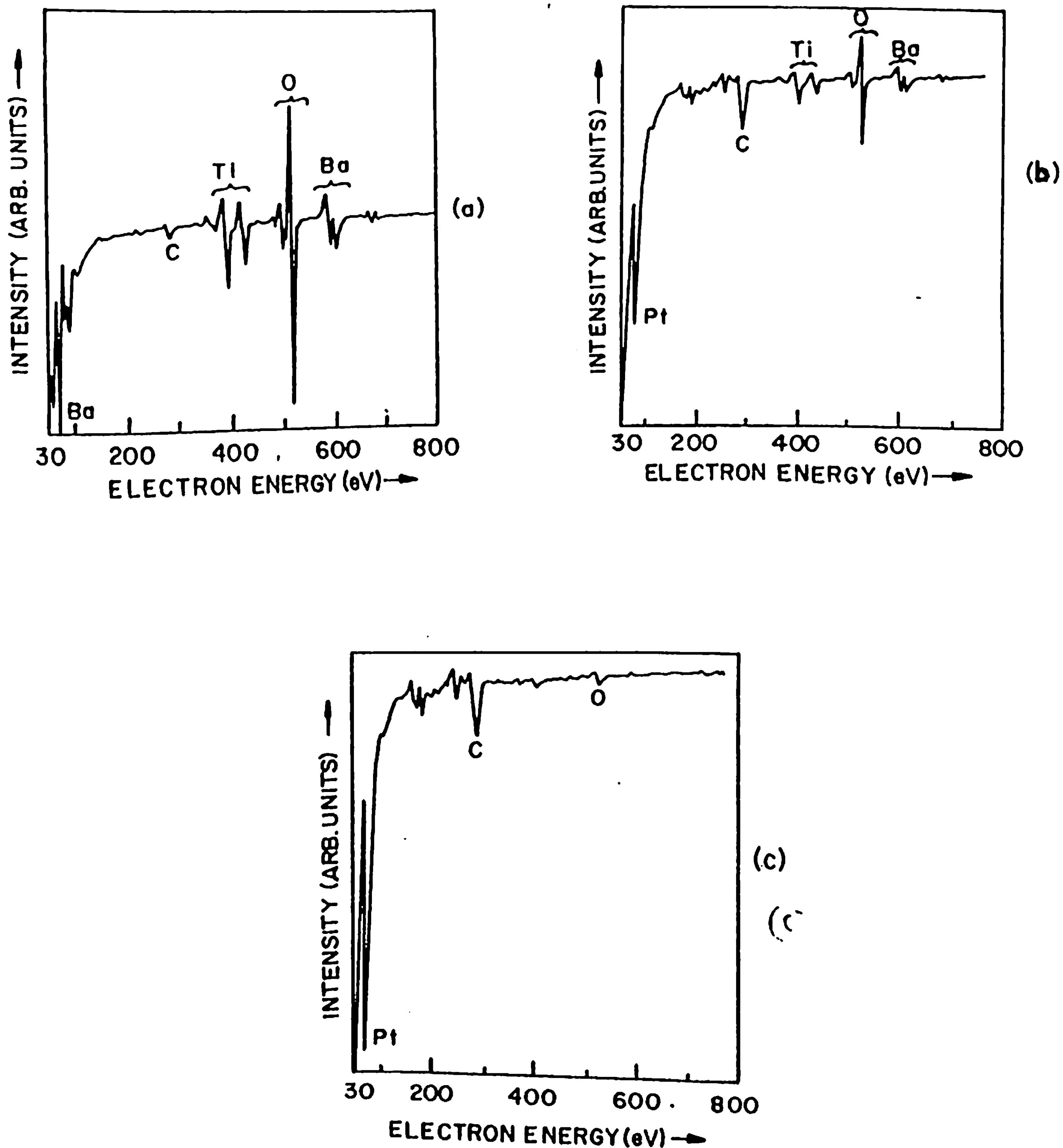

Figure 3.6: Auger electron spectra of $BaTiO_3$ thin films deposited on Pt strip after etching for (a) 2 min., (b) 20 min. and (c) 25 min.

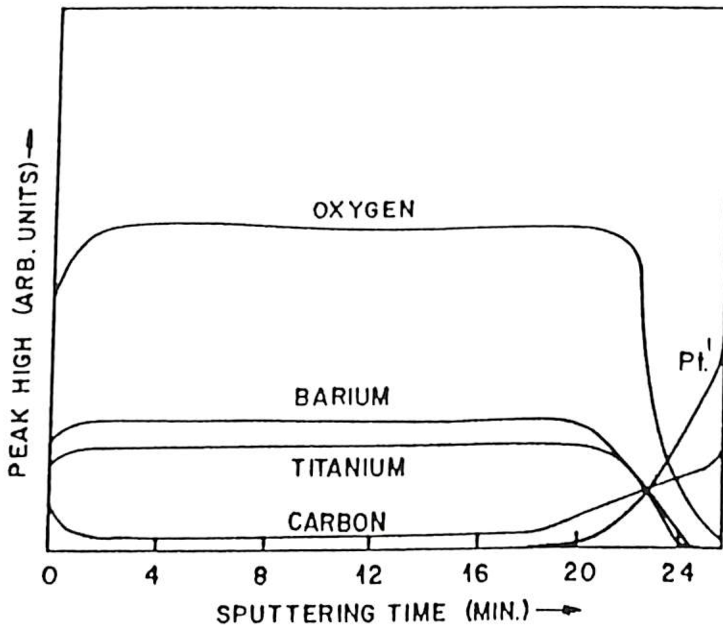

Figure 3.7: Auger depth profile of $BaTiO_3$ thin films as a function of etching time.

peak heights of different constituents were plotted as a function of etching time as shown in figure 3.7. The depth profile showed a good degree of homogeneity in the film and a reasonably sharp film substrate interface. the width of the interface roughly calculated was about 8 nm. The nature of the interface generally affects the electrical and dielectrical properties of these thin films.

3.5 Optical Characterization: UV-Visible specroscopy

The UV-visible spectroscopy studies were carried out using Shimadzu, Model 160 A spectrophotometer. For UV-visible studies films were deposited on fused silica substrates and were cured at temperatures ranging from 300 to 900°C . The substrates were coated with the precursor solution 5 to 6 times to get a thickness of around 1μm after curing at 300°C . Without proper curing of the previously deposited layer, further coating was difficult and this was giving rise to poor quality films. Therefore the measurements were not performed below 300°C . Films of initial thickness of the order of 0.1 to 0.4μm were not used for UV-visible study due to the absence of interference maxima and minima in their transmission spectra taken after curing them at higher temperatures.

UV-visible optical transmission spectroscopic studies were done on $BaTiO_3$ and $SrTiO_3$ thin films to evaluate the band gap, refractive index, and thickness of these films, which in turn give knowledge about the crystallinity, densification and compaction in these thin films. As the films changes from amorphous to crystalline phase the optical bandgap decreases and refractive index increases. A change in thickness for samples annealed at different temperatures were used to evaluate qualitatively the degree of compaction during the required phase formation.

3.5.1 Determination of Refractive Index and Thickness from Optical Transmission Spectra

Optical transmission spectra of $BaTiO_3$ and $SrTiO_3$ thin films deposited on fused silica substrates of thickness 1 mm were used for the calculation of refractive index, thickness and band gap of these films. The measurement of transmission T of light

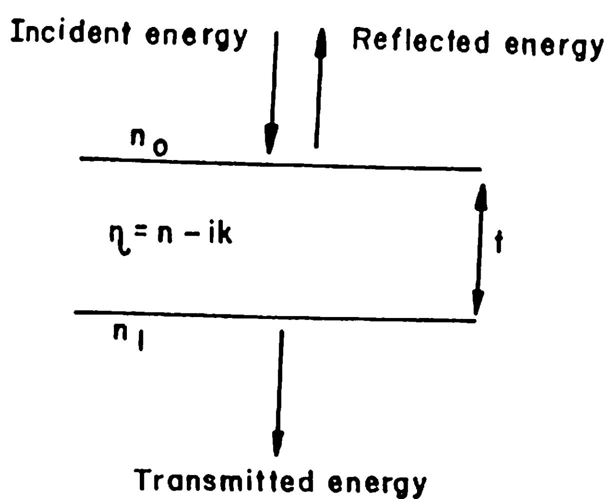

Figure 3.8: Schematic representation of a dielectric thin film of complex refractive index $\eta = n - ik$.

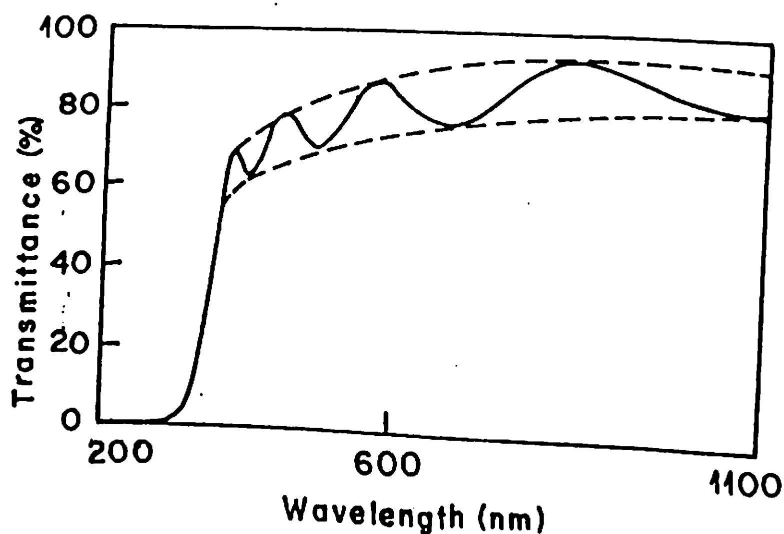

Figure 3.9: optical transmission spectra of polycrystalline $BaTiO_3$ thin film on fused silica subtrate. The dotted lines shows the envelope curve for calculating the optical constants by the method adopted by Manifacier et al [4].

through a parallel faced dielectric in the region of transparency can be used to determine the refractive index and thickness of weakly absorbing thin films. Hall and Fergusion [2] and Miloslaviskii[3] developed a method using successive approximations and interpolations to calculate these parameters. J.C.Manifacier et al [4] has developed a simplified method for the calculation of these parameters using the maxima and minima in the interference pattern in the optical transmission spectra of thin films. Figure 3.8 represents structure of a dielectric thin film of complex refractive index $\eta = (n - ik)$ and thickness t on a substrate of refractive index n_1. The quantity n_o represent the refractive index of air Consider a unit amplitude for the incident light in case of normal incidence, the amplitude of transmitted light is given as:

$$A = \frac{t_1 t_2 \exp(-2\pi i\eta t/\lambda)}{1 + r_1 r_2 \exp(-4\pi i\eta t/\lambda)} \tag{3.3}$$

where t_1, t_2, r_1, r_2 are the transition and reflection co-efficient at the front and back surfaces of the film. The transmission of the film is given by

$$T = \frac{n_1}{n_o} | A |^2 \tag{3.4}$$

In the case of weakly absorbing films $k^2 \ll (n - n_o)$ and $k^2 \ll (n - n_1)$, the transmission is given as

$$T = \frac{16 n_o {n_1}^2 \alpha}{{C_1}^2 + {C_2}^2\alpha^2 + 2C_1 C_2 \alpha cos(4\pi nt/\lambda)} \tag{3.5}$$

where $C_1 = (n + n_o)(n_1 + n)$, $C_2 = (n + n_o)(n_1 + n)$ and

$$\alpha = \exp(-4\pi kt/\lambda = \exp(-Kt) \tag{3.6}$$

K is the absorption co-efficient of the film.

Outside the region of fundamental absorption ($h\nu > E_g$) or free carrier absorption (higher wave lengths), the dispersion in n and k will be less and the condition for interference maxima and minima in the transmission spectra is given as

$$4\pi\ nt/\lambda = m\pi \tag{3.7}$$

where m is the order number of the fringes. Using this condition, the value of transmission at maxima and minima are given as

$$T_{max} = 16 n_o n_1 n^2 \alpha/((C_1 + C_2\alpha)^2 \tag{3.8}$$

$$T_{min} = 16 n_o n_1 n^2 \alpha/((C_1 - C_2\alpha)^2. \tag{3.9}$$

Figure 3.9 represents the transmission spectra of $BaTiO_3$ thin film made by sol-gel process. The dotted lines in the figure shows the envelop curve covering the interference maxima and minima. This has been used to calculate the optical constants of the film using the method adopted by Manifacier et al [4]. The films were deposited on fused silica substrates and annealed at 700°C for 15 minutes. Considering T_{min} and T_{max} as a continuous functions of λ through $n(\lambda)$ and $\alpha(\lambda)$, which forms the envelopes of the T_{max} and T_{min} in transmission spectrum as shown in figure 3.9, the ratio of T_{max} and T_{min} from the above equations 3.8 and 3.9 can be written as,

$$\alpha = \frac{C_1[1 - (T_{max}/T_{min})^{1/2}}{C_2[1 + (T_{max}/T_{min})^{1/2}]} \tag{3.10}$$

Then from equation 3.8,

$$n = [N + (N^2 - {n_o}^2{n_1}^2)^{1/2}]^{1/2} \tag{3.11}$$

where

$$N = \frac{{n_o}^2 + {n_1}^2}{2} + 2n_o n_1 \frac{T_{max} - T_{min}}{T_{max}T_{min}} \tag{3.12}$$

Thus by determining the value of T_{max} and T_{min} for a particular wavelength from the envelope curve and the refractive index of the film n can be explicitly determined.

The thickness t of the film can be calculated from two adjacent maxima or minima using equation (7) as

$$t = \frac{M\lambda_1\lambda_2}{2(n(\lambda_1)\lambda_2 - n(\lambda_2)\lambda_1)} \tag{3.13}$$

where M is the number of oscillations between two selected maxima or minima. M=1 for two adjacent maxima or minima and λ_1, λ_2, $n(\lambda_1)$ and $n(\lambda_2)$ are the corresponding wavelengths and indices of refraction.

3.6 Determination of Optical Band Gap

The optical band gap of the films can be roughly calculated from the wavelength corresponding to optical absorption edge using the relation:

$$E_g = \frac{1.242}{\lambda(\text{microns})} \tag{3.14}$$

For a more accurate measurement of band gap.it is assumed that there is a direct transition between valance band and conduction band. when light photon of incident energy $h\nu$ falls on the material. In this case the absorption co-efficient α is related to band gap E_g as [5]

$$(h\nu\alpha)^2 = \text{constant}.(h\nu - E_g) \quad (3.15)$$

The absorption co-efficient α of the thin films for different wave lengths were calculated using the relation:

$$\alpha = \frac{1}{2}log[T/100] \quad (3.16)$$

Figure 3.10 shows the optical transmission and absorption spectra of $SrTiO_3$ thin film deposited on fused silica substrate and annealed at 700^oC . The films were highly transparent and having interference colours on them. The refractive index and the thickness of the the films were calculated from the envelope curve of T_{max} and T_{min} generated from the peaks and valleys of the interference maxima and minima. The refractive index and thickness calculated by the above method were 1.94 and 0.6μm respectively. The thickness calculated in this way was with in the experimental error to that obtained using a thickness profiler. The optical band gap Eg was determined by extrapolating the linear portion of the plot relating $(h\nu\alpha)^2$ and $h\nu$ to $(h\nu\alpha)^2$ equal to zero. Figure 3.11 shows the plot between $(h\nu\alpha)^2$ and $h\nu$ for $SrTiO_3$ thin film deposited on fused silica. The value optical band gap determined from the plot according to the above method was 3.36 eV.This value is comparable to that of single crystal value of 3.37-3.41 eV [6].

3.7 Fourier Transform Infrared (FTIR) Spectroscopy

The FTIR spectroscopy is a powerful modern techniques for evaluation of materials in which spectrum is first produced by an interferrogram, which is processed and computed in real time through a dedicated computer to provide high resolution information. Fourier transform infrared spectrophotometer, Model: Nicolet 510 P was used in the FTIR studies to evaluate the structural and chemical changes in $BaTiO_3$ and $SrTiO_3$ precursor films with heat treatment. It provides information about the nature of the bonding in the examined species. FTIR studies on sol-gel

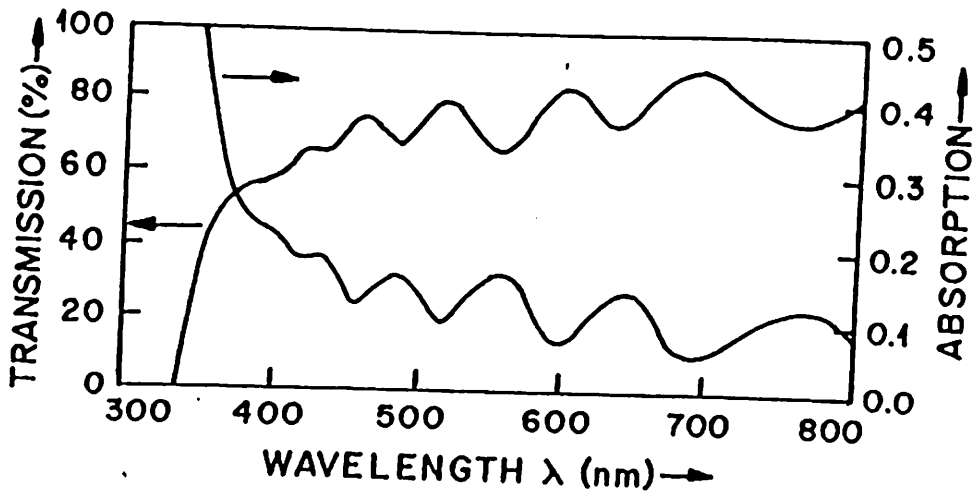

Figure 3.10: Optical transmission and absorption spectra of $SrTiO_3$ thin film on fused silica substrate made by sol-gel process.

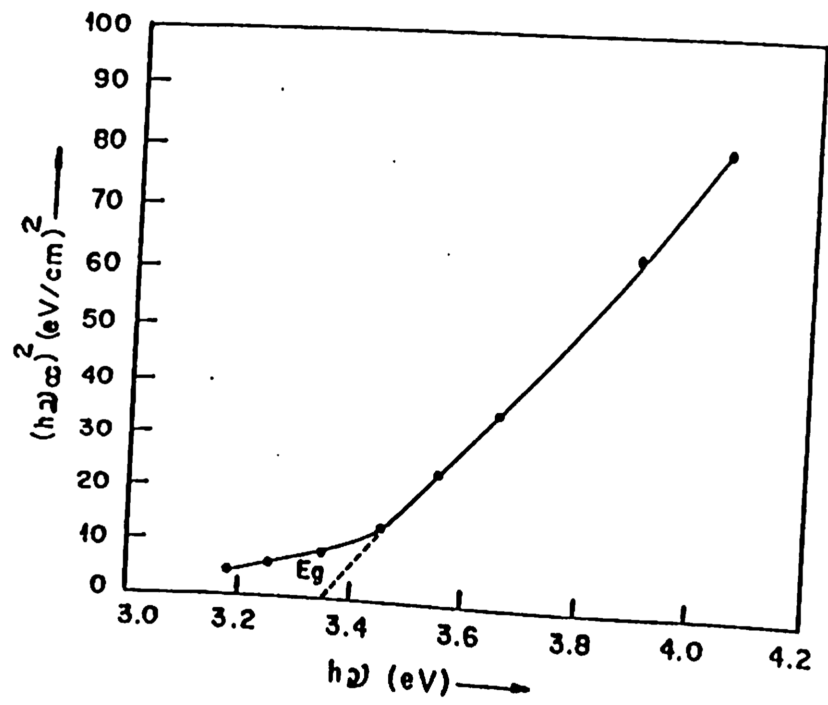

Figure 3.11: Determination of band gap from the optical data.

precursor films provides information about the nature of complexation of the starting materials, hydrolysis during deposition, condensation reactions occurring during heat treatment, pyrolysis of organics, polymerization of the condensed products and the crystalline phase formation. FTIR technique has been used in the present investigation qualitatively to understand the different reaction mechanisms taking place during the final film formation from corresponding precursor solutions with heat treatment.

Atmospheric moisture and carbon dioxide can cause problem in infrared spectra. Water absorbs around 4000 to 3500cm^{-1} and 2000 to 1300cm^{-1} , while carbon dioxide absorbs at 2350 and 688cm^{-1} . These absorbance often mask weak features that are of interest for a particular investigation. Purging with dry air or nitrogen and annealing treatments were performed prior to loading the films for FTIR spectra investigation. FTIR spectroscopic studies were carried out to investigate the nature of chemical bonding of the precursor solution and the change in chemical structure during heat treatment. The results of the FTIR studies were discussed in chapter 4 in detail.

3.8 Electrical and Dielectric Measurements

Electrical measurements were done on samples having MIM and MIS structures, using HP 4192 A Impedance Analyzer in the range of 5 Hz to 13 MHz. The a.c. signal has an amplitude of 5 mV to 1.1 V. The samples were kept inside a measurement cell, having a provision for evacuation as well as circulation of dry oxygen or nitrogen. Pressure contacts were made on the electrodes and are connected to the impedance analyzer.

3.8.1 Frequency dependence of dielectric properties

It is very important to know that how a dielectric behaves when an alternating electric field is applied on them. This can give an insight into the different dielectric relaxation phenomena occurring in the material. Normally a parallel plate capacitor filled with a dielectric material can be investigated for their behaviour in alternating fields by introducing a complex relative permittivity $\epsilon^* = \epsilon' + i\epsilon''$, where ϵ' and ϵ'' are the real and imaginary parts of the complex relative permittivity. The current

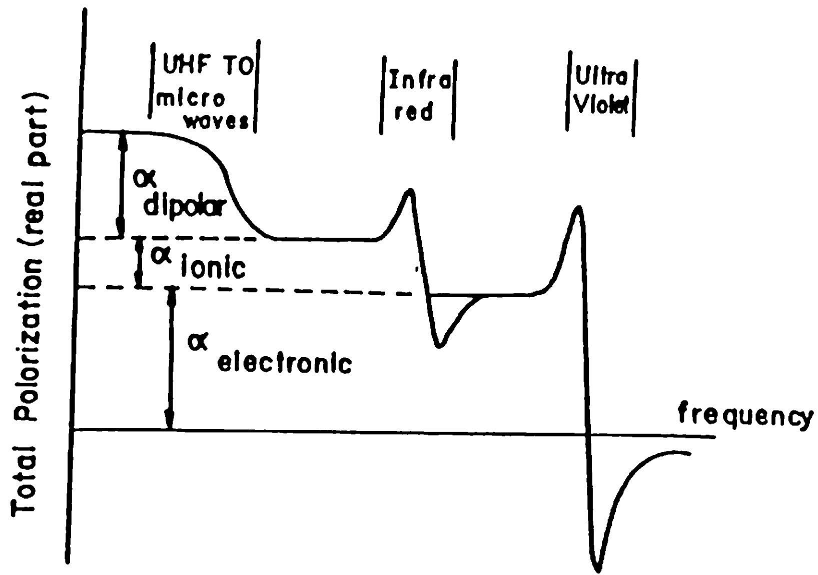

Figure 3.12: A typical frequency dependence of total polarization of a dielectric material.

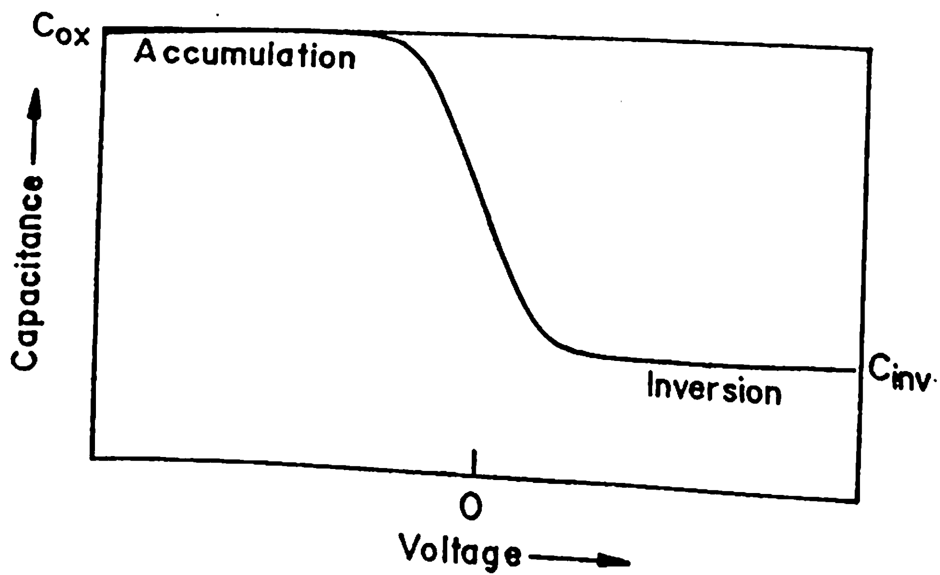

Figure 3.13: Typical C-V characteristics of an MIS capacitor.

through such a capacitor is made up of two components, one capacitive and lossless and the other a lossy component in phase with the applied field.

When a dielectric is placed in an electric field, different types of polarization occurs. They are electronic polarization, ionic polarization, dipolar polarization and space charge polarization. These electrical entities generally, have an inertia and hence the polarization do not occur instantaneously with the application of electric field. Due to this reason, the polarization phenomena is always accompanied by energy dissipation. Ionic and electronic polarization occurs at very high frequencies, which are above the frequency range of ac signal used in this study. From the point of view of MIM and MIS device fabrications, space charge polarization, dipolar polarization and electrode barrier polarization are important. The figure 3.12 shows the frequency dependence of polarization for a dielectric material.

3.8.2 Temperature dependence of dielectric properties

Ferroelectric materials are characterized by the presence of spontaneous polarization and a transition temperature above which the spontaneous polarization vanishes. Therefore, it is important to study the behaviour of a ferroelectric material at different temperatures with the application of an electric field. This is done by slowly heating the samples from room temperature to a temperature above the transition temperature and measuring their capacitance and loss factor for a range of frequencies at different steady temperatures.

3.8.3 Frequency dependent C-V characteristics

C-V measurements of the samples were done for an applied bias in the range of +20 to −20 volts, using HP4192A Impedance Analyzer. The measurements were done for different frequencies of ac signal super imposed on the d.c. bias.

In C-V measurements, the direction of voltage sweep and sweep rate and the gate material selection are important. An ideal C-V plot for a p-type MOS devices is shown in figure 3.13. When a negative bias is applied to the gate, positive charges are attracted from the semiconductor and they accumulate at the semiconductor oxide

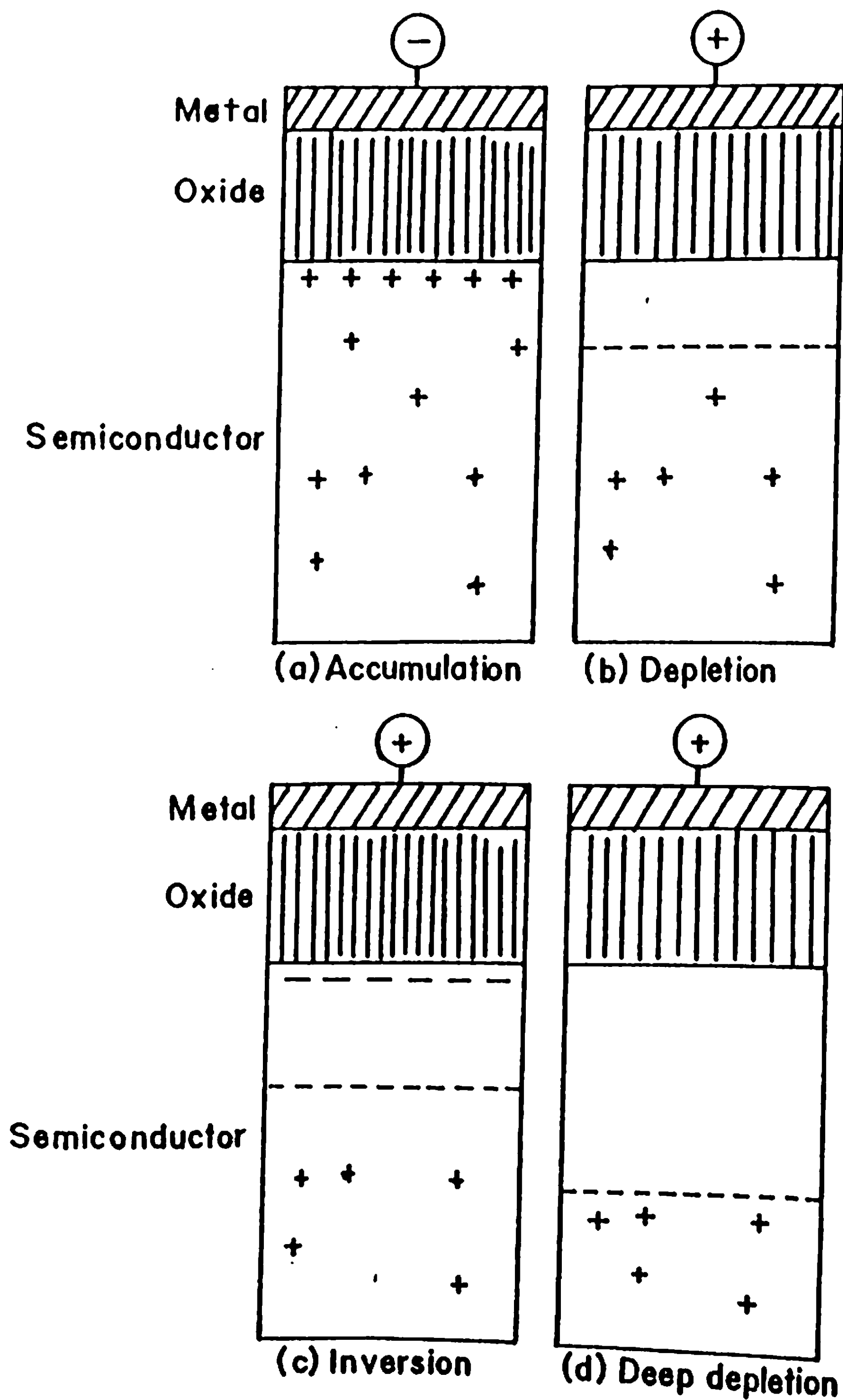

Figure 3.14: Representation of accumulation, depletion, inversion and deep depletion during the voltage sweep in the C-V characteristics of an MIS capacitor.

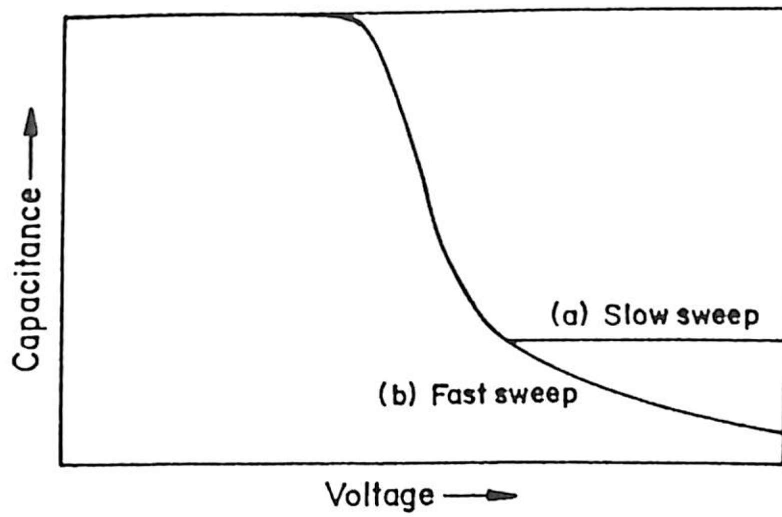

Figure 3.15: Representation of sweep rate dependence of C-V characteristics.

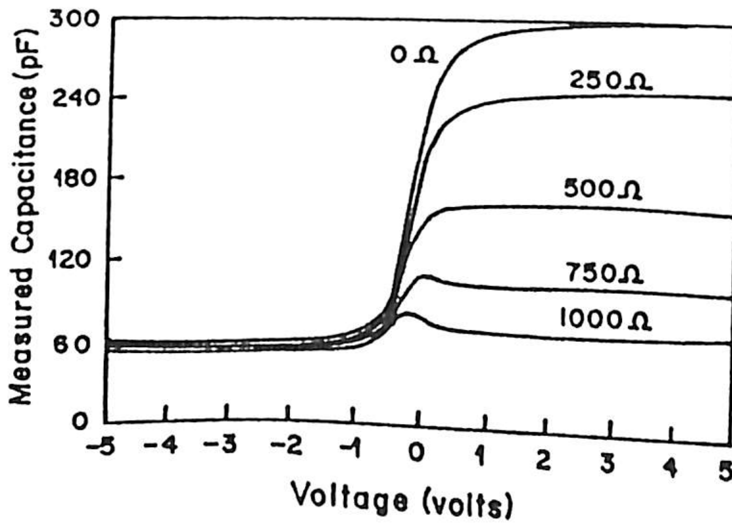

Figure 3.16: Effect of series resistance in the C-V characteristics of an MIS capacitor.

interface. Under these conditions, the high frequency small signal capacitance is simply the parallel plate capacitance and is equal to $\epsilon_o \epsilon_r A/d$.This is called accumulation. A reduction in negative gate bias will diminish the accumulated charges. As the bias changes from −ve to +ve, the charges are repelled from the interface and the region will be depleted of majority carriers. This is called depletion. As the positive bias on the gate again increases, the depletion region width increases and as a result the capacitance decreases. At this point when the depletion region is devoid of mobile charge carriers, the region will be in a non equilibrium state. Semiconductor then tries to re-establish the equilibrium by generating electron hole pairs, and the electron accumulates near the semiconductor oxide interface. This creates an inversion. The inversion region charges prevent further depletion and the capacitance remain constant. If sufficient time is not given for the generation of electron hole pair, inversion can not occur and depletion contineous to a state called deep depletion. These different stages are indicated in figure 3.14 [7].

If the C-V plot is swept from accumulation to inversion, then the upper bond for the sweep rate must be found to ensure that inversion occurs. The effect of sweep rate on the C-V characteresticis is shown in figure 3.15. A slow sweep rate may not be practical in production environment, where suitable selection of sweep rate may be necessary. When a very slow sweep rate is selected time is wasted in plotting wafers with fast generation time. To overcome these difficulties, the C-V plot was swept from inversion to accumulation after a stable inversion condition is established. Since the plot begin with an MIS device already in equilibrium, there are no sweep rate effects and plot speed limitations. Another method of achieving this is done by sweeping the C-V characteristic cyclically from accumulation to inversion and back to accumulation. This cyclic sweep can be used to study about the hysteresis behaviour due to charge injection in to the film. The substrate resistance and back contact resistance generally affects the measured value of capacitance of an MIS device. The relationship between the measured capacitance C_m and the actual capacitance C_i due to insulator layer is given as:

$$C_m = \frac{C_i}{1 + \omega^2 {R_s}^2 {C_i}^2} \tag{3.17}$$

where R_s is the series resistance with the capacitor. When $\omega R_s C_i$ is equal to 1, the

measured capacitance will be only half the actual value. A large series resistance will lead to immeasurably small capacitance. The effect of series resistance will be large at higher frequencies as well. The effect of series resistance in the C-V plot of an MIS structure is shown in figure 3.16.

3.8.4 I-V and I-T measurements

The leakage current behaviour of MIM and MIS structures are important for using them in devices like DRAM's and other non volatile memory devices. A Keithley 220 current source was used to provide a programmable voltage at the guard output to serve as the voltage bias source. The current was measured using a Keithley picoammeter model# 485. These outputs were then connected to the IEEE-488 bus for data acquisition. The programming for data acquisition was performed in basic. The program includes facilities for direct viewing graphical presentation and storage of data for subsequent analysis. The ramp rates were varied as per requirement by programming the bias source. The mechanism of current conduction in these devices were studied from the I-V characteristics at various temperatures. The I-T data are collected by monitoring the variation of current at fixed voltage bias as a function of temperature.

3.9 Ferroelectric Measurements

Polarization reversal mechanism in ferroelectric material are controlled by the nucleation, growth, merging and shrinkage of ferroelectric domains. These phenomena are dependent on nature of Barkhausen jumps (the polarization switching jumps), the internal electric field, the dielectric relaxation times and the ferroelectric electrode interface states.

3.9.1 Polarization reversal mechanism

The total dielectric displacement D, the extent to which the external electric field has been altered by the presence of the dielectric is expressed by either the external applied field E_A [8] or the electric field in the dielectric (local electric field) E_L [9].

Thus D is represented as:

$$D = \epsilon_o E_A + P_t \quad (3.18)$$

P_t is the total polarization, which is the sum of polarization due to linear contributions to displacement (P_l) and switching of dipoles in ferroelectric films (P_d) ie.,

$$D = \epsilon_o E_A + P_l + P_d = \epsilon_o E_A + \epsilon_o \chi E_A + P_d = \epsilon_o \epsilon_r E_A + P_d \quad (3.19)$$

where, χ is the dielectric susceptibility of the ferroelectric and ϵ_r the relative permittivity of the dielectric. The polarization P_l generates an internal field E_i in the ferroelectric, which opposes the applied field. The difference between these two is called the local field and represented as:

$$E_L = E_A - E_i = E_A - \frac{\eta}{\epsilon_o \epsilon_r}(P_l + P_d) \quad (3.20)$$

The polarization P_d controls the hysteresis properties. where, η is depolarization factor.

The different stages of spontaneous polarization can be classified in to one or more domain phenomena as shown in figure 17 [10]. It starts with domain nucleation at the initial stage of polarization for virgin ferroelectric. When the size of the domain nucleus becomes larger than the critical size, the domain begins to grow. After growth of each domain, they meet each other and begin to merge. As the applied field increases, the merged domains grow. However, the internal field will also increase with applied field and because of this, complete polarization may not be achieved. When the applied field is decreased, the polarized domains may return to the original state. As the external field begins to increase in the opposite direction, the opposite domains will nucleate or grow with a continuous shrinkage of previously existing domains.

3.9.2 P-E hysteresis

The P-E hysteresis loop displayed on an oscilloscope is used as the basic evidence for the presence of ferroelectric state in a material. This is done by with the aid of Sawyer and Tower [11] circuit shown in figure 3.18. A.C. signal of frequency 60 Hz was applied in the circuit. The samples used were, $BaTiO_3$ thin films grown on

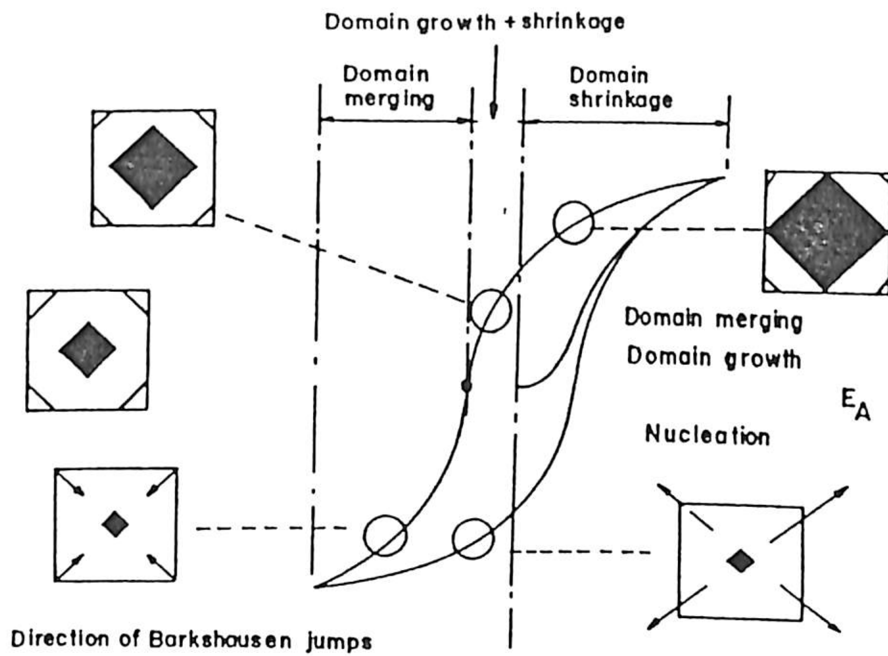

Figure 3.17: Different stages in the P-E hysteresis cycle of a ferroelectric material.

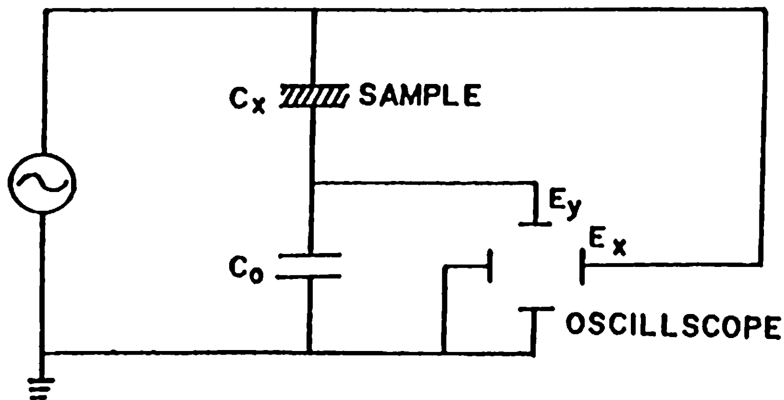

Figure 3.18: Typical Sawyer-Tower circuit for measuring P-E hysteresis loop.

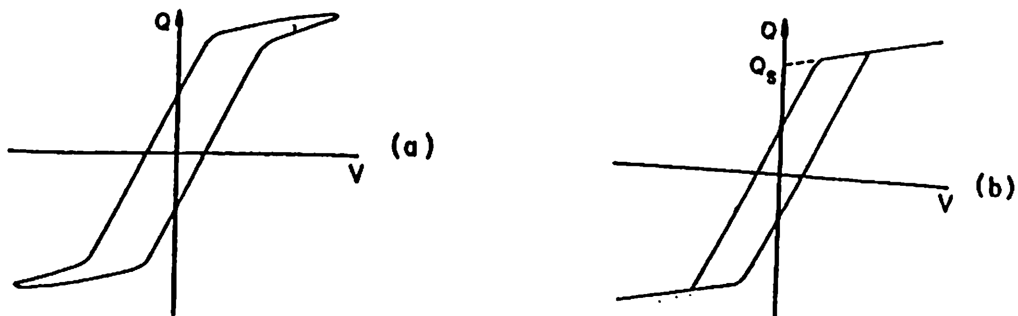

Figure 3.19: Typical hysteresis loop due to (a) a conducting sample (b) an insulating sample.

platinized silicon wafers with top gold electrode, to form a parallel plate capacitor or MIM structure having a capacitance C_r. A capacitor of large capacitance C_o provided as a reference capacitor. Then the oscilloscope deflection are expressed as:

$$V_x = V + E_y, \quad V_y = C_o Q \tag{3.21}$$

where V and Q are the voltage and charge, respectively on the sample.

A simple Sawyer-Tower circuit is not adequate for displaying the hysteresis loop due to lossy samples. Figure 3.19(a) and (b) shows the hysteresis loop due to non conducting and conducting sample respectively. Genarally, samples with higher conductivity produce hysteresis loops with rounded ends, which in turn distorts the actual hysteresis due to spontaneous polarization. To overcome this, a modified Sawyer-Tower circiut has been used [12]. A compensating arm containing a parallel combination of adjustable resistance R_c and capacitance C_c in the order of sample resistance and capacitance is constructed. The input is applied simultaneously to the sample and the compensation arm and then to the inputs of a differential amplifier. the vale of R_c and C_c are then adjusted to nullify the effect of sample resistance and capacitance. The block diagram of the modified hysteresis loop is shown in figure 3.20. The measurements were done in a cell, protected from atmospheric humidity by flowing dry air through the cell. However when the samples were exposed to atmosphere, the P-E loop displayed were lossy nature due to the increase in conductivity due to the absorption of moisture.

The remanent polarization in calculated from the hysteresis loop using the relation

$$P_r = \frac{C_o V_y}{A} \tag{3.22}$$

where A is the area of the sample and V_y the voltage along Y-axis corresponding to remanent polarization.

3.9.3 C-V butterfly loop

Ferroelectricity was again confirmed by performing C-V measurements on an MIM structure. Due to the non-linear dielectric behaviour of ferroelectric materials, the

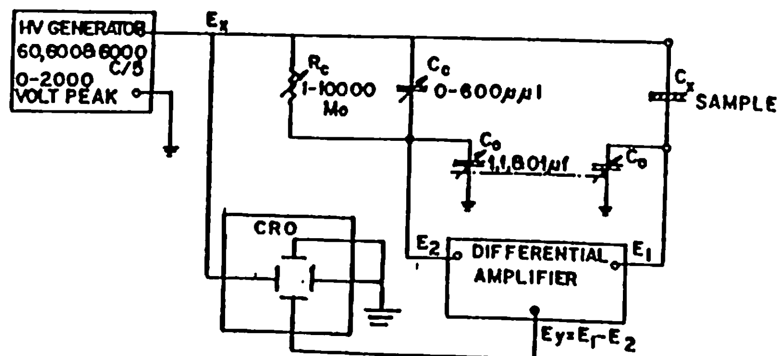

Figure 3.20: Block diagram of a modified Sawyer-Tower cicuit with compensation for sample conductivity and capacitance.

C-V characteristic on an MIM structure shows a typical butterfly loop. These measurements were again done with HP 4192 A Impedance Analyzer, in the range of −20 to +20 volts and at frequencies ranging from 1 kHz to 1MHz.

3.10 Preferred Orientation in $BaTiO_3$ Thin Films Grown on Single Crystal $SrTiO_3$ (100) Substrates.

Barium titanate and strontium titanate are belonging to the family of perovskite crystals with very good lattice matching (lattice mismatch less than 5 percent). This makes it feasible to grow thin films of $BaTiO_3$ on single crystal $SrTiO_3$ substrates. The desirable nonlinear optical properties [13] of the $BaTiO_3$ makes it attractive for a variety of electro-optic and optical storage device applications. The unique properties of this material have stimulated research in the development of high quality epitaxial $BaTiO_3$ thin films on various matching substrates, mostly by physical vapour deposition techniques [14,15]. But there is hardly any literature available on the fabrication of epitaxial thin films of $BaTiO_3$ on any kind of substrate by wet chemical process like sol-gel and metal organic decomposition (MOD). Figure 3.21 represent the X-ray diffraction pattern of $BaTiO_3$ thin films deposited $SrTiO_3$ substrate at 600 °C and 900 °C as indicated in the film. For comparison the X-ray diffraction pattern of a polycrystalline $BaTiO_3$ thin film made on fused silica substrate at 600 °C is also given. The film made on $SrTiO_3$ at 600 °C shows enhanced peaks corresponding to (100) and (200) reflection from the $BaTiO_3$ thin films. A reduction in the strongest polycrystalline peak, (110), is also observed in the spectra. As the films were annealed 900 °C , all the cross peaks corresponding to the powder diffraction pattern has been reduced in intensity to an insignificant level. The spectrum of $BaTiO_3$ thin film at 900 °C shows the reflections mainly from (100) and (200) planes of $BaTiO_3$ thin films. These results suggest that epitaxial thin films of $BaTiO_3$ thin films can be grown on $SrTiO_3$ substrates by sol-gel process. Figure 3.22 shows the scanning electron micrograph of $BaTiO_3$ thin film made on single crystal $SrTiO_3$ substrate and annealed at 600 °C . The surface of the film reveals good uniformity and crystallinity.

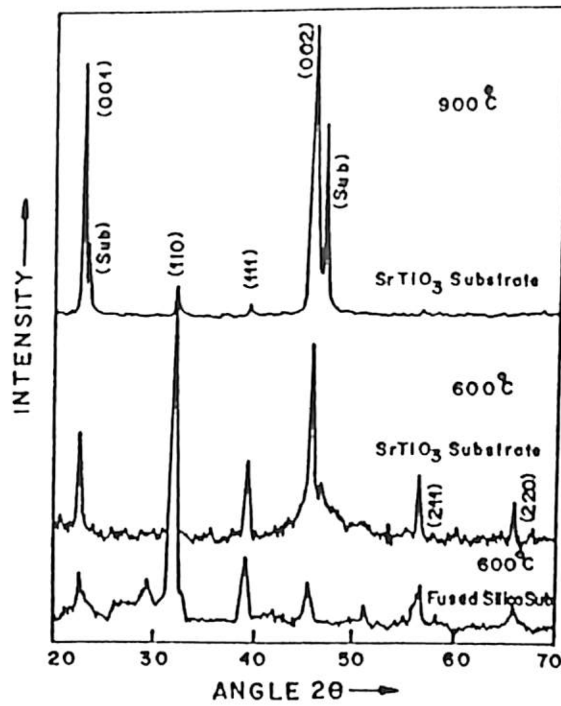

Figure 3.21: XRD spectra showing preferred orientation in sol-gel grown $BaTiO_3$ thin film on single crystal $SrTiO_3$ (100).

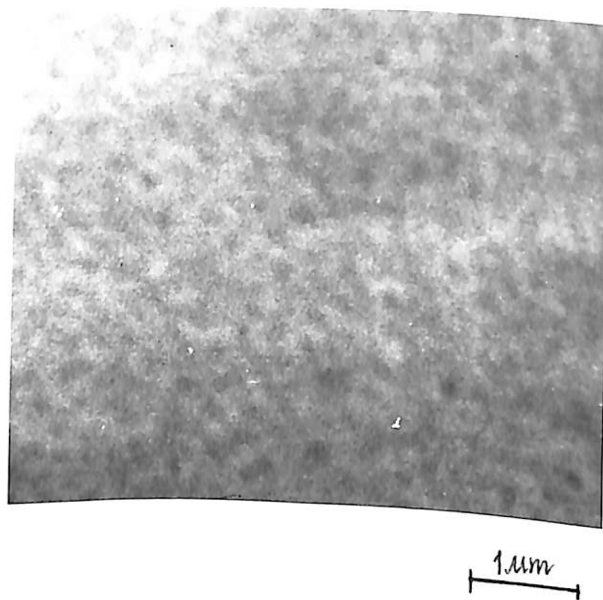

Figure 3.22: Scanning electron micrograph of $BaTiO_3$ thin film grown on single crystal $SrTiO_3$ (100).

References

1. Adir Bar-Lev. *Semiconductors and Electronic Devices; 2nd Edition.* (Prentice Hall of India. New Delhi. 1987) p. 117.

2. J. F. Hall. and W. F. C. Ferguson. J. Opt. Soc. Am. 45. 714 (1955).

3. S. P. Lyashenko. and V. K. Miloslavskii. Opt. Spectrosc. 16. 80 (1964).

4. J. C. Manifacier, J. Gasiot, and J. P. Fillard, J. Phys. E 9, 1002 (1976).

5. J. Callaway, *Quantum Theory of the Solid State* (Academic, New York, 1974), p.525.

6. G. A. Barbosa. R.S. Katiyar, and S.P.S. Porto, J.Opt. Soc. Am. 68,610 (1978)

7. B. J. Gordon, Solid State Tech. Jan. 1993, p.57.

8. A. J. Moulson, and J. M. Herbert, 1990, *Electroceramics, Materials-Properties-Applications* (London: Chapman & Hall),p.54.

9. C. Kittel, 1976, *Introduction to Solid State Physics*, Fifth edition(New York: Wiley), P.404.

10. I. K. Yoo and S. B. Desu, Philo. Mag. B, 69, 461 (1994).

11. C. B. Sawyer and C. H. Tower, Phys. Rev. 35, 269 (1930).

12. H. Diamant, K. Drenck and R. Pepinsky, Rev. Sci. Inst. 28, 30 (1957).

13. B. A. Wechsler, M. B. Klein, and D. Rytz, SPIE Proc.. Laser Nonlinear Opt. Mater. 681, 91 (1986).

14. K. Fujimoto, Y. Kobayashi, and K. Kuboto, Thin Solid Films 169, 249 (1989).

15. G.. M. Davis and M. C. Gower, Appl. Phys. Lett. 55, 112 (1989)

Chapter 4

Structural and Microstructural Evolution in $BaTiO_3$ and $SrTiO_3$ Precursor Thin Films

Bulk ceramic materials and thin films exhibit large variations in their physical, optical and electronic properties depending on their structure, microstructure and stoichiometry. In sol-gel processed thin films these variations occur mainly due to the use of impure chemicals, irreproducible processing conditions and improper starting materials. In fact the strong dependence of processing parameters on properties of the sol-gel derived materials can be used advantageously to tailor the material properties of films to suit various technological requirements. Various physical properties like changes in band gap, refractive index and thickness of the film during processing can be correlated with structural and microstructural changes as well as densification of the film [1,2]. In this regard it will be interesting to examine the films prepared by sol-gel process at various film preparation stages and to understand the chemical as well as solid state reactions taking place at various temperatures. The structural and microstructural evolution in $BaTiO_3$ and $SrTiO_3$ thin films during film formation is discussed here.

4.1 Studies on Sol-gel derived Barium Titanate Thin Film

Barium titanate thin films and ceramics were synthesized by sol-gel process by various workers using different barium sources like barium acetate [3-5], barium 2-ethyl hexanoate [6,7], barium alkoxides and barium metal dissolved in alcohols [8-11], barium acetyl acetonate [11], barium hydroxide [12-16] (aqueous solution as well as dissolved in alcohols) etc. The dielectric, ferroelectric and structural properties of $BaTiO_3$ thin films prepared from these precursors show large variations. It will therefore be interesting to compare the film formation properties of different $BaTiO_3$ sol-gel systems. Different experimental techniques like infrared, uv-visible and x-ray diffraction spectroscopic studies were carried out for this purpose. Sol-gel derived $BaTiO_3$ thin films prepared from two different precursor systems, one using barium 2-ethyl hexanoate and other using barium hydroxide dissolved in 2-methoxy ethanol as barium source were used in the study. The titanium source in both cases were titanium isopropoxide ($Ti(OC_3H_7)_4$) (Aldrich). The reaction products were examined at various curing temperatures using infrared absorption spectroscopy to see the evolution of barium titanate from their respective barium and titanium compounds. The optical properties of the films were studied using optical transmission spectroscopy and structural properties using x-ray diffraction spectroscopy and these results were correlated with physical and microstructural properties of the film.

4.1.1 FTIR Studies

Figures 4.1(a) to (f) shows FTIR spectrum of $BaTiO_3$ precursor (EH precursor) spin coated on KBr single crystal substrates. Curve (a) shows the spectrum of titanium isopropoxide chelated using 1 mole of acetyl acetone. The bands at 1550 and 1590cm^{-1} are due to acetyl acetone (acac) bonded to titanium. Curve (f) shows the spectrum of barium 2-ethyl hexanoate thin film deposited at 30°C after dissolving it in methanol. The bands at 1400-1600cm^{-1} region are due to symmetric and asymmetric stretching vibrations of carboxylate group. Curve (b) shows the spectrum of $BaTiO_3$ precursor (EH precursor) cured at 30°C . It shows that most of the bands

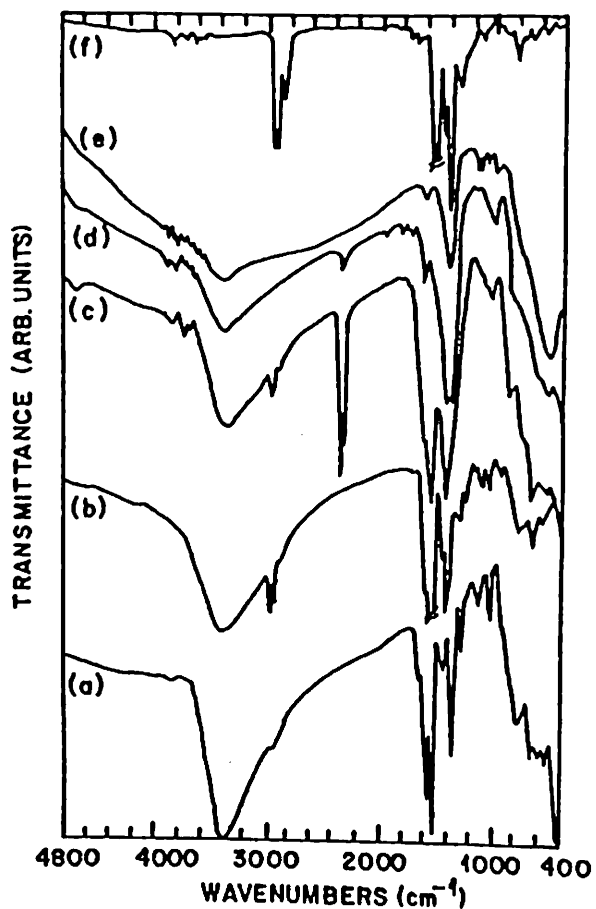

Figure 4.1: FTIR spectrum of $BaTiO_3$ precursor thin film (EH precursor) annealed at different temperatures.

due to titanium-acac complex are overlapped by carboxylate bands. The spectrum do not show evidence for any cross reaction between barium 2-ethyl hexanoate and titanium isopropoxide in solution. The curves (c), (d) and (e) show absorption spectra of EH precursor films cured at 250°C , 400°C and 550°C respectively. The broad band around $3400cm^{-1}$ which decreases in intensity with increase in annealing temperature is due to OH stretching vibrations due to hydroxyls present in the system. The bands between $2800\text{-}3000cm^{-1}$ are due to C-H stretching vibrations of the organic molecules. The bands due to C-H stretching, acac-titanium isopropoxide complex and those due to carboxylates disappear in the spectra taken after annealing the films above 400°C . This is due to the complete removal of organics above an annealing temperature of 400°C . The new bands appearing at $2335\text{-}2350cm^{-1}$ at an annealing temperature of 250°C and vanishing above 400°C is due to CO_2 adsorbed on the film, which has been evolved from the film due to the oxidation of organic molecules. The new band appearing at $1400cm^{-1}$ after annealing the film at 400°C may be due to the formation of Ba-O-Ti bond. It seems that titanium dioxide which is present in the film from the hydrolysis and polycondensation of titanium isopropoxide reacts with BaO released from the decomposition of barium 2-ethyl hexanoate at annealing temperatures between 300-400C forms Ba-O- Ti bond which is responsible for the appearance of the above absorption peak. FTIR spectrum of the film annealed at 600°C shows reduction in the $1420cm^{-1}$ band as well as the appearance of a new band at $530cm^{-1}$ which is due to the formation of $BaTiO_3$ crystallites [17,18].

Figure 4.2 shows the FTIR spectrum of films coated on KBr single crystal substrates in the range of $4800\text{-}400cm^{-1}$ using ME precursor. Curves (a)-(f) shows absorption spectra of $BaTiO_3$ precursor films annealed at 30, 150, 250, 350, 550 and 650°C respectively. The curve (g) shows the FTIR spectrum of the film made by the coating the solution containing barium hydroxide dissolved in 2-methoxy ethanol. The curve (g) contains strong absorption bands at $3400cm^{-1}$ (OH stretching), 2800-$3000cm^{-1}$ (C-H stretching), 1640, 1400, 1310 and $1080cm^{-1}$. The absorption bands of barium hydroxide dissolved in alcohols are difficult to assign because of the complex nature of the solution chemistry reported for this system [13]. However the mixture of barium hydroxide dissolved in 2-methoxy ethanol and titanium isopropoxide do not

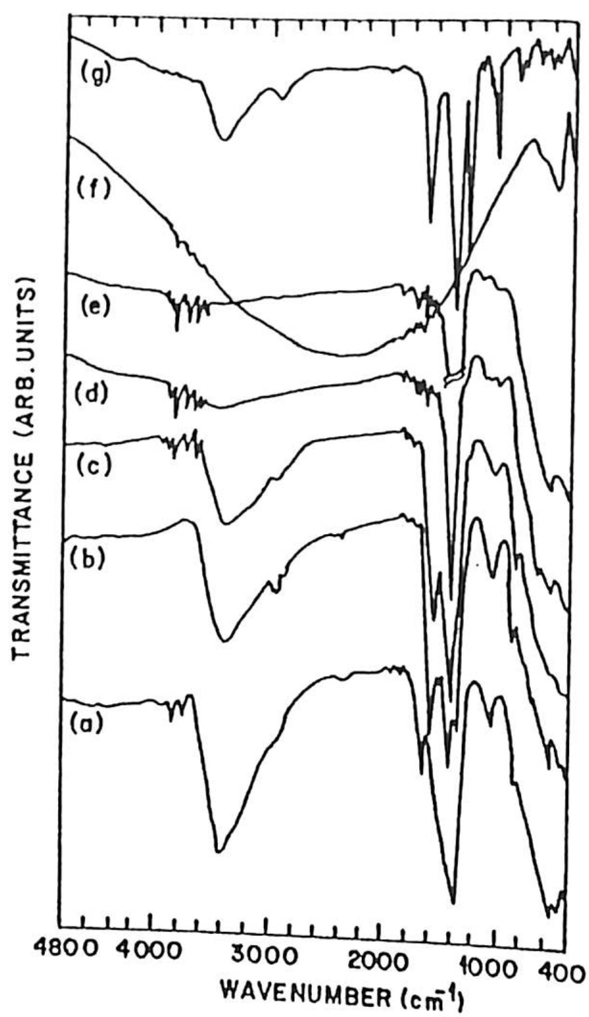

Figure 4.2: FTIR spectrum of $BaTiO_3$ thin film (ME precursor) annealed at different temperatures.

contain the strong absorption band of the former at 1310cm^{-1}, which denotes the reaction between the two precursors to form a complex, probably a mixed alkoxide. The band at 1310cm^{-1} may be due to metal-alkoxy bond (Ba-OR) of barium 2-methoxy ethoxide present in the solution. Further, the absorption band of the $BaTiO_3$ film deposited at 30°C (curve(a)) shows a broad band centered at 1390cm^{-1}. This band upon curing the film at 150°C resolved in to three bands with the strongest band at 1420cm^{-1}. This band remains stronger even after curing the film at 550°C and may be due to Ba-O-Ti bond. A band at the same position is seen for the $BaTiO_3$ film prepared from EH precursor and annealed at 400°C confirms this fact.

Other notable features of the FTIR spectrum of the ME precursor films (curves (a) to(f)) are the progressively decreasing height of OH stretching band with increase in annealing temperature and the decreasing intensity and the absence of the C-H stretching band with increase in annealing temperature. This is due to the removal of hydroxyls and organics present in the precursors. Finally the film annealed at 650°C shows a broad absorption in the region 4800cm^{-1} to 800cm^{-1} and the presence of an absorption peak at 530cm^{-1}. The 530cm^{-1} peak can be assigned to crystalline $BaTiO_3$.

4.1.2 X-ray diffraction studies

Figure 4.3(a)-(c) show the XRD spectra of barium titanate thin films coated on silicon (100) substrate from EH precursor and annealed at 450, 600 and 800°C respectively. The spectrum of the sample annealed at 450°C shows no clear peaks belonging to $BaTiO_3$ or any of its components and is showing a broad peak with d = 3.10Åbelonging to some unknown phase. The spectrum of the sample annealed at 600°C shows clear $BaTiO_3$ peaks only and does not show any additional peaks indicating that $BaTiO_3$ has crystallized in single phase. The spectrum at 800°C shows enhancement in peak heights showing increased crystallinity. The peaks having higher (hkl) values show broadening as well as splitting (eg.(211,112) and (220, 202)) suggesting tetragonal structure having lattice parameters, a = b = 3.995Åand c = 4.05Å. Further, the observation of ferroelectricity in these films [6] confirms the tetragonal structure.

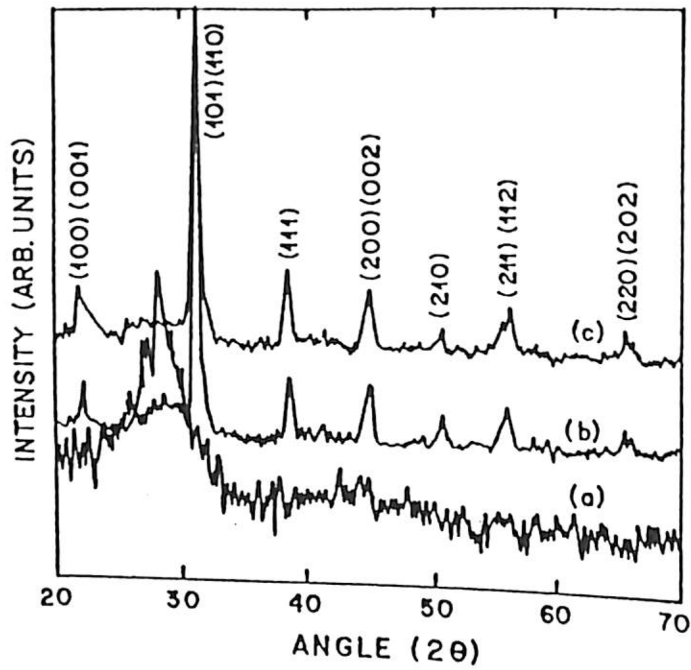

Figure 4.3: XRD spectra of $BaTiO_3$ precursor (EH) thin films coated on single crystal silicon (100) and annealed at (a) 450°C , (b) 600 °C and (c) 800°C .

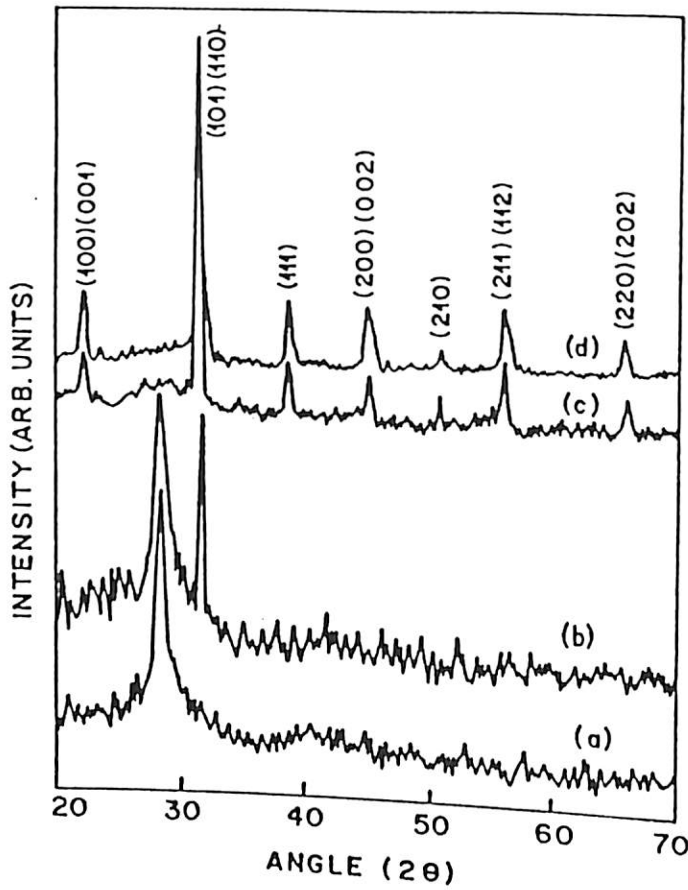

Figure 4.4: XRD spectra of $BaTiO_3$ precursor (ME) thin films coated on single crystal silicon (100) and annealed at (a) 350°C , (b) 450 °C , (c) 600°C and (d) 800°C .

Figure 4.4(a)-(d) shows the XRD spectra of $BaTiO_3$ films deposited from ME precursor and annealed at temperatures 350, 450, 600 and 800°C respectively. The film annealed at 350°C shows only one peak with value of d = 3.10A, which may be due to some unknown phase. The spectrum of the film annealed at 450°C shows the same phase as above and another peak with value of d = 2.814. It is doubtful whether this peak is due to $BaTiO_3$ (110). Other evidences like optical absorption and FTIR suggest that the film has not crystallized in to $BaTiO_3$ phase at 450°C . The film annealed at 600°C and 800°C show only $BaTiO_3$ phase. Peaks belonging to higher (hkl) values were also developed in the spectra. The peaks belonging to (hkl) values (200) and (002) as well as (112) and (211) do not show any splitting or broadening suggesting that the films were crystallized in cubic phase. The lattice constant calculated from the spectra was 4.005Å. The absence of ferroelectricity in our films made from ME precursor also confirms this fact. Similar results were obtained by Fray and Payne [9] for $BaTiO_3$ films made by sol-gel technique from barium and titanium methoxy ethoxide precursors also.

4.1.3 Optical Studies

The optical properties of barium titanate thin films made by sol-gel process using EH precursor and ME precursor in the range of 200-1100 nm were studied using optical transmission spectroscopy. The film thickness and refractive index were determined from the envelope of T_{max} and T_{min} generated from the peaks and valleys of the interference maxima and minima employing Manifacier et al. method of calculation of optical constants for weakly absorbing films [19].

Figure 4.5(a) and (b) show the variation of thickness for films grown from EH and ME precursors respectively with annealing temperature. Both films show continuous thickness reduction with annealing temperature up to 650°C . Films grown from EH precursor show large thickness reduction between 300°C to 450°C (35%) than those made from ME precursor(10%). Above 450°C the shrinkage is very slow and nearly linearly decreases with increase in annealing temperature up to 700°C . Above this temperature the film thickness increases with further increase in annealing temperature.

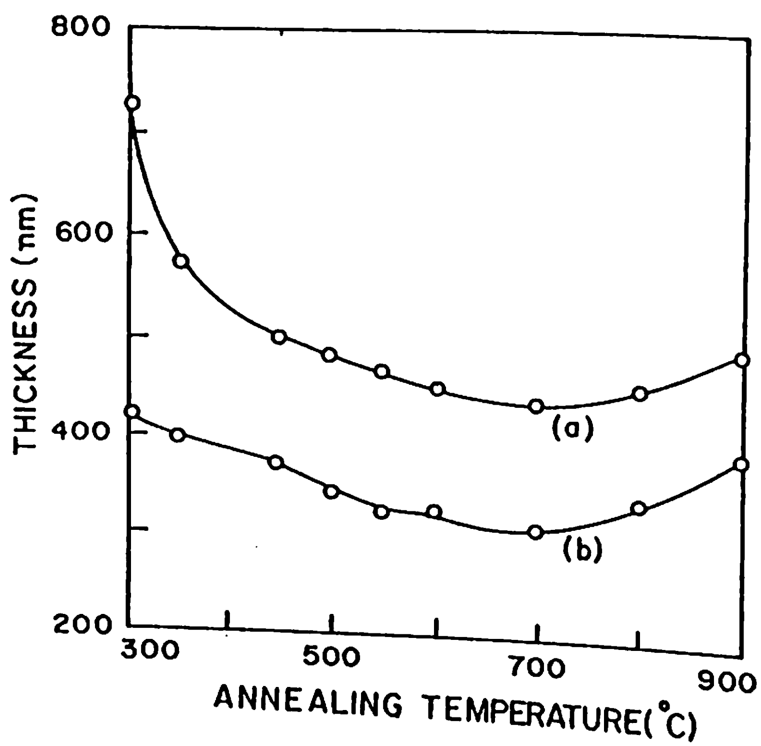

Figure 4.5: Variation of thickness of $BaTiO_3$ precursor thin films on fused silica substrate with annealing temperature (a) EH precursor and (b) ME precursor.

The shrinkage of thin films fabricated by sol-gel process can be due to different chemical and physical changes taking place during the film formation process. They are (a) surface tensional forces exerted by the solid-liquid interface during solvent evaporation, which occurs around room temperature, (b) removal of organics and subsequent collapse of the pore structure occurs during the pyrolysis of organics in the range of 200-400°C, (c) bond formation between metal atoms through oxygen atom due to the condensation of hydroxyls, which occurs at all temperatures below sintering temperature, (d) structural relaxation which is assisted by ionic movements at elevated temperatures, etc.

The films under study were cured at 300°C. Most of the solvent in the films would have already evaporated and therefore the shrinkage due to surface tensional forces are not expected to assist further shrinkage of the films. The presence of organics and its subsequent removal between 200°C to 400°C is evident from the successive reduction in the infrared absorption bands at 2800-3000cm^{-1} (figure 4.2). Even though the removal of organics in an all-alkoxide sol-gel system do not produce shrinkage[20] (it effects an increase in porosity) the large organic content of the organic salt-alkoxide precursor seem to produce porosity as well as shrinkage in the film. This is evident from the larger shrinkage in the EH precursor films compared to that of ME precursor films. The pore structure of the EH precursor films seems to collapse as the pyrolysis proceeds effecting in the shrinkage of the film.

The general continuous shrinkage experienced in films prepared by sol-gel process may be due to the condensation reaction,

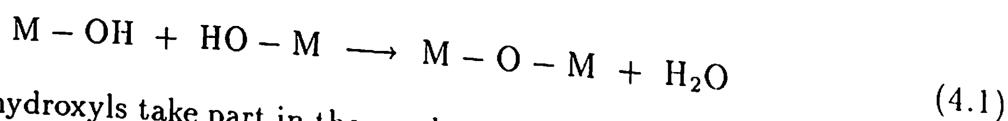

$$M-OH + HO-M \longrightarrow M-O-M + H_2O \qquad (4.1)$$

where the metal hydroxyls take part in the condensation reaction to produce metal to metal bond through oxygen. The progressive reduction of OH band centered around 3400cm^{-1} in the FTIR spectrum clearly supports this reaction. The shrinkage between 450-650°C may be a combined effect of condensation and structural relaxation. The structural relaxation which occurs due to diffusive motion of barium and titanium ions to produce barium titanate crystals remove excess free volume from the film effecting in compaction of the structure. These structural changes are seen in the FTIR spectrum by the appearance of a band at 530cm^{-1}, which is attributed to

the Ti-O stretching vibration of the $BaTiO_3$ crystal. The increase in thickness of the films annealed above 750°C is due to cracking of the film arising from the thermal mismatch of the film with the substrate, as seen from the electron micrographs. Figure 4.6(a)&(b) show the variation of refractive index (n) of the barium titanate thin films prepared from EH and ME precursors respectively with annealing temperature. The refractive index of EH film annealed at 300°C was 1.74, which decreased to 1.69 at 350°C and then increased with further increase in annealing temperature. Between 500°C and 600°C the refractive index showed a sharp increase and above 700°C it started decreasing.The refractive index of the films prepared from ME precursor continuously increased with increase in annealing temperature up to 650°C , and above which it started decreasing. The rate of increase in the refractive index in these films were maximum in the temperature range of 450-600°C .

The refractive index (n) of $BaTiO_3$ thin film is proportional to its electronic polarization per unit volume, which in turn is inversely proportional to interatomic distance [2]. Therefore a reduction in the interatomic distance resulting in the densification of the film will lead to an increase in refractive index. The densification in sol-gel films upon annealing may be controlled by condensation of hydroxyls as well as structural relaxation. The metal-oxygen-metal bond formed during condensation reaction helps in bringing up the atoms together. The reduction of surface energy attainable due to compaction of the film is the driving force for the structural relaxation. The sharp increase in the refractive index for films annealed between 450°C to 600°C may be due to a combined effect of condensation and structural relaxation. The decrease in refractive index for samples annealed above 700°C is due to the cracking of the films caused by thermal mismatch of the film with the substrate. The decrease in refractive index for the EH precursor films around 350°C may be due to the increase in porosity of the film due to the pyrolysis of organics present in the film[20]. Up on annealing at elevated temperatures, the pore structure collapse causing densification and shrinkage in the film. Similar annealing assisted shrinkage as well as densification were observed by Li et al for barium titanate thin films deposited using reactive partially ionized beam (RPIB)[2] technique. The optical absorption edge (E_g) of the films prepared by sol-gel technique using EH and ME precursors were

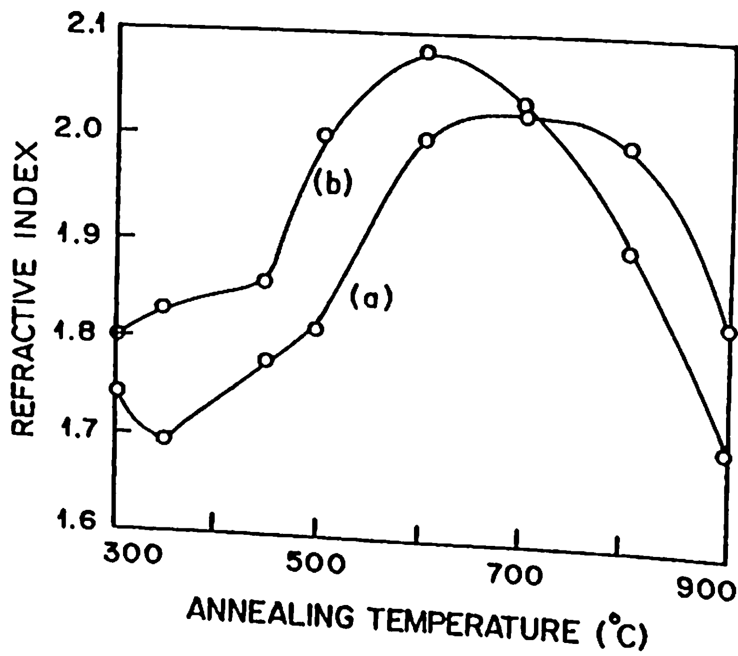

Figure 4.6: Variation of refractive index of $BaTiO_3$ thin films on fused silica substrate with annealing temperature (a) EH precursor and (b) ME precursor.

estimated from the optical transmission spectra. From the transmission spectra, the band gap was calculated by considering a direct transition between the valance band and conduction band [6]. Figure 4.7(a) and (b) shows the variation of the E_g of the films with annealing temperature. E_g of the film grown using both precursors show a value 3.95 eV below annealing temperatures of 500°C . The band gap of the film prepared from EH precursor decrease sharply from 3.95 eV to 3.5 eV when the annealing temperature was increased from 500°C to 550°C . The corresponding transmission spectra of the film is reproduced in figure 4.8, where the change in optical absorption edge is clearly visible. In ME films the change in optical absorption edge is observed between annealing temperature of 550-600°C only. Above 600°C the E_g for both films remain at 3.5 eV.The sudden decrease in the optical absorption edge denotes changes in the structure of the film. XRD studies and FTIR studies also suggest such a structural transformation of $BaTiO_3$ thin films around an annealing temperature of 600°C . Similar change in optical band gap were observed by Davis and Gower during the structural transformation of $BaTiO_3$ thin films deposited using excimer laser ablation [1].

4.1.4 Scanning electron microscopy

The abrupt changes of the properties of the film (thickness and refractive index) deposited on fused silica substrates and annealed around 600-700°C suggested for a closer look in to the film morphology using scanning electron microscopy. Figure 4.9(a) and (b) shows the electron micrograph of barium titanate films deposited using EH precursor annealed at 450°C and 800°C respectively and figure 4.9(c) and (d) shows that deposited using ME precursor and annealed at 450°C and 800°C respectively. While EH precursor films annealed at 450°C is featureless, that made from ME precursor show fine structure of about 30 to 50 nm diameter. The exact identity of these crystallites are not known. The electron micrography of the film deposited from both the precursors and annealed at 800°C show severely cracked surfaces presumably due to the thermal mismatch of the film with fused silica substrate. This accounts for the observed reduction in refractive index as well as the increase in thickness of the film above annealing temperature of 600°C (figure 4.5

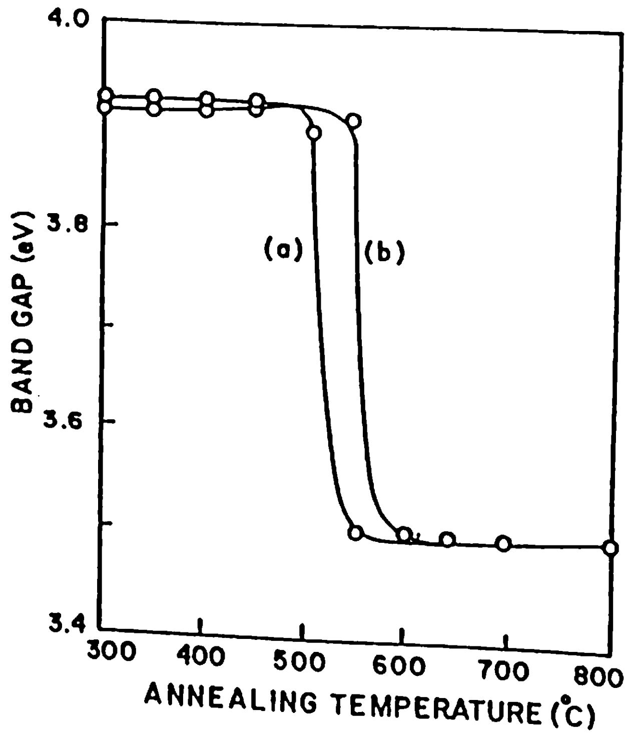

Figure 4.7: Variation of band gap E_g with annealing temperature of $BaTiO_3$ precursor thin films on fused silica substrate (a) EH precursor and (b) ME precursor.

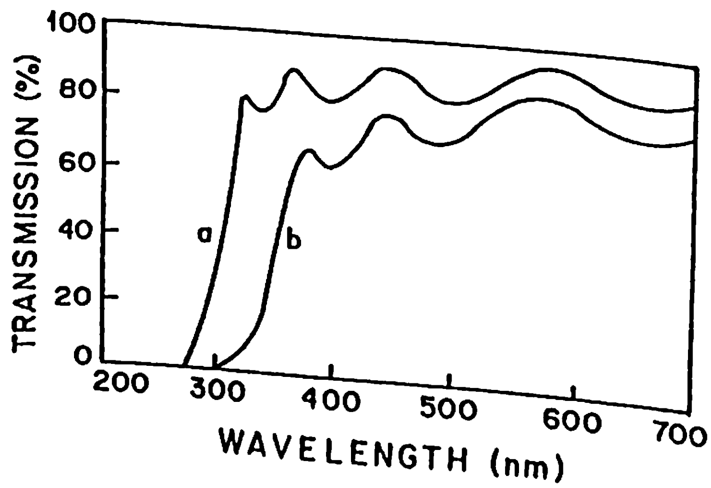

Figure 4.8: Optical transmission spectra of $BaTiO_3$ thin film on fused silica substrate annealed at (a) 400°C and (b) 600°C .

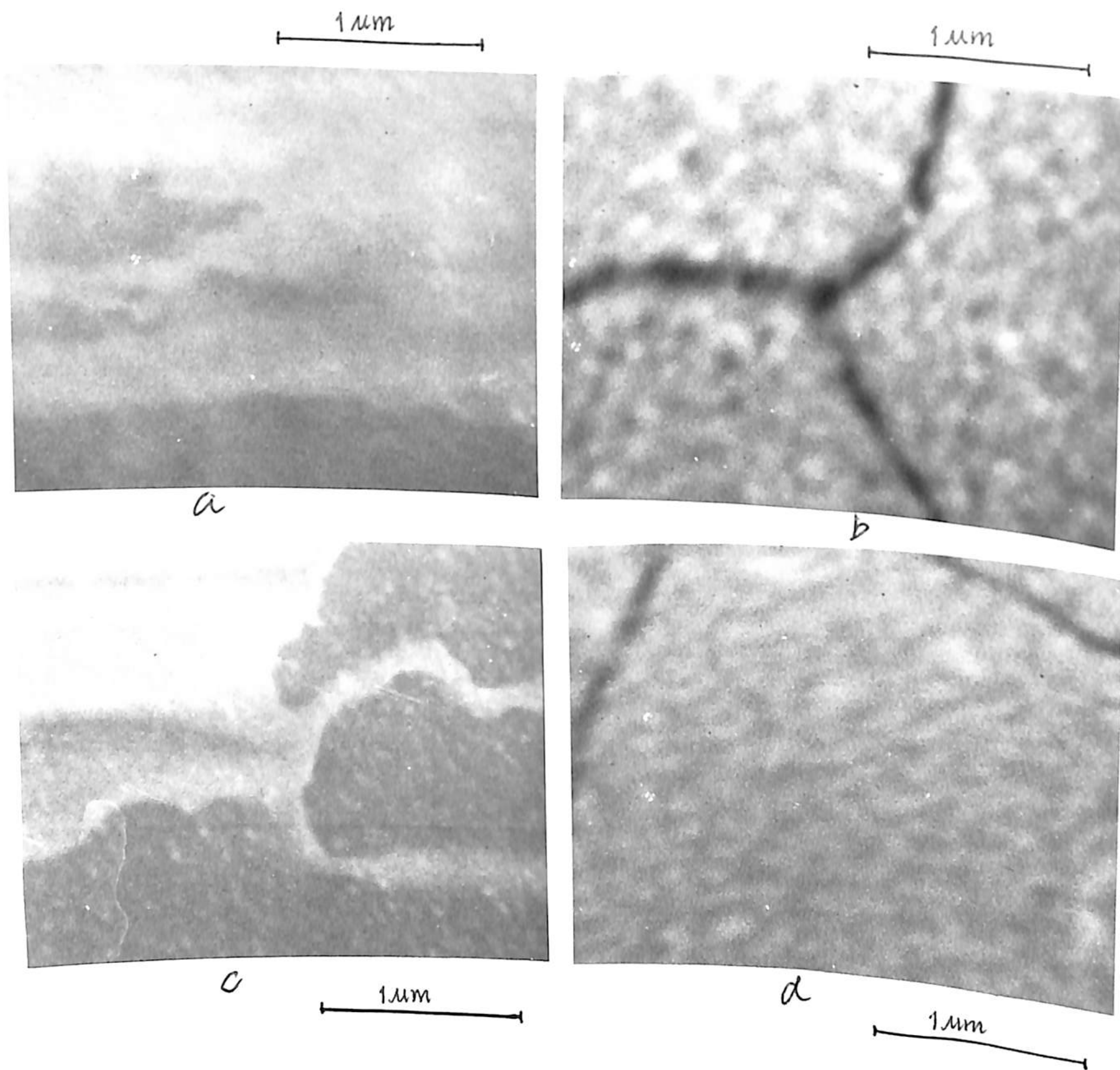

Figure 4.9: Scanning electron micrograph of $BaTiO_3$ precursor thin films on fused silica substrate. (a) & (b) made using EH precursor and annealed at 450°C & 800°C, respectively and (c) & (d) made using ME precursor and annealed at 450°C & 800°C, respectively.

Table 4.1: comparison of the properties of $BaTiO_3$ thin films deposited using barium 2-ethyl hexanoate (EH precursor) and barium hydroxide dissolved in 2-methoxy ethanol (ME precursor) as two different barium sources

Property	Curing temperature	EH precursor	ME precursor
Structure	> 600°C	tetragonal a = b = 3.995Å c = 4.05Å	cubic a = b = c =4.005Å
Organic content	< 400°C > 400°C	high very low	low very low
Shrinkage	300–500°C 500–700°C Above 700°C	35% ≈ 12% shows increase in thickness	10% ≈ 12% shows increase in thickness
Refractive index	At 600°C	2.00	2.08
Surface morphology	> 700°C	porous	dense

and 4.6). The films fabricated from ME precursor and annealed at 800°C shows fine mosaic structure without pores,while the films deposited from EH precursor shows some what porous structure. The porosity of the EH precursor films may be due to the larger organic content of barium 2-ethyl hexanoate precursor compared to that of barium hydroxide dissolved in 2-methoxy ethanol.

The properties of the sol-gel derived barium titanate thin films deposited using barium ethyl hexanoate and barium hydroxide as two different barium precursors were summerized in table 4.1.

4.2 Structural and Microstructural evolution in $SrTiO_3$ thin films made by sol-gel process

The precursor system used in the preparation of $SrTiO_3$ thin film was titanium isopropoxide and strontium 2-ethyl hexanoate. The structural and microstructural changes during heat treatment of $SrTiO_3$ precursor thin films made from the above precursors were expected to have the similar behaviour as that of the $BaTiO_3$ films made from similar precursors. However some changes are expected in the evolution process due to the difference in crystal structure.

4.2.1 FTIR studies

The FTIR spectrum of $SrTiO_3$ precursor films have been recorded after the films have been cured at temperatures of 30, 150, 250, 350, 450, 550 and 650°C . Since the coating solution was prepared from acetyl acetone complexed titanium isopropoxide, strontium ethyl hexanoate and water, partial hydrolysis of alkoxide and possible cross reactions must have taken place. The complex nature of the FTIR spectra of the $SrTiO_3$ supports this fact. In order to resolve this spectra, different components of the precursor solution were examined separately. Figure 4.10(a) shows the FTIR spectrum of titanium isopropoxide chelated using 1 mol of acetyl acetone (acac). The absorption bond of 620cm^{-1} is due to titanium isopropoxide and bands at 1590 and 1530cm^{-1} are due to ac ac groups bonded to Ti. This bonding increases the co ordination of Ti from 4 to 5 as indicated in equation 1.14 (chapter 1).

Figure 4.10(b) shows the FTIR spectrum of strontium ethyl hexanoate, which shows strong absorption bands in the 1300-1600cm^{-1} region due to symmetric and asymmetric stretching vibration of the carboxylate groups. Figure 4.10(c) is the FTIR spectrum of strontium ethyl hexanoate precursor cured at 400°C , which shows a peak at 1430cm^{-1} showing the pyrolysis and subsequent transformation of strontium ethyl hexanoate into strontium carbonate.

Figure 4.11(a)-(g) shows the FTIR spectrum of $SrTiO_3$ precursor films fired at 30, 150, 250, 350, 450, 550 and 650°C respectively. The absorption band seen around 3400cm^{-1} in figure 4.11(a) which is progressively decreasing in intensity (see figure

4.11(b)) is due to hydroxyl group attached with the $SrTiO_3$ precursor film which arise due to the hydrolysis of titanium isopropoxide. The decrease in its intensity can be attributed to the condensation reaction. The exact nature of these hydroxyls (vicinal, germinal or isolated) cannot be judged as they are not resolved in the spectra. The absorption bands at 2800-3000cm^{-1} is due to OH stretching. Here also, the bands show decrease in intensity after curing at elevated temperatures. These bands are absent in spectra of films cured above 450°C showing removal of organics.

A comparison of the band in the region of 1400- 1600cm^{-1} with that of pure strontium ethyl hexanoate and titanium isopropoxide show that most of these bands are due to organics belonging to the constituents. The bands and 1590cm^{-1} and 1530cm^{-1} which are due to formation of titanium isopropoxide-acac complex is nearly masked by the strong carboxylate bands. The intensity of these bands also decreases and vanishes above a curing temperature of450°C showing removal of organics. The bands at 2335-2350cm^{-1} are due to CO_2 absorbed on the films which have evolved from the pyrolysis of organic contents of the films. As pyrolysis of the films contineous it is seen that a new band is appearing at 1015cm^{-1} . This new band may be due to the formation of some new bonds in the precursor. A comparison of the spectra of strontium ethyl hexanoate cured at 400°C (figure 4.10(c)) shows that this band is not due to strontium compounds like SrO or $SrCO_3$. Thin film of titanium isopropoxide-acac complex hydrolyzed and cured at 400°C also do not show this peak. This new band may be due to a reaction between strontium oxide and titanium oxide, (at 400°C most of the other organic molecules pyrolyzes, and the position of the bands rules out strontium carbonate) possibly the formation of Sr-O-Ti bond.

The low frequency region of the spectrum shows a mixture of bands due to carboxylate group and alkoxides. The formation of a new band around 450cm^{-1} for samples cured above 500°C is due to crystallization of strontium titanate.

4.2.2 Optical Properties: (UV-Visible)

Optical properties of $SrTiO_3$ thin films were studied from the optical transmission spectra recorded in the wavelength range of 200 to 1100 nm. The films used in this study were deposited on 1 mm thick fused silica substrates. Calculation of the

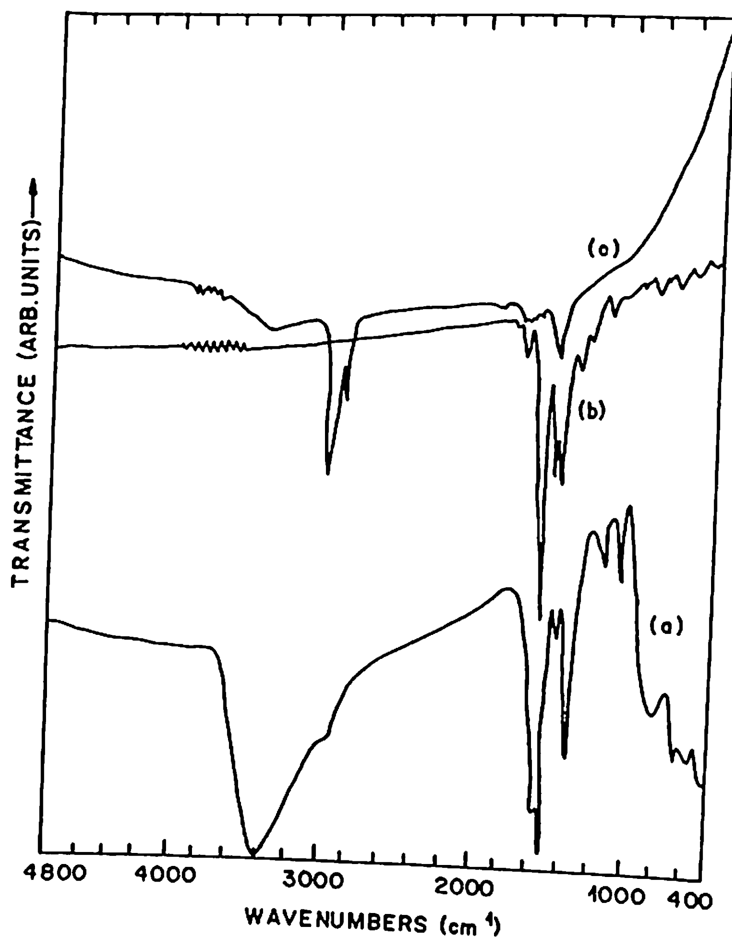

Figure 4.10: FTIR spectra of thin films of (a) $Ti(OC_3H_7)_4$ chelated using 1 mole acetyl acetone (b) $Sr(C_7H_{15}COO)_2$ at room temperature and (c) $Sr(C_7H_{15}COO)_2$ at 400°C .

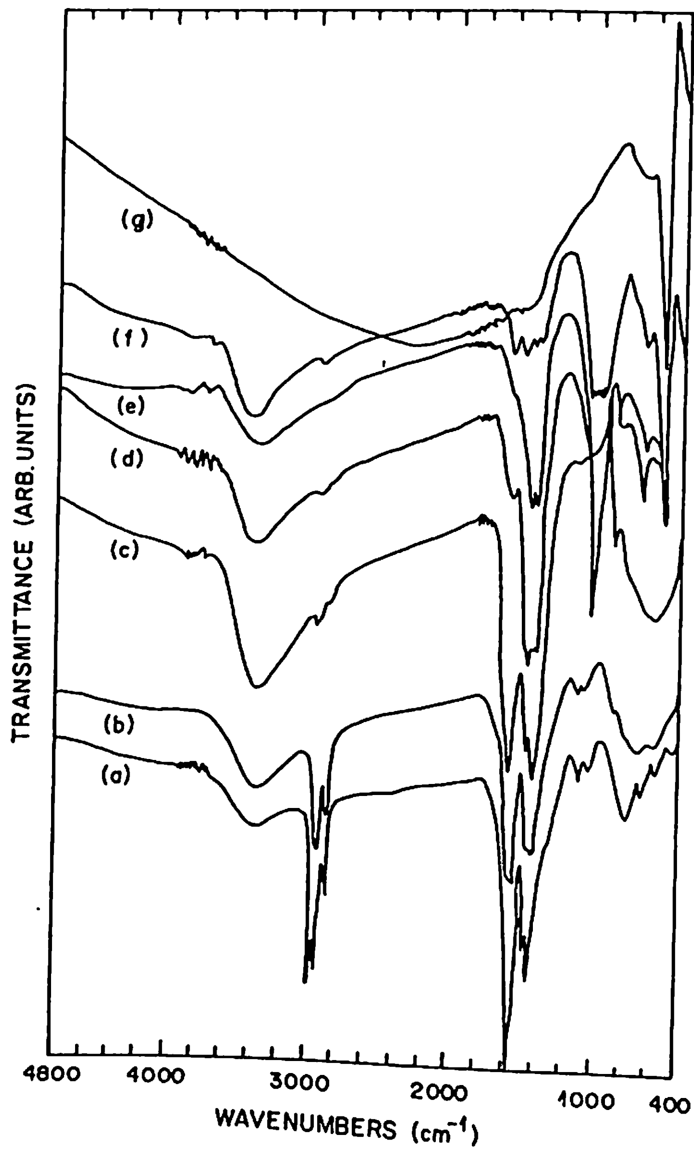

Figure 4.11: FTIR spectra $SrTiO_3$ thin film annealed at different temperatures.

refractive index and thickness of the films were done by the method developed by Manifacier et al [19].

Figure 4.12 shows the variation of thickness of $SrTiO_3$ thin films with annealing temperature. The films show sharp shrinkage in the range 300°C to 450°C (about 35%). This shrinkage may be due to the attractive force provided by the bond formation during condensation reaction. The increase in pore volume fraction created by the removal of organics may weaken the gel structure, resulting in the collapse of gel network leading to the shrinkage of the film. Above 450°C the reduction in thickness is low and it is attributed to the structural relaxation.

The variation of refractive index with annealing is represented in figure 4.13. At 300°C the films have a refractive index of 1.69. It increases with curing temperature and attains constant value 1.93 around 600°C , this indicates the the maximum densification of the films.

Figure 4.14 shows the wavelength dispersion curve of $SrTiO_3$ thin film. The dispersion curve is fairly flat above 600 nm and rises rapidly towards shorter wavelength region, showing the typical shape of dispersion curve near an electronic interband transition [21]. It has been shown by DiDomenico and Wample [22] that refractive index of a material near an electronic interband transition is related to the wavwlength λ as

$$n^2 - 1 = \frac{S_o \lambda_o^2}{1 - (\lambda_o/\lambda)^2} \quad (4.2)$$

where λ_o is the average oscillator position and S_o is an average oscillator strength. This means that the quantity $(1/n^2) - 1$ should be proportional to $1/\lambda^2$. Figure 4.15 plotted between the above quantities shows a straight line behaviour indicating the validity of DiDomenico model in the observations made here.

Figure 4.16(a) and (b) shows the transmission spectra of $SrTiO_3$ thin film annealed 400°C and 550°C respectively. The film annealed at 400°C was amorphous having band gap of about 3.8 eV. The band gap for the film annealed at 550°C was about 3.4 eV, which is near the single crystal value reported [23]. The change in band gap from 3.8 to 3.4 eV suggest the occurence of crystallinity in the film annealed at 550°C . This fact was supported by XRD and FTIR studies.

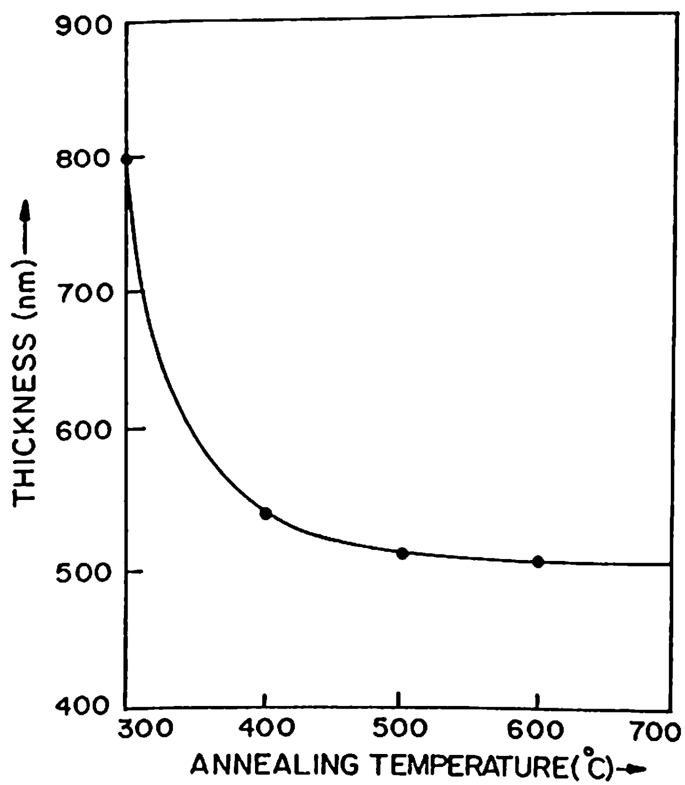

Figure 4.12: Variation of thickness with annealing temperature of $SrTiO_3$ thin film on fused silica substrate.

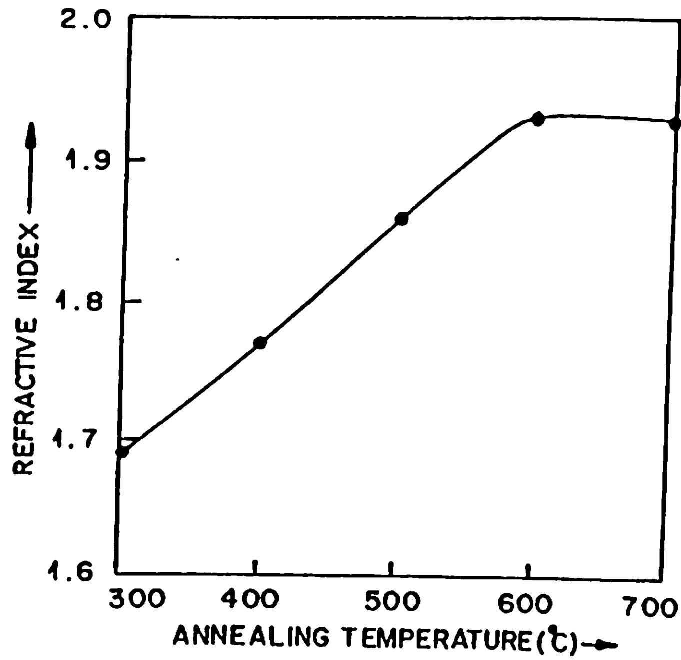

Figure 4.13: Variation of refractive index with annealing temperature of $SrTiO_3$ thin film on fused silica substrate.

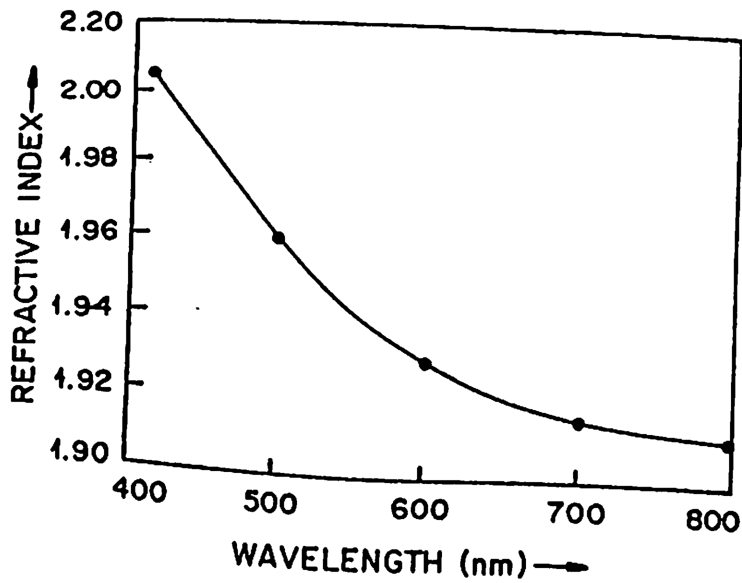

Figure 4.14: Wavelength dispersion curve of $SrTiO_3$ thin film on fused silica substrate.

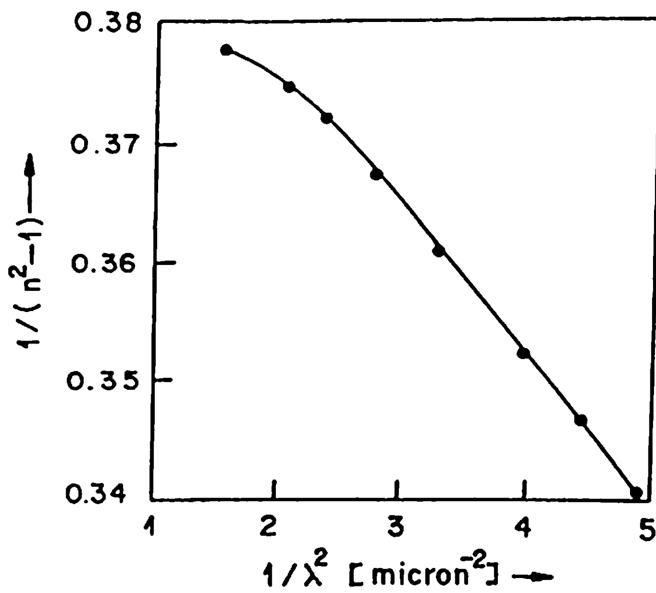

Figure 4.15: Plot representing Didominico-Wemple single electronic model for inter-band transition.

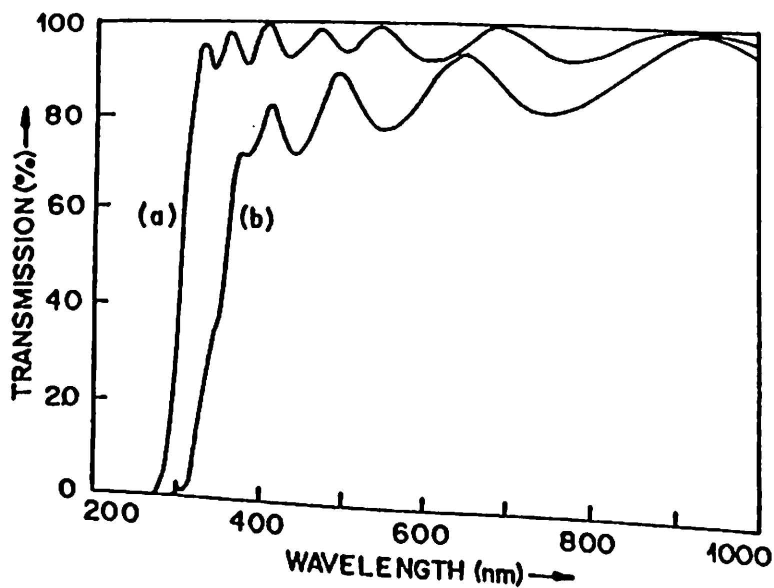

Figure 4.16: Transmission spectra of $SrTiO_3$ thin film on fused silica substrate an-nealed at (a) 400°C and (b) 550°C .

4.2.3 X-ray diffraction studies

Figure 4.17(a)-(d) show the X-ray diffraction spectra of $SrTiO_3$ thin films deposited on silicon (100) substrates and annealed at temperatures 400, 500, 600, and 700°C respectively. The spectrum of sample annealed at 400°C was found to be amorphous. At 500°C the film start crystallizing, as indicated by the emergence of characteristic peaks of $SrTiO_3$. XRD spectra of samples annealed at 600°C and 700°C shows increase in peak heightsindicating improved crystallinity. The calculated values of the lattice parameters indicate that $SrTiO_3$ thin films were crystallized in cubic form. Lattice parameters calculated from the d values of the peaks in the spectrum are $a = b = c = 3.90$Å, which was in good agreement with the ASTM values (data card # 5-634).

The XRD spectra shows the onset of crystallization around a temperature of 500°C . It is interesting to note that the change in optical absorption edge in the UV-visible spectra and the appearence of a new band at 450cm^{-1} in the FTIR spectra also appear in the sample around 500°C .

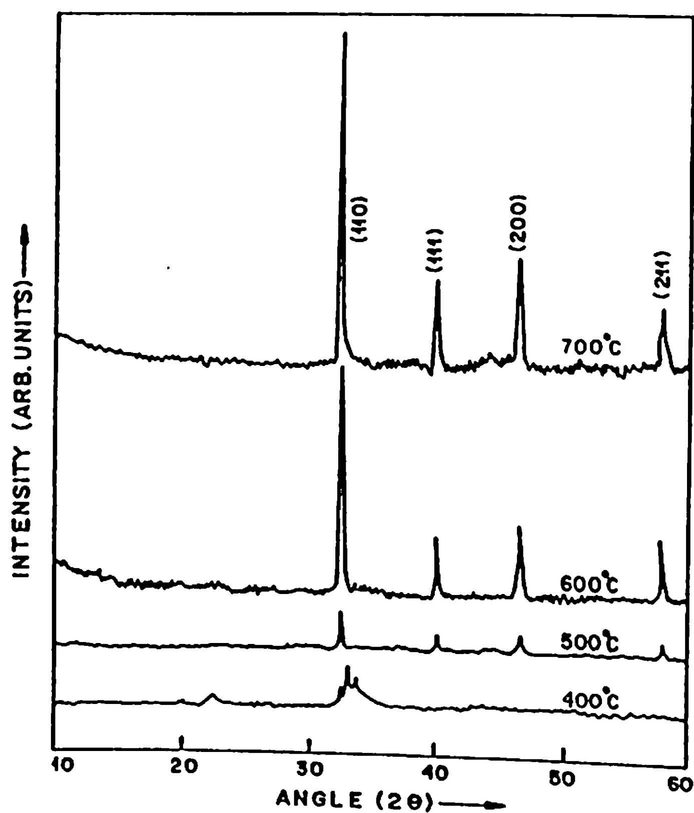

Figure 4.17: XRD spectra of $SrTiO_3$ thin film on fused silica substrate annealed at diffrent temperatures.

References

1. G. M. Davis and M. C. Gower, Appl. Phys. Lett. 55, 112 (1989).
2. P. Li, J. F. McDonald and T. M. Lu, J. Appl. Phys. 71, 5596 (1992).
3. G. Tomandl, H. Rosch and A. Stiegelschmitt, Mat. Res. Soc. Symp. Proc. 121, 281 (1988).
4. N. D. S. Mohallem, M. A. Aegerter, Mat. Res. soc. Symp. Proc. 121, 515 (1988).
5. H. B. Sharma, R. P. Tandon, A. Mansingh and R. Rup, J. Mater. Sci. Lett. 12, 1795 (1993).
6. M. N. Kamalasanan, S. Chandra, P. C. Joshy, A. Mansingh, Appl. Phys. Lett. 59, 3547 (1991).
7. M. N. Kamalasanan, N. D. Kumar and S. Chandra, J. Appl. Phys. 74, 5679 (1993).
8. K. S. Mazdiyasni, R. T. Dolloff and J. S. Smith, J. Am. Ceram. Soc. 52, 523 (1969).
9. M. H. Frey and D. A. Payne, Appl. Phys. Lett. 63, 2753 (1993).
10. Y. Nosaka, M. Jimbo, M. Aizawa, N, Fujii and R. Igarashi, J. Mater. Sci. Lett. 10, 406 (1991).
11. T. Nanao, T. Eguchi, US Patent 4, 668,299 (1987).
12. S. S. Flaschan, J. Am. Chem. Soc.77, 6194 (1955).
13. J .J. Ritter, R. S. Roth and J. E. Blendell, J. Am. Ceram. Soc. 69, 155 (1986).
14. K. Y. Chen, L. L. Lee and D. S. Tsai, J. Mater. Sci. Lett. 10, 1000 (1991).
15. K. H. Yoon and K. S. Chung, J. Appl. Phys. 72, 5743 (1992).

16. M. I. Diaz-Guemes, T. G. Carreno, C. J. Serna and J. M. Palacois, J. Mater. Sci. 24, 1011 (1989).

17. R. T. Mara, G. B. B. M. Sutherland and H. V. Tyrell, Phys. Rev. 96, 801 (1954).

18. J. T. Last, Phys. Rev. 105, 1740 (1957).

19. J. C. Manifacier, J. Gasiot and J. P. Fillard, J. Phys. E, 9, 1002 (1976)

20. C. J. Brinker and G. W. Scherer, *Sol-Gel Science: The physics and chemistry of sol-gel processing* (Academic Press Inc. New York) 1990 P. 555.

21. M. Wohlecke, V. Marrello, and A. Onton, J. Appl. Phys. 48,1748 (1977).

22. M. Ddomenico Jr, and S.H. Wimple, J. Appl.Phys. 40, 720, (1969)

23. G. A. Barbosa, R.S. Katiyar, and S.P.S. Porto, J.Opt. Soc. Am. 68,610 (1978)

Chapter 5

Electrical and Dielectric Properties of $BaTiO_3$ Thin Films Grown by Sol-Gel Process

Transparent smooth and crackfree $BaTiO_3$ thin films were deposited on stainless steel, fused silica, platinum plates and platinized silicon wafers (100) using sol gel process. Barium 2-ethyl hexanoate and titanium isopropoxide were used as precursors. The films were annealed at 750°C for 15 minutes to get polycrystalline films.The electrical properties of the films prepared on stainless steel substrates showed electrode barrier effect whereas those prepared on platinum substrates were susceptible to ambient atmospheric humidity. However, films grown on platinum substrates and measured under dry conditions were showing very good electrical properties. Amorphous thin films of $BaTiO_3$ were used in MIS configuration and their C-V and I-V characteristics were studied. Ferroelectric hysteresis and C-V characteristics were also studied on these films. The electrical properties of $BaTiO_3$ was measured on films deposited on stainless steel substrates, platinized silicon wafer and polished platinum plates. The top electrode of the Metal-Insulator-Metal (MIM) structure was vacuum deposited gold dots of diameter 1mm and thickness $3\mu m$.

5.1 Dielectric and electrical properties of polycrystalline $BaTiO_3$ thin films

5.1.1 Dielectric properties of $BaTiO_3$ thin films on stainless steel substrates

Thin films of $BaTiO_3$ made on stainless steel substrates showed dielectric relaxation at a frequency of about 1 kHz. Figure 5.1 gives the curve showing the variation of the dielectric constant ϵ' and dielectric loss ϵ'' as a function of frequency, of a 1μm thick $BaTiO_3$ film deposited on stainless steel substrate. As the frequency is increased ϵ' continuously decreased whereas ϵ'' shows a peak around 1 kHz. Further ϵ' shows extraordinarily large dispersion with frequency (ϵ' decreased to nearly 30% of its initial value when the frequency is increased from 100 Hz to 1 MHz). The inset of figure 5.1 shows the variation of ϵ' with film thickness for different frequencies. ϵ' was found to increase linearly with increase in film thickness. This result is a typical case of an electrode barrier capacitance. In the case of an electrode barrier capacitance C_s , the measured capacitance C_{meas} of an MIM structure can be expressed as

$$C_{meas} = (\epsilon'\epsilon_o A)\frac{1}{d} + C_s \tag{5.1}$$

where A is the area of the film, d the thickness, ϵ' the dielectric constant and ϵ_o the permittivity of the vacuum. From this equation the measured dielectric constant C_{meas} can be written as

$$\epsilon'_m eas = \epsilon' + C_s\frac{d}{\epsilon_o A} \tag{5.2}$$

where ϵ'_{meas} is taken as (C_{meas} $\times$ (d/ϵ_o A). This means that in presence of a surface barrier capacitance the measured dielectric constant will increase linearly with increase in sample thickness, which is in agreement with the present observation. The value of barrier capacitance calculated from the slope of the graph showing ϵ'_{meas} against the sample thickness d at 100 Hz was 1.1 nF.

The formation of an electrode barrier in $BaTiO_3$ thin film on stainless steel can be explained as due to the diffusion of transition metal elements like Fe and Ni present in the stainless steel in to the surface layer of the thin film, making it p-type having a large resistivity [1]. This large resistance will act as a series resistance with

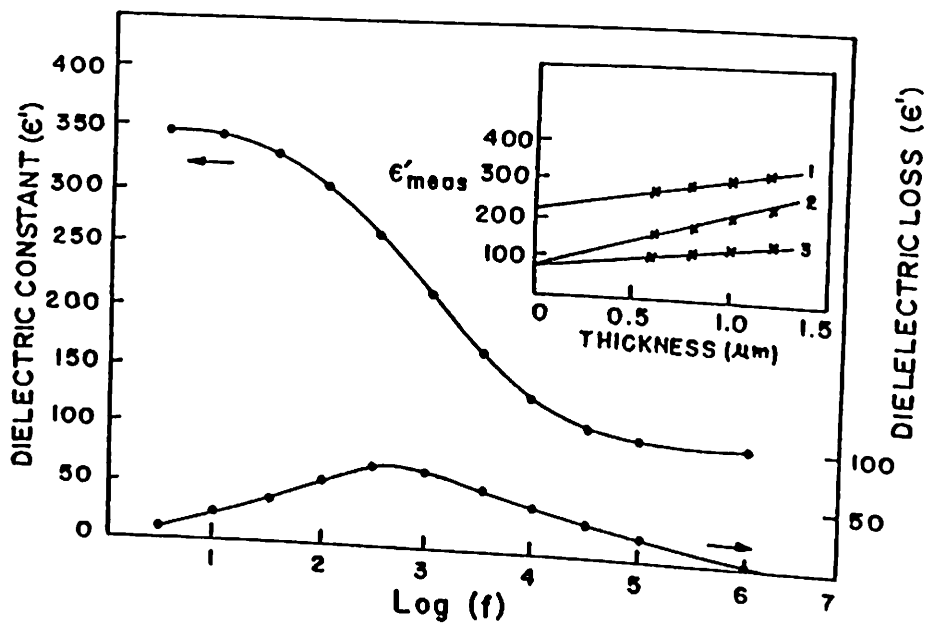

Figure 5.1: Variation of ϵ' and ϵ'' as a function of frequency of $BaTiO_3$ thin film made on stainless steel substrate. Inset : Variation of ϵ' with film thickness for frequencies (1) 1 kHz. (2) 10 kHz and (c) 100 kHz.

the sample, there by forming an electrode barrier.

5.1.2 Effect of humidity on the dielectric behaviour of $BaTiO_3$ thin films on platinum substrates

The electrical properties of $BaTiO_3$ thin films grown on platinum substrates were found to be highly influenced by the humidity of the ambient atmosphere. Figures 5.2 and 5.3 show the variation of dielectric constant ϵ' and dielectric loss ϵ'' with temperature for different frequencies for a $2.5\mu m$ thick $BaTiO_3$ film grown on platinum substrate. The relative humidity of the atmosphere was 35%. At room temperature ϵ' and ϵ'' were large compared to that of the film on stainless steel substrate. As the temperature is increased, ϵ' as well as ϵ'' increased and reached a maximum at about 40^oC and then decreased with further increase in temperature for all measured frequencies. However when the sample was cooled down from high temperature,ϵ' as well as ϵ'' was found to follow a different path from the heating up curves. The room temperature value of ϵ' and ϵ'' after the heating cooling cycle was much lower than that at the beginning of the cycle. ϵ' and ϵ'' however regained their original value when the sample was kept in ambient air for two hours.

To study the effect of humidity on the dielectric measurements, samples were kept in a dry box in flowing dry air. Figure 5.4 and 5.5 shows the variation of dielectric constant and dielectric loss as a function of the time for which the dry air has been flown through the dry box holding the sample. The measurement showed a sudden decrease in the value of ϵ' and ϵ'' at the instant when the air start flowing through the sample holder. After 5 minutes of flow dry air, the values of ϵ' and ϵ'' was found to decrease and stabilize to a lower value at room temperature than that in humid air.

It has been reported by Mountvala [2] that the electrical properties of $BaTiO_3$ can be affected by moisture and this property has been related to the microstructure of the material and that samples having smaller grain size were more affected by moisture than that of larger grain size. Films prepared by sol gel process have fine microstructure and may have large porosity as well as uncondensed hydroxyl groups on the surface which may make the film more susceptible to humidity.

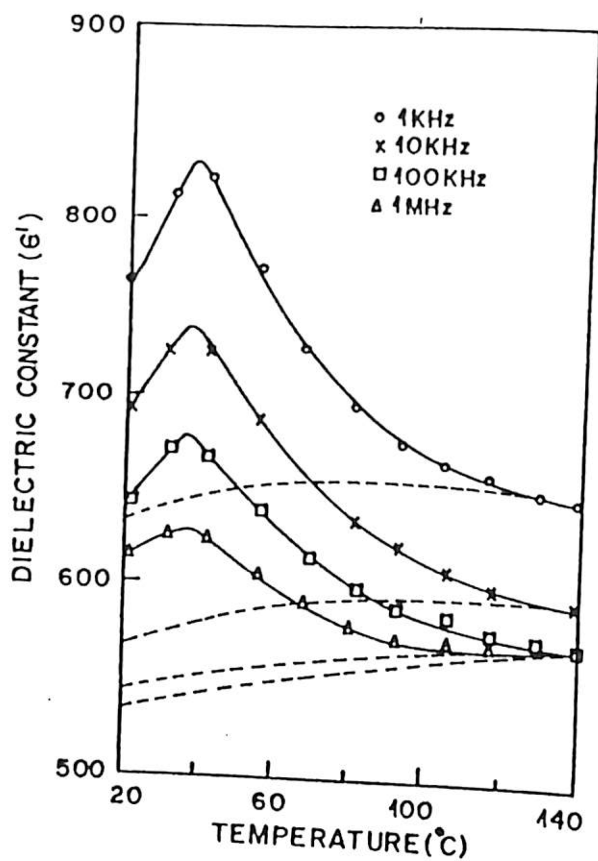

Figure 5.2: Variation of ϵ' with temperature for various frequencies in ambient air. Dotted lines represent the corresponding cooling down curves.

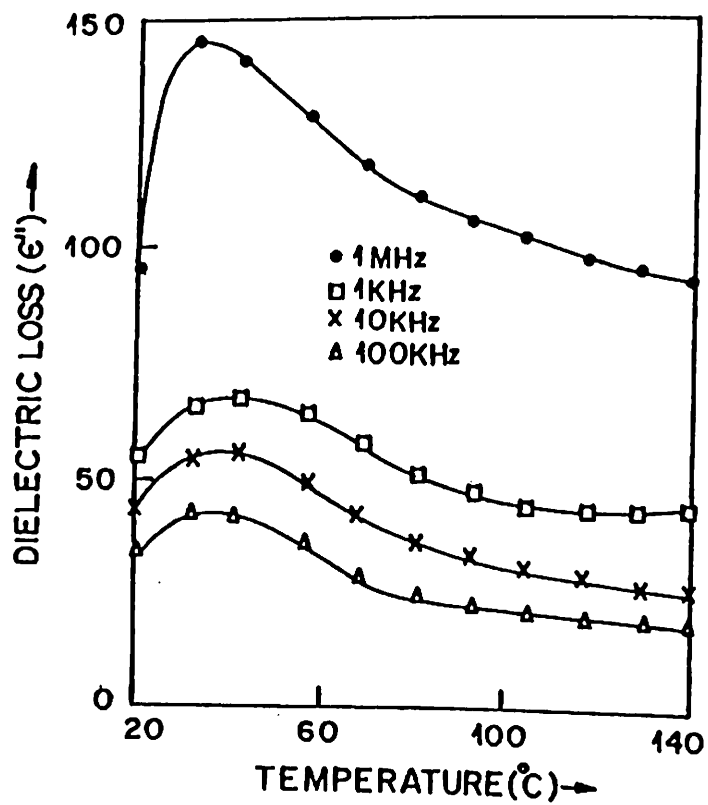

Figure 5.3: Variation of ϵ'' with temperature for various frequencies in ambient air.

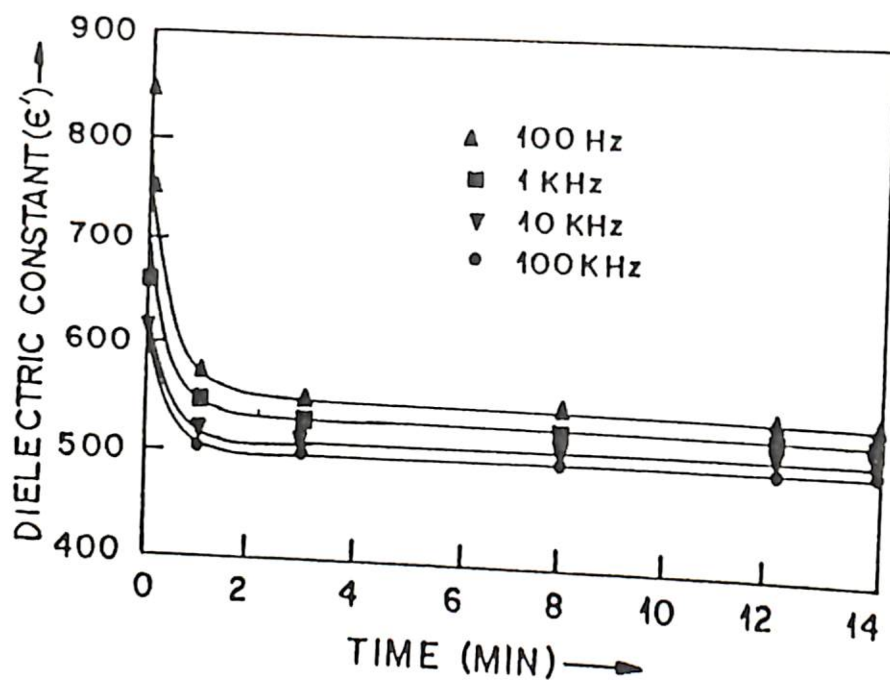

Figure 5.4: Variation of ϵ' as a function of the time for which oxygen has been flown through the sample holder.

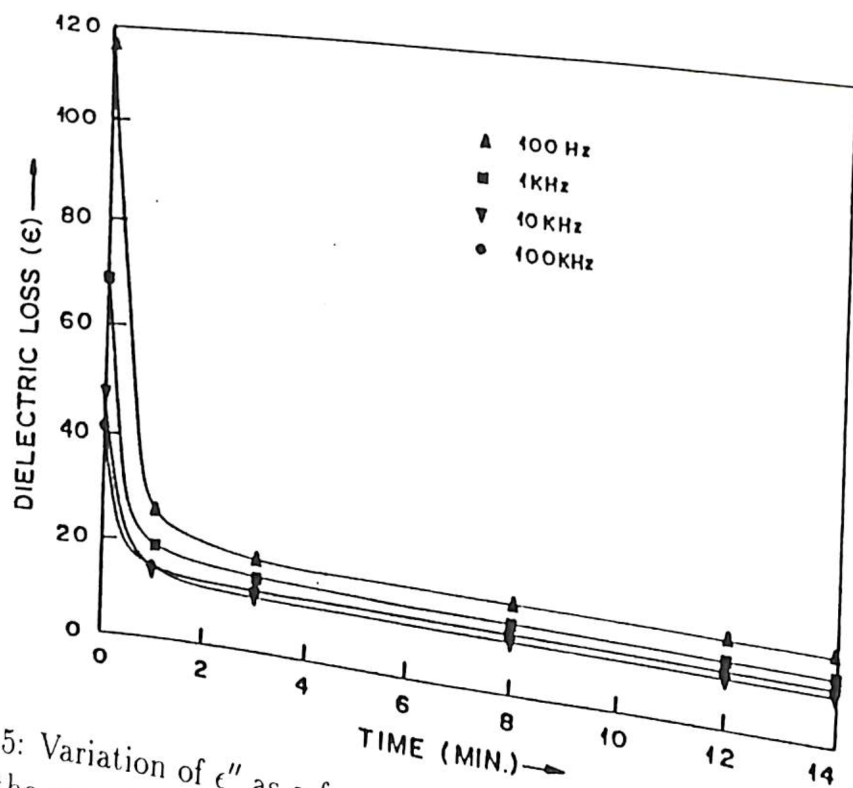

Figure 5.5: Variation of ϵ'' as a function of the time for which oxygen has been flown through the sample holder.

Figure 5.6 shows the variation of ϵ' with temperature of the film in flowing dry air. ϵ' increases with increase in temperature and shows a maximum at 117°C . Figure 5.7 shows the temperature dependence of ϵ'' of the film on platinum strip in dry air. ϵ'' at room temperature was much smaller than that in ambient air for all measured frequencies. At low frequencies ϵ'' increased with increase in temperature, came to a plateau at about 120°C and then increased again with further increase in temperature. At higher frequencies, the nature of the curves were the same except that the rate of increase of ϵ'' with temperature was much lower. However, ϵ'' at higher frequencies (1MHz) show a slight decrease with increase in temperature.

The peak of ϵ' vs temperature curve as well as the plateau of ϵ'' versus temperature curve denote ferroelectric to paraelectric transition in the film. The transition temperature obtained in the present study is 117°C which is in agreement with that reported by earlier workers for $BaTiO_3$ films grown by sol gel process [3,4]. Since $BaTiO_3$ films grown by sol-gel technique on platinum substrates and measured under dry conditions give better dielectric properties than that on stainless steel substrates and under ambient atmosphere, all further studies were carried out on films grown on platinum strip and measured under flowing dry air conditions.

In figure 5.8 variation of ϵ' and ϵ'' is shown against frequency for $BaTiO_3$ thin film at 20, 105 and 190°C . At 20°C and 105°C ϵ' show very low dispersion with frequency where as at 190°C , the dispersion is larger. At 20°C the variation of ϵ'' with frequency is very low, where as at higher temperature, the low frequency part of ϵ'' shows very high value. This may be due to the increase in number of free carriers thermally generated in the sample. The low dispersion in ϵ' and the absence of any relaxation peak in ϵ'' indicate that interfacial polarization of the Maxwell-Wagner (MW) type as well as that due to electrode barrier are negligible in the sample.

5.1.3 Electrical conductivity in crystalline $BaTiO_3$ thin films

Figure 5.9 shows the ac conductivity σ_ω of the film as a function of frequency f. Log(σ_ω) is plotted against log f for temperatures 20, 105 and 190°C . For frequencies below 5×10^4 Hz, the slope of the curves are less than 1 (ie. 0.89 at 20°C , 0.84 at 105°C and 0.77 at 190°C) where as for frequencies above 5×10^4 Hz, all the curves

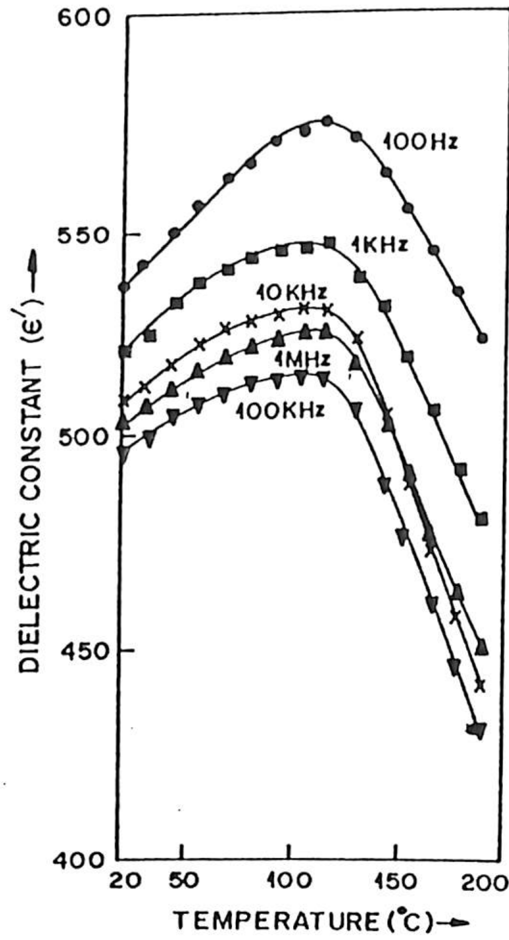

Figure 5.6: Variation of ϵ' as function of temperature for $BaTiO_3$ on Pt for different frequencies in dry conditions.

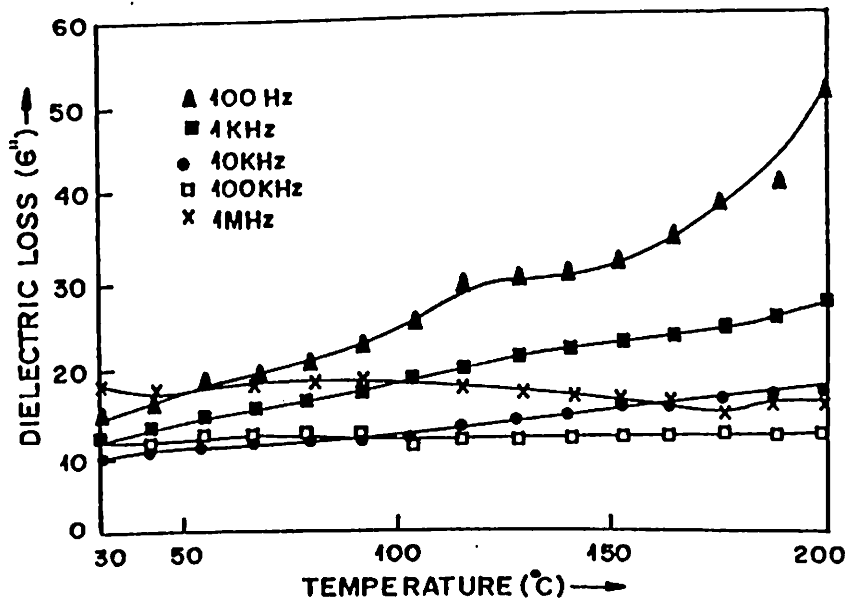

Figure 5.7: Variation of ϵ'' as function of temperature for $BaTiO_3$ on Pt for different frequencies in dry conditions.

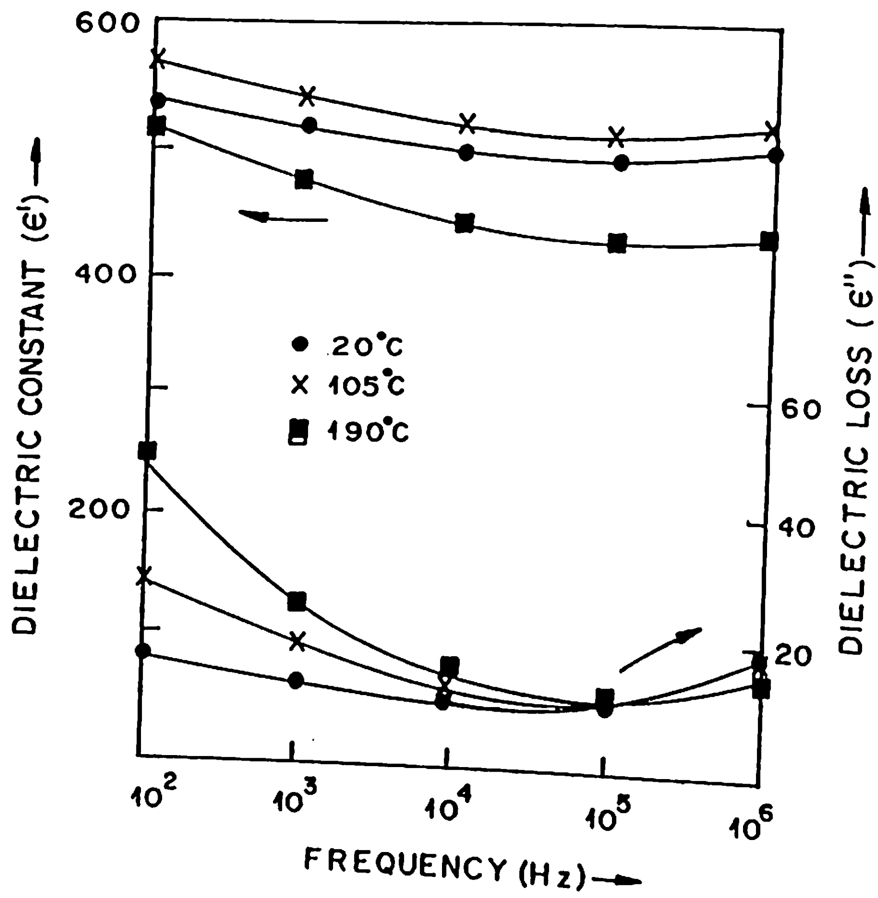

Figure 5.8: Dependence of ϵ' and ϵ'' as a function of frequency of ac signal at different temperatures.

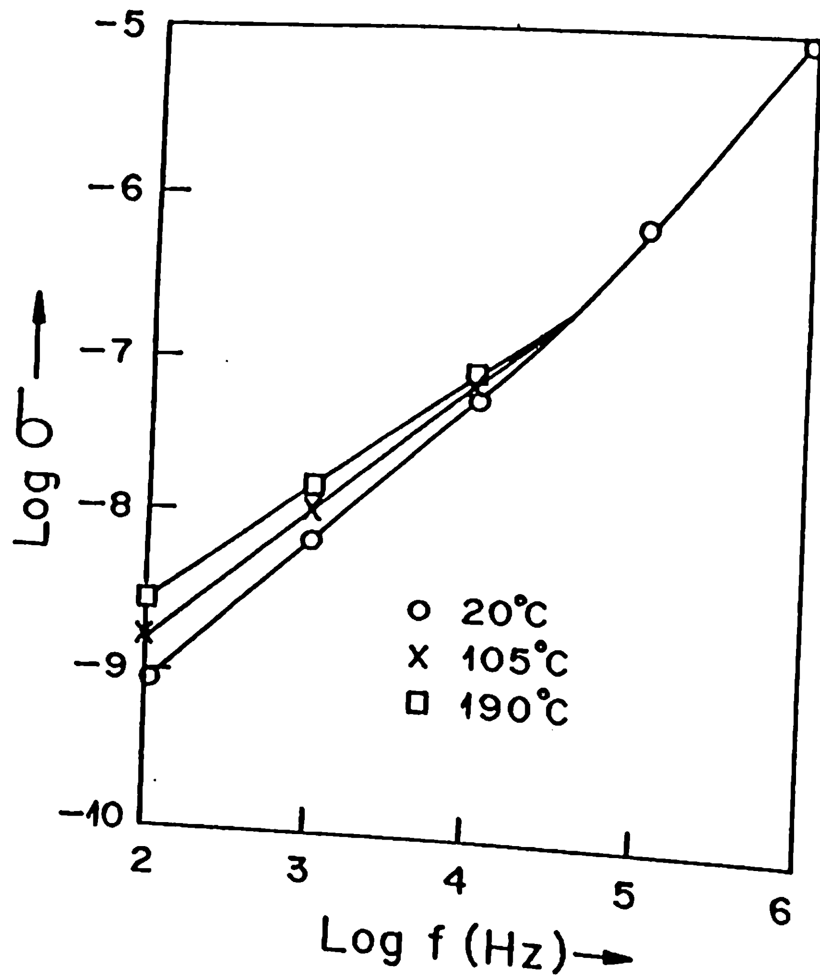

Figure 5.9: Frequency dependence of ac conductivity of $BaTiO_3$ thin film on Pt substrate.

nearly join together with a slope of 1.2.

The temperature dependence of conductivity σ_ω of sol-gel grown $BaTiO_3$ films were measured in the range of 305 500 K. The result obtained are shown in the figure 5.10 where log σ_ω is plotted as a function of 1000/T for various frequencies. On the higher temperature side of the plot, σ_ω shows a bending denoting the presence of thermally generated carriers. The dc conductivity curve shows a sudden bending at around 120°C and the low frequency ac conductivity plot show a sudden change around 117°C . The curves representing higher frequency remain temperature independent. The activation energy for dc conduction has been calculated from the straight portion of σ_{dc} vs 1000/T plot. The low and high temperature part give activation energies of 0.6 eV and 0.8 eV respectively. The room temperature value of the resistivity of the sample could not be measured due to the low value of leakage current, but was estimated by extrapolating the σ_{dc} versus 1000/T curve to room temperature to be about 10^{15} Ω -cm. The break down field of the films were about 2×10^5 V/cm.

The sudden change in the conductivity curves around 117°C denotes the tetragonal to cubic phase transition. It seems that the phase transition affects the energies of the trapped carriers also thereby affecting in an increase in the activation energy for dc conduction process. Similar effect is seen in the curve showing temperature dependence of ϵ'' also where the curve changes its nature around 117°C . The low breakdown field ($\approx 2\times 10^5$ V/cm) observed may be due to the formation of large crystallites on the film with electrodes on both sides in which case the breakdown field of the film will be the same as that of $BaTiO_3$ crystals ($\approx 10^5$ V/cm) [5]. The ac conductivity of $BaTiO_3$ film can rise from both bound as well as free charge carriers. The frequency response due to the free carriers can be written as [6],

$$\sigma(\omega) = \sigma_{dc}\frac{1}{1 + \omega^2\tau^2} \qquad (5.3)$$

τ is the relaxation time. According to this equation, the conductivity due to free carriers must decrease with increase in frequency ω . In our sample,the ac conductivity σ_ω increases with increase in frequency and therefore the observed ac

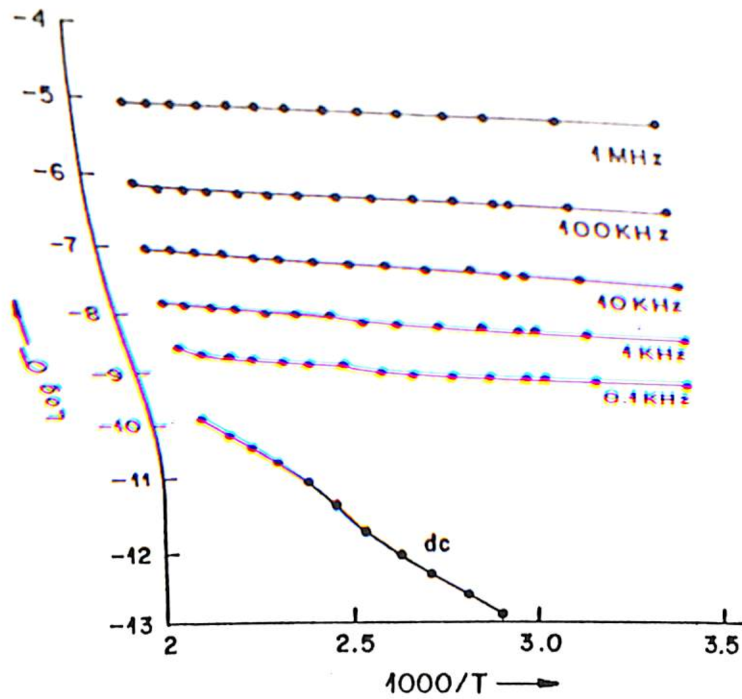

Figure 5.10: Variation of conductivity with $1000/T$ for various frequencies.

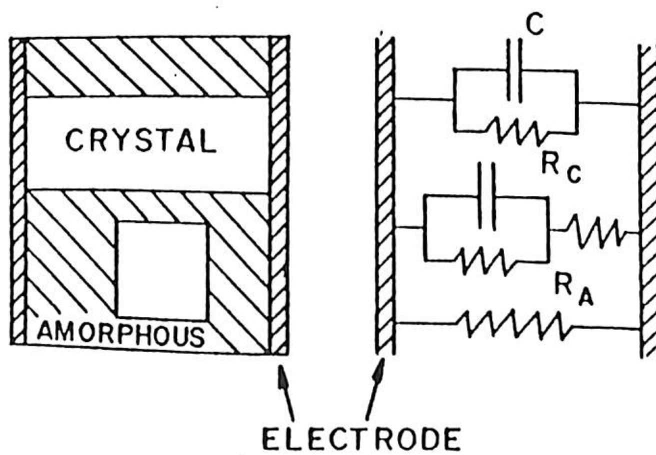

Figure 5.11: (a) Schematic diagram of the cross section of $BaTiO_3$ thin film in MIM configuration and (b) the equivalent electrical circuit.

conductivity must be related to the bound carriers trapped in the sample.

5.1.4 Mechanism of conduction in sol-gel $BaTiO_3$ thin film on platinum substrates

The frequency dependent ac conductivity of dielectric thin films are usually influenced by three process, (a) Schottky barrier at metal-dielectric interface, (b) Maxwell-Wagner (MW) type dispersion due to inhomogeneities existing in the material giving rise to a spatial variation in conductivity [7] and (c) hopping type conduction between localized states. The presence of any electrode barrier has not been observed in our films as evidenced by the low dispersion of ϵ' . Further, it has been suggested [6] that a final check of electrode can be made by observing the sharp drop of sample capacitance in conductivity regime of the sample where the ac conductivity has a superlinear dependence ($\sigma_\omega \propto \omega^2$) on frequency and a saturation of conductivity at higher frequencies. In our sample, a superlinear dependence of ac conductivity with frequency starts at about 5×10^4 Hz. But the absence of corresponding drop in the sample capacitance as well as the absence of saturation of the conductivity regime suggests there are no appreciable electrode resistance in our samples.

Interfacial polarization due to Maxwell-Wagner(MW) type dispersion is expected in materials where two different phases (amorphous and crystalline in the present case) coexist. The crystalline phase in $BaTiO_3$ have a large dielectric constant (and hence has large capacitance) whereas that of amorphous phase is very small and hence has negligible capacitance. Therefore, the system comprising of crystalline and amorphous regions can be visualized as a large number of crytallites having large capacitances and small resistances interconnected by amorphous regions having large resistances. If C and R_C are the respective capacitance and resistance of a crystallite and R_A the resistance of the amorphous region which connects the crystallite to the electrode, and we neglect the small capacitance of amorphous regions then the parallel capacitance C_P and conductance G_P of the crystallites-amorphous matrix assembly can be written [6] as

$$C_p = C\frac{1}{(1 + R_A/R_C)^2 + \omega^2 R_A^2 C^2} \tag{5.4}$$

$$G_p = \frac{1}{R_C}\frac{(1 + R_A/R_C) + \omega^2 R_A R_C C^2}{(1 + R_A/R_C)^2 + \omega^2 R_A^2 C^2} \qquad (5.5)$$

In our films, electron microscopy shows that the dimensions of many crystallites are large enough to be directly connected with the electrodes on both sides. A schematic diagram showing the cross section of the film and its equivalent electrical network is shown in figures 5.11(a) and 5.11(b). In our conductivity studies (figure 5.10) we have observed that the ac as well as dc conductivity of the films show a change in the 117-120°C temperature region corresponding to the crystallographic tetragonal-to-cubic transition. Therefore it is reasonable to believe that it is the crystalline phase which is sensitive to ac as well as dc conductivity changes in the measured temperature ranges and having a larger conductivity than the amorphous regions. If this is true, the amorphous region will have larger resistance than the crystallites and hence the amorphous region as well as those smaller crystallites which are connected to the electrode through amorphous region will contribute very little to the capacitance and the electrical conductivity of the film. The capacitance as well as the conductivity of the film will depend mainly on larger crystallites which are directly connected to the electrodes. On the other hand, if amorphous regions are having lower resistance than the crystalline regions, the conductivity of the film will be controlled by the amorphous regions and the capacitance of the film will show a dispersion with frequency. The low dispersion of dielectric constant with frequency of the crystallites directly connected with the electrodes on both sides (since the frequency range under investigation is far away from the resonant frequency of $BaTiO_3$) will be superimposed by a much larger dispersion due to the interfacial polarization from the crystal amorphous interface. The frequency-dependent electrical conductivity of the film also will show a polarization effect, ie. linear dependence of conductivity at low frequency and an ω^2 dependence at high frequencies followed by a saturation of conductivity.

In our sample we have a nearly linear dependence of conductivity on frequency at low frequencies ($\sigma_\omega \propto \omega^{0.89}$ at room temperature) and σ_ω at higher frequencies. But the absence of a dielectric dispersion in the $\omega^{1.2}$ regime and the absence of frequency dependent conductivity of the samples in the present study may not be due to interfacial polarization of the MW type.

In many insulating materials, frequency dependent ac conductivity has been observed due to thermally activated hopping of charge carriers with energies very near to Fermi level. The total conductivity of such material can be described by the experimental formula

$$\sigma(\omega) = \sigma_{dc} + \sigma_{\omega} \tag{5.6}$$

In $BaTiO_3$ films it is seen that σ_{dc} is a few order of magnitude smaller than σ_{ω} in the measured temperature ranges so that the measured $\sigma_{meas}(\omega)$ can be taken as σ_{ω} itself. The frequency dependent part of conductivity σ_{ω} has been observed to obey the relation

$$\sigma_{\omega} = A\omega^{s} \tag{5.7}$$

where A is a constant and s is a number $0.8 < s < 1$ at room temperature for frequencies between 10^2 to 10^5 Hz and s = 2 for higher frequencies. The low frequency value of s decreased with increase in temperature and was explained due to hopping between uncorrelated pairs of hopping centers where as the high frequency value of s was independent of temperature and was attributed due to hopping of charge carriers between equivalent hopping centers.

The result of the present investigation qualitatively agrees with the hopping model. However, the high frequency value of s obtained (i.e., 1.2) is much lower than 2 which is expected by the hopping model. The density of states near the Fermi level calculated from Pollak's expression [8].

$$\sigma_{\omega} = \frac{\pi^3}{96} e^2 kT[N(E_f)]^2 \alpha^5 \omega [\ln(\frac{\nu_{ph}}{\omega})]^4 \tag{5.8}$$

where α is the hopping distance and ν_{ph} the phonon frequency as $N(E_f) = 2.4 \times 10^{19}/\text{eV}/\text{cm}^3$

5.2 Dielectric and electrical properties of amorphous $BaTiO_3$ thin films in MIS configuration

Ferroelectric and dielectric thin films of high dielectric constant has been extensively investigated as a gate material for DRAM (Dynamic Random Access Memory) applications with an effort to increase the charge storage density. These materials possess

high dielectric breakdown strength and low leakage current. However, for such applications, ferroelectric properties such as polarization hysteresis are not required. In this regard amorphous $BaTiO_3$ thin films are very useful. Amorphous thin films of $BaTiO_3$ have low leakage current densities and high dielectric breakdown strength than crystalline $BaTiO_3$ thin films [9]. Moreover amorphous thin films are easy to fabricate and need to be processed only at low temperatures [10,11]. Amorphous $BaTiO_3$ thin films generally have a dielectric constant in the range 15 to 20 and this value meets with the requirements for the fabrication of high density memory devices.

5.2.1 C-V Characteristics of amorphous $BaTiO_3$ thin films on p-type silicon

MIS capacitance is extensively used to characterise insulating thin films and semiconductor surface. The C-V measurement on an MIS device can give information about interface states, oxide charge, ion transport through insulators and silicon impurity profile [12].

Figure 5.12(a) and (b) show the small signal (10 mV) capacitance as a function of bias voltage in the range −10 to +10 volts. The frequency of the applied ac signal was respectively 100 Hz and 10 kHz. The figures show good C-V characteristic behaviour, with clear indications of the regions of accumulation, depletion and inversion. The accumulation was observed during negative bias since the film has been deposited on p-type silicon (resistivity 10Ω -cm). At accumulation the total capacitance is only due to the insulating film and hence the structure resembles an MIM structure. Thus the dielectric constant of the insulator is calculated from the formula,

$$C_{max} = \frac{\epsilon_o \epsilon_r A}{d} \tag{5.9}$$

The maximum value of dielectric constant of amorphous $BaTiO_3$ thin film of thickness 140 nm was calculated as 16.12 at accumulation. As the bias on the gate electrode (top Al electrode) is increased from negative to positive, the majority carriers (holes) are depleted from the insulator semiconductor interface to form a depletion region. This depletion region acting as a series capacitance with the insulator results in the reduction of effective capacitance. The flat band capacitance C_{FB} of the film

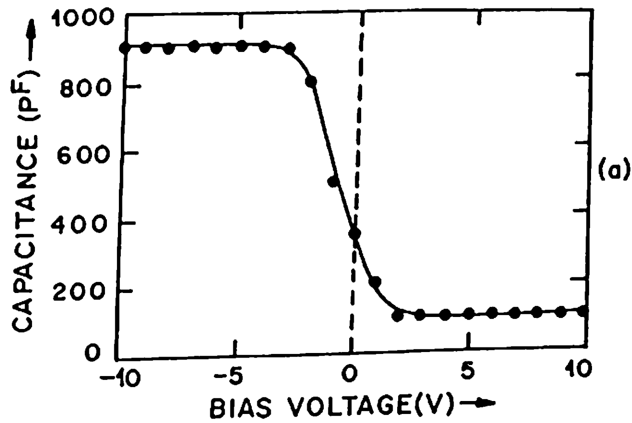

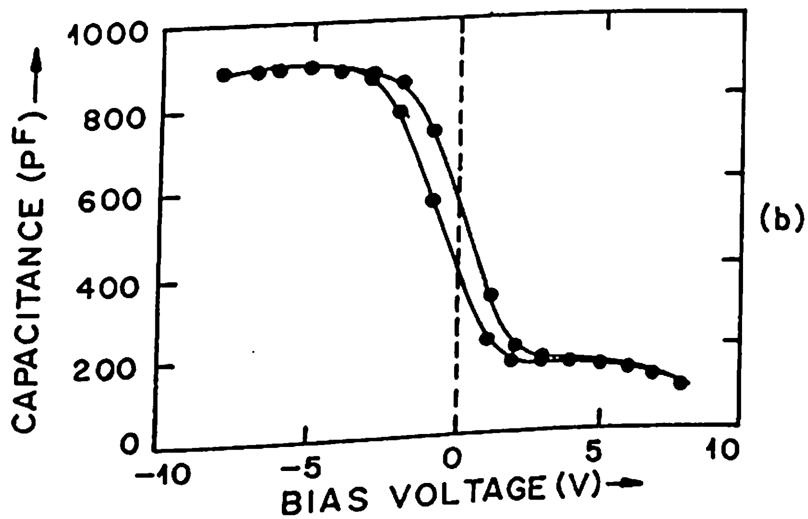

Figure 5.12: C-V characteristics of MIS capacitor based on amorphous $BaTiO_3$ thin film measured at a signal frequency of (a) 100 Hz and (b) 10 kHz respectively.

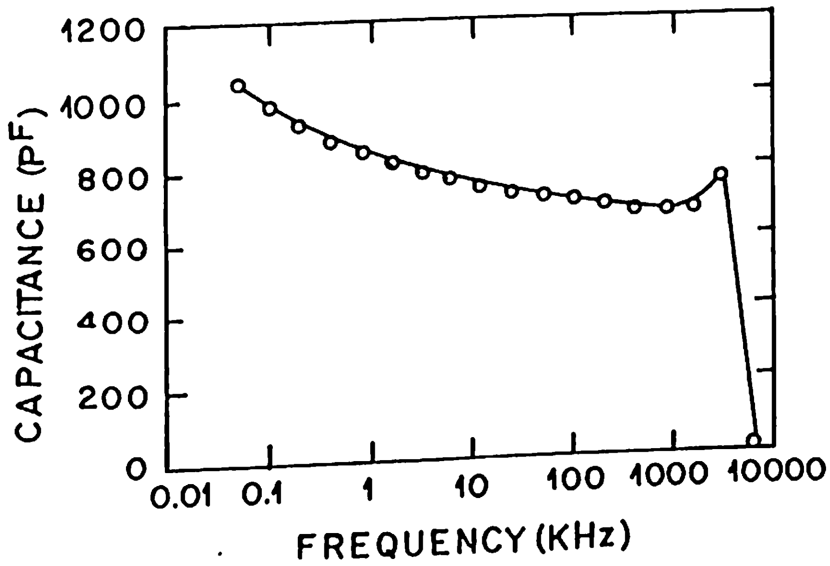

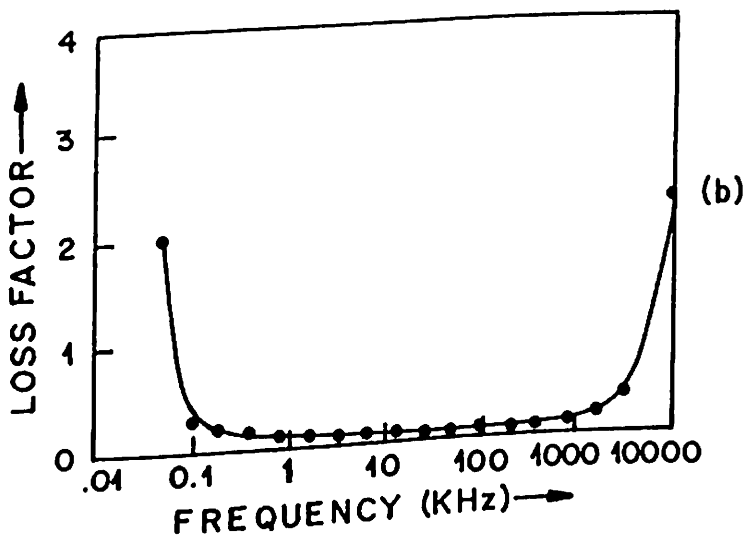

Figure 5.13: Dielectric dispersion in amorphous $BaTiO_3$ thin film (a) variation of capacitance with frequency and (b) variation of loss factor with frequency.

was calculated from the relation [13]

$$C_{FB} = \frac{\epsilon_o \epsilon_r A}{d + \frac{\epsilon_r/\epsilon_s}{L_d}} \tag{5.10}$$

where ϵ_r is the dielectric constant of the insulator and ϵ_s is the dielectric constant of the semiconductor. A is the area of the capacitor and d is the thickness. L_d the extrinsic Debye length is calculated using the relation

$$L_d = (\frac{kT\epsilon_s}{q^2 N_D})^{1/2} \tag{5.11}$$

where N_D is the donor concentration of the p-types semiconductor, k the Boltzman's constant, q the electronic charge and T the absolute temperature. The value of L_d calculated for P-type silicon of resistivity 10 Ω -cm was about 90 nm. Using this value the flat band capacitance obtained for a 1400 nm amorphous $BaTiO_3$ thin film at a signal frequency of 100 Hz was about 410 pF and corresponding flat band voltage was −0.5 volt. This negative voltage shift indicates the presence of positive traps state in the insulator.

The C-V measurements at different frequencies suggested a dispersion in the capacitance with frequency for these films. The frequency dependence of capacitance and dielectric loss are indicated in figure 5.13(a) and (b). The figure indicates that there is no appreciable dispersion in capacitance in the frequency range 500 Hz to 1 MHz. The dielectric loss factor also shows very small variation in this frequency range. The existence of hysteresis behaviour in the C-V curve plotted at 10 kHz when dc bias is swept from accumulation to inversion and back to accumulation indicate charge carrier injection in to the film from the electrode. The hysteresis voltage width (ΔV) measured was about 0.3 volts. The density ofstates recharged during the bias cycle in the C-V measurement, N_{it} calculated using the relation,

$$N_{it} = \frac{C_i \Delta V}{qA} \tag{5.12}$$

was about $1.8\times 10^{11}/cm^2$, where C_i is the insulator capacitance. Similar values were reported for MOS devices with conventional insulators.

The total oxide trap charge density in an insulating film is related to the flat band voltage V_{FB} and the work function difference between the gate electrode mate-

rial and the semiconductor by the following relation,

$$Q_i = (\Phi_m - V_{FB})C_i \tag{5.13}$$

which was calculated as $3.5\times 10^{11}/cm^2$. When the negative bias on the gate electrode changes to positive value, the majority carriers (holes in the case of p-type semiconductor) are depleted away from the semiconductor-insulator interface, thereby causing a series capacitance to the insulating film. This causes a reduction in the effective capacitance. This depletion of majority carriers disturb the equilibrium concentration of charge carriers in the semiconductor. The maximum width of this depletion region W_m is thus determined by the dopant concentration in the semiconductor. Hence the value of the capacitance minimum C_min is related to the maximum depletion width as

$$C_{min} = \frac{\epsilon_o \epsilon_r A}{d + \frac{\epsilon_r}{\epsilon_s} W_m} \tag{5.14}$$

From the semiconductor data the value of W_m calculated was about 600 nm. Using this value of W_m, the value of C_{min} calculated for a film of thickness 140 nm was about 110 pF. The value of C_{min} measured from the C-V characteristics was 105 pF.

During inversion, the depletion capacitance C_d acting in series with the dielectric effects in reduction of total capacitance and hence the following relation holds true.

$$\frac{1}{C_{min}} = \frac{1}{C_{max}} + \frac{1}{C_d} \tag{5.15}$$

Using the value of C_{min} and C_{max} in the above relation, the value of the depletion capacitance is obtained as 112 pF. The value of C_d calculated theoretically from the relation

$$C_d = \frac{\epsilon_o \epsilon_s A}{d} \tag{5.16}$$

was 129 pF. The proximity in calculated and measured values of these quantities indicate the good dielectric behaviour of the amorphous $BaTiO_3$ thin films, which can be successfully utilized for the fabrication of charge storage devices.

5.2.2 I-V characteristics

The details of the I-V measurements were given in the experimental section. The samples used were MIS capacitors with amorphous $BaTiO_3$ thin films as dielectric

on p-type silicon wafers. A dc bias of 20 V has been applied to the sample in forward bias (positive potential to the gate electrode) and reverse bias (negative potential to the gate electrode). Figure 5.14 shows the I-V characteristics of the above sample configuration for insulating films of thickness 140 nm and 280 nm. The leakage current in the samples are in the order of nanoamperes indicating their good insulating behaviour. The current in the forward bias is dependent on the sample thickness as seen from the figure 5.14. At the same time, for both films the current in the reverse bias is about 2 order of magnitude less than that in the forward bias. The I-V characteristics shown in the figure 5.15 have similar behavior to that of conventional MOS structure [14].

The conduction mechanism in insulating thin films are intrinsically related to the density of charged defect states in the material. The negative shift in the flat band voltage in the measured C-V characteristics suggests the presence of positively charged trap states in the insulator. For such material having a high density of positively charged traps, a conduction mechanism of Poole-Frenkel type is suggested [15]. To understand conduction mechanism in these thin films, a curve has been plotted between $V^{1/2}$ and ln(I/V) in figure 5.15. The slope of the curve measured from the above graph was about 1.24.

The relation governing the Poole-Frenkel type of conduction mechanism in materials with intrinsic defects is given as

$$J = E \exp \left[\frac{-q(\Phi_B - \sqrt{qE/\pi\epsilon_o\epsilon_r})}{kT} \right] \tag{5.17}$$

This relation can be modified as,

$$log(I/V) = \frac{-q}{kT}\sqrt{\frac{qV}{\pi\epsilon_o\epsilon_r d}} + \text{constant} \tag{5.18}$$

where ϵ_r is the dielectric constant and d the thickness of the film. The value of dielectric constant calculated using the above relation by substituting the value of the measured slope from the figure 5.16 was about 19.96. This value is in good agreement with the value of dielectric constant calculated from the C-V measurements for an applied signal of 100 Hz.Generally for the above calculation the static dielectric constant has to be used. We assume here that the value of dielectric constant measured at a frequency of 100 Hz can be considered same as static dielectric constant.

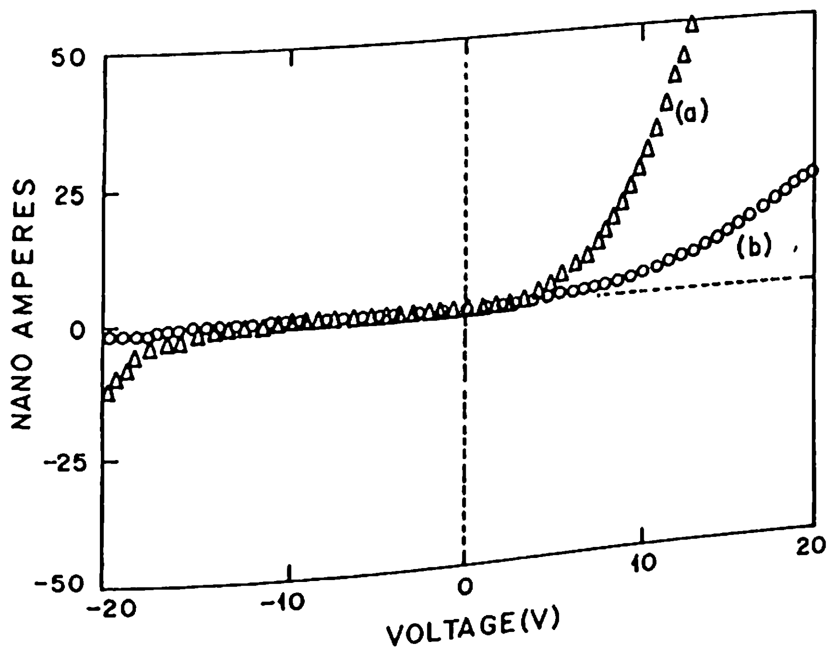

Figure 5.14: V-I characteristics of amorphous $BaTiO_3$ on silicon substrate for different thicknesses (a) 140 nm and (b) 280 nm.

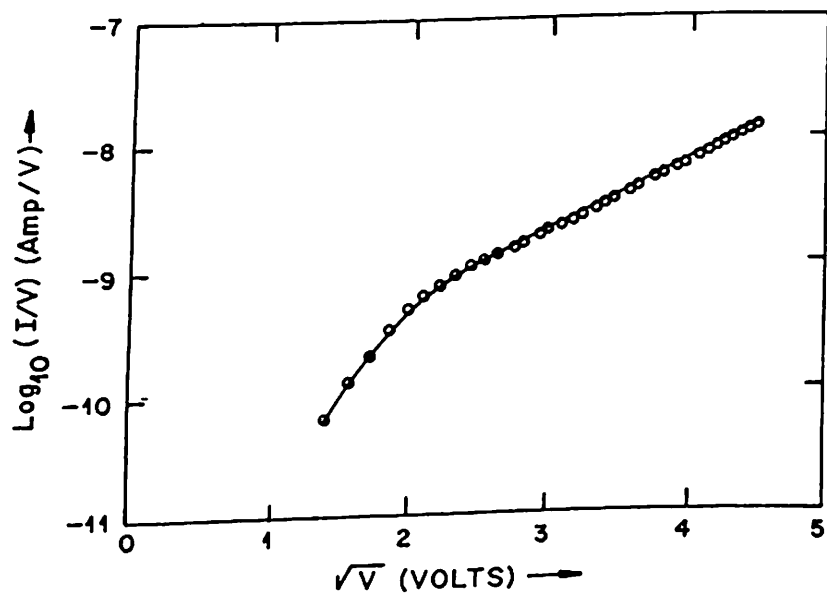

Figure 5.15: Plot representing Poole-Frenkel conduction mechanism.

The results obtained in the C-V and I-V measurements support the fact that, amorphous $BaTiO_3$ thin films are potential candidates as insulators in developing memory capacitors having high charge storage density and low leakage current density.

5.3 Ferroelectric Properties of $BaTiO_3$ Films

One of the best known features of ferroelectric materials is the response of the polarization P with external electric field E, which is often referred to as simply the hysteresis. Ferroelectric behaviour in a material can be confirmed by observations this hysteresis in P-E response on an oscilloscope. Another method is to observe the non-linear behaviour in dielectric response under voltage bias, often referred to as butterfly loop.

5.3.1 P-E Hysteresis loop measurements

P-E measurements were done using the well known Sawyer-Tower circuit, for $BaTiO_3$ samples made on platinized silicon wafers. Figure5.16 shows the PE hysteresis loop of 2.5μm thick $BaTiO_3$ thin films under humid free conditions, without any compensation. The remanent polarization P_r measured to 8μC/cm^2 and coercive field E_c was 35 kV/cm. The saturation ends of the hysteresis loops are not well pointed. This happens because, thin films generally exhibit high electric conductance and dielectric losses. This demands, the compensation for residual capacitance and conductance of the sample. This is done by introducing compensation network as given in the modified hysteresis loop tracer illustrated in experimental section [16].

Figure 5.17 shows the compensated hysteresis loop for $BaTiO_3$ thin films measured under dry conditions. the block diagram of the hysteresis loop tracer with compensation is given in the experimental section. It is observed that with compensation the edges become more sharper than the compensated loops. A reduction in coercive field has been observed in the compensated samples.

The effect of applied electric field on P-E hysteresis loop is shown in figure5.18. As the applied field increases, ferroelectric domain began to grow, remitting in a

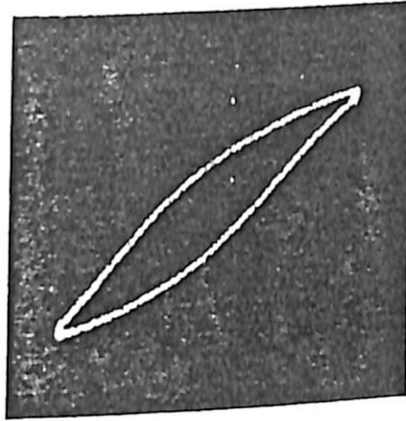

Figure 5.16: P-E hysteresis loop for $BaTiO_3$ thin film on Pt:Si substrate without compensation.

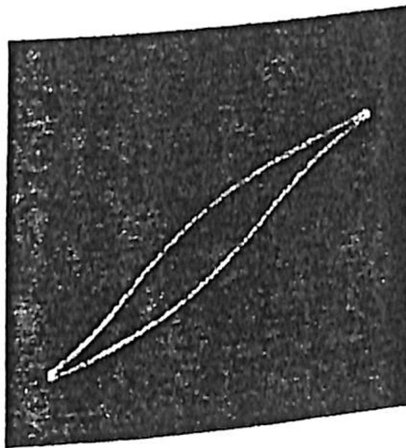

Figure 5.17: P-E hysteresis loop for $BaTiO_3$ thin film on Pt:Si substrate with compensation.

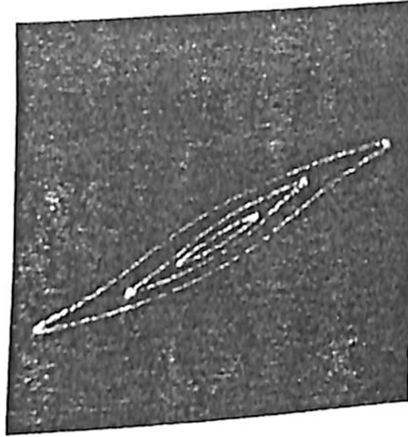

Figure 5.18: P-E hysteresis loop for $BaTiO_3$ thin film on Pt:Si substrate with compensation at different fields.

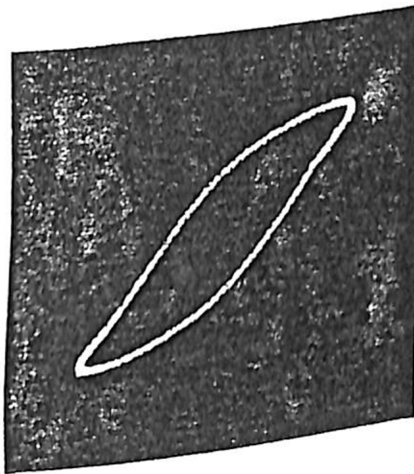

Figure 5.19: P-E hysteresis loop for $BaTiO_3$ thin film on Pt:Si substrate without compensation under humid conditions.

spontaneous polarization, which saturates at higher field. The increase in area of the loop indicates that the hysteresis loss increases with increasing value of electric field [17]. This loss arises due to the domain wall motion.

The effect of moisture on the hysteresis behaviour of $BaTiO_3$ thin films, were observed by carrying out P-E hysteresis measurements under humid conditions. Figure 5.19 shows the hysteresis loops of the sample taken in humid conditions. The ends of the loops are more wide open suggesting an increased conductivity due to the presence of moisture in the measuring atmosphere. The pronounced conductivity of $BaTiO_3$ under humid conditions are confirmed from the dielectric measurements explained earlier. The area of the loop also increased under this measurement conditions.

5.3.2 C-V butterfly loop

Further, the evidence of ferroelectricity has been established in sol-gel derived $BaTiO_3$ thin films from C-V measurements carried out on films grown on Pt:Si. Figure 5.20 represents a typical C-V butterfly loop for a ferroelectric thin film [18]. The measurement was done by super imposing an ac signal of amplitude 1 volt and frequency 1 MHz with positive dc bias on $1\mu m$ thick film. The nature of C-V loop indicates, hysteresis and the non linear behaviour of ferroelectric $BaTiO_3$ with applied bias.

Figure 5.21(a), (b) and (c) are the C-V hysteresis loop plotted for a $2.5\mu m$ thick $BaTiO_3$ film for frequencies 10 KHz, 100 KHz and 1 MHz respectively.

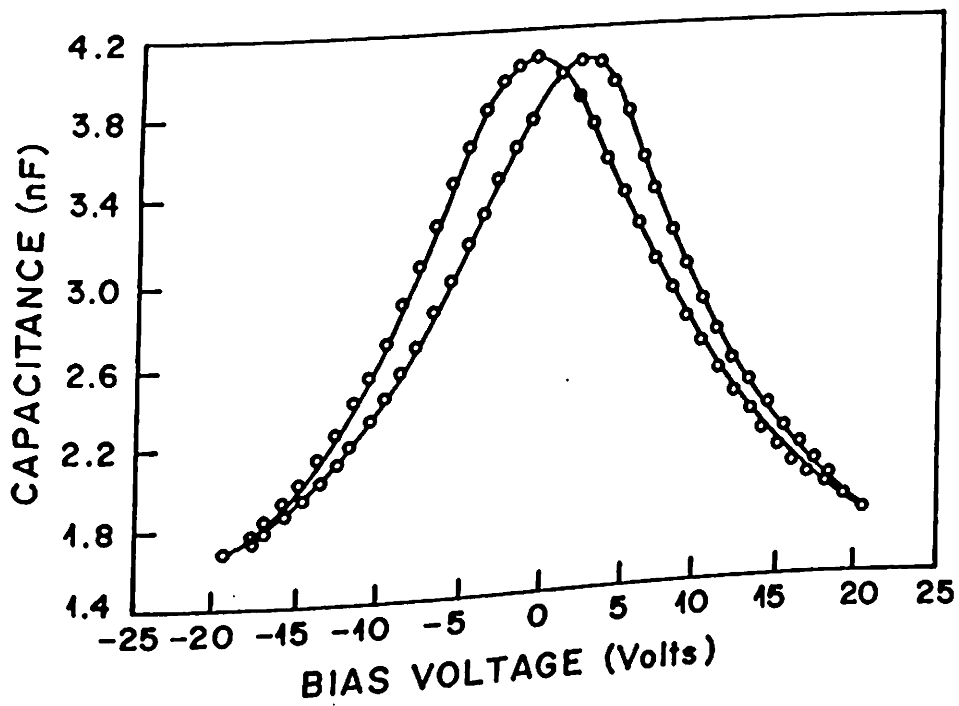

Figure 5.20: C-V butterfly loop for a 1μm $BaTiO_3$ thin film on Pt:Si substrate at 1 MHz.

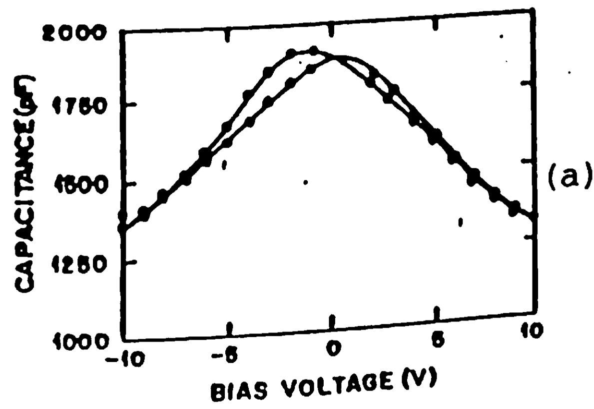

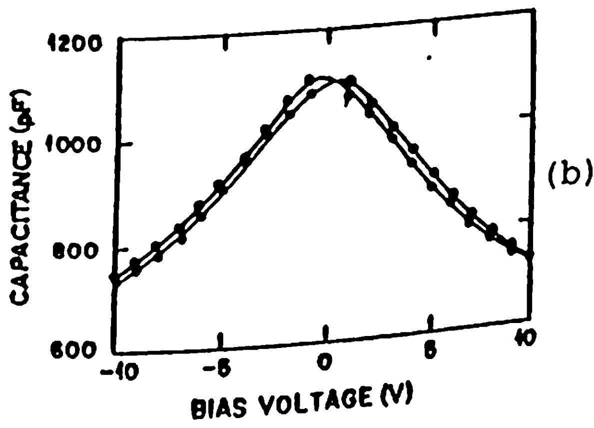

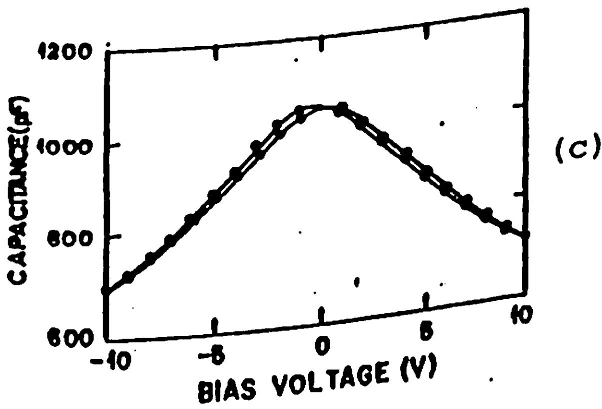

Figure 5.21: C-V characteristics of a 2.5μm $BaTiO_3$ thin film on Pt substrate at (a) 10 kHz, (b) 100 kHz and (c) 1 MHz.

References

1. K.H.Hardtl. Ferroelectrics. 12, 9 (1976).
2. A.J.Mountvala. J.Am.Ceram.Soc., 54, 544 (1971).
3. M.I.Yanovskaya, N.Ya Turova, E.P.Turevskaya, A.V. Novoselova, Y.N. *Venevtsev*, S.I. Segitov and E.M. Soboleva, Inorg. mater. 17, 221(1981).
4. N.D.S.Mohallem. Ph.D.thesis, Univ.Sao Paulo (1990).
5. T. Tuchiya, T. Kawano, T.Sei and H.Hatano, J. Ceram. Soc. Jpn. 98, 743(1990).
6. A.I. Lakatos and M. Abkowitz, Phys.Rev., B3, 1791 (1971).
7. M. Kitao, Jpn.J.Appl.Phys.11, 1472 (1972).
8. M.Pollak, Philos. Mag. 23, 519 (1971).
9. Q. X. jia, Z. Q. Shi and W. A. Anderson, Thin Solid Films 209, 230 (992).
10. J. D. McClure and J. R. Crow, J. Vac. Sci. Technol. 16, 311 (1979).
11. K. Sreenivas and A. Mansingh, J. Appl. Phys. 62, 4475 (1987).
12. E. H. Nichollian and J. R. Brews, *Metal Oxide Semiconductor Physics and Technology*, (Wiley, New York. 1970).
13. S. M. Zee, *Physics of Semiconductor Devices*, (Wiley, New York, 1991).
14. G. Q. Lo, D. L. Kwang and S. Lee, Appl. Phys. Lett. 60, 3236 (1992).
15. A. K. Jonscher and R. M. Hill, *Physics of Thins*, ed. George Hass (Academic, New york, 1975), vol 8, pp. 222.
16. C. B. Sawyer and C. H. Tower, Phys. Rev. 35, 269(1930).
17. Shaoping Li, Wenwu Cao, and L. E. Cross, J. Appl. Phys. 69(10), 7219(1991).
18. D. R. Uhlmann, G. Towee, and J. M. Boulton, J. Non-Cryst. Solids 131-133, 1194(1991).

Chapter 6

Dielectric and Electrical Properties of Sol-Gel Derived $SrTiO_3$ Thin Films

Sol-gel derived thin films are very attractive candidates for a variety of new applications in microelectronics and integrated optics. The ceramic thin films fabricated using this technique find applications in high density random access memory devices [1,2] and electro-optic devices [3]. Strontium titanate is a well known perovskite structured material which has a cubic paraelectric phase above 105K. It has a bulk dielectric constant of about 300 [4] which is nearly temperature independent and therefore can achieve a reasonable charge storage density for high density memory applications. Further, $SrTiO_3$ thin films are chemically and compositionally very stable and have excellent dielectric properties which make it an excellent insulator for electronic applications.

6.1 M-I-M Capacitor Structure based on polycrystalline $SrTiO_3$ thin films on stainless steel substrates

The quality of a dielectric material for their application in capacitor technology and other charge storage devices are generally evaluated in terms of its frequency response and their ability to retain stored charges. For this purpose the dielectric and electrical behaviour of the material has to be investigated. Strontium titanate ceramic thin

films are emerging as an excellent candidate for the above applications. Here the electrical and dielectric properties of strontium titanate thin films made by sol-gel process are studied on samples made on stainless steel substrate. The top electrode of the configuration was vacuum evaporated gold dots of diameter 1mm.

6.1.1 Dielectric Properties

The electrical conductivity of dielectric thin films is usually influenced by the nature of electrical contacts through which the electrical properties are measured. It is therefore necessary to ensure that the electrical contacts are ohmic and there is no spurious capacitance due to surface barriers at the electrodes. The measured capacitance C_{meas} of a metal-insulator-metal (MIM) structure in the presence of an electrode barrier can be expressed as [5]

$$C_{meas} = (\epsilon_o \epsilon_r A)(1/d) + C_s \qquad (6.1)$$

where A is the area, d the thickness, ϵ' the dielectric constant of the sample, ϵ_o the permittivity of vacuum and C_s the surface barrier capacitance. If C_s , is negligible then the value of the dielectric constant measured will be independent of thickness and if C_s is significant, the measured dielectric constant should increase with increase in thickness. In figure 6.1 the measured value of dielectric constant ϵ' is plotted against the sample thickness for various frequencies. It is seen that ϵ' is nearly thickness independent showing that the barrier capacitance is negligible and the measured value ϵ' represents the bulk values of $SrTiO_3$ thin films. Since the dielectric properties are thickness independent, for all further measurements, samples having 1.4μm thickness were used.

Figure 6.2 shows variation of dielectric constant ϵ' and loss factor $\tan\delta$ with frequency at temperatures 305, 396, 445 and 500K. The dielectric constant ϵ' shows a decrease with increase in frequency upto 10^6 Hz for all measured temperature. Above 10^6 Hz, it increased with further increase in frequency. The loss factor $\tan\delta$ shows a broad peak at room temperature centered around 25 KHz. At higher temperatures the low frequency part of $\tan\delta$ shows an increase presumably due to the increase in the number of free carriers thermally generated. The $\tan\delta$ peak is also not distin-

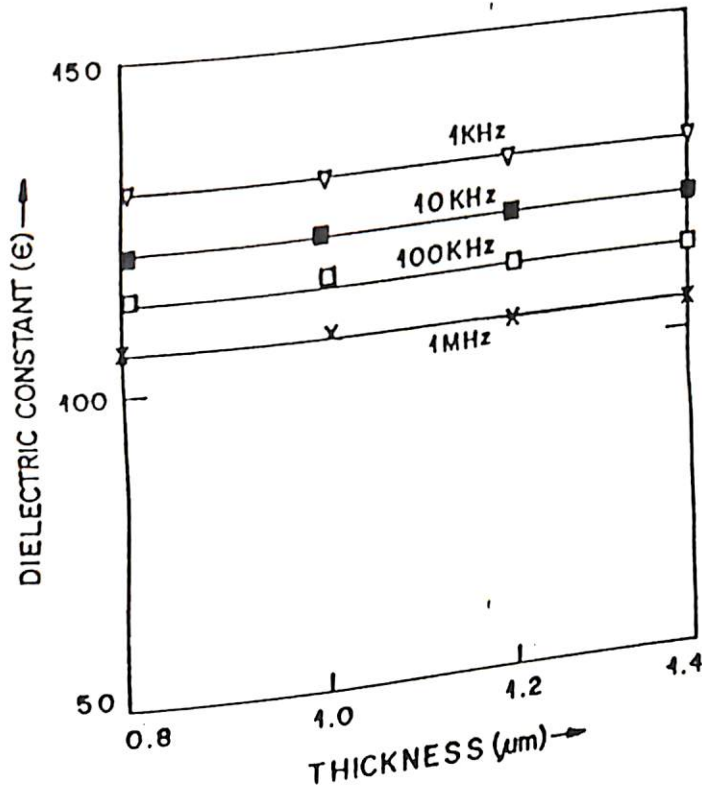

Figure 6.1: Variation of dielectric constant of $SrTiO_3$ thin film on stainless steel substrate with thickness for different frequencies.

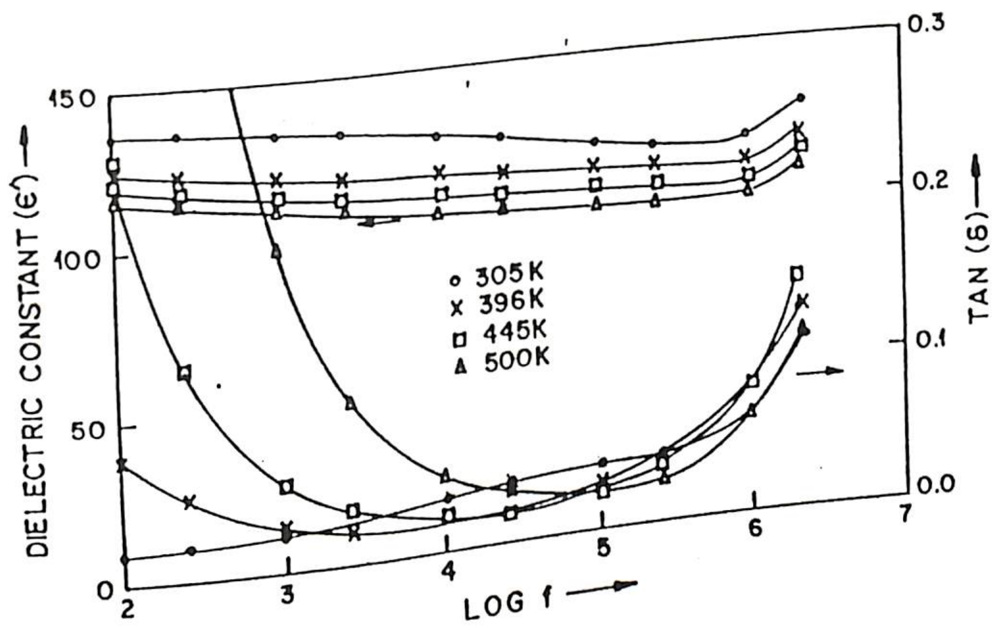

Figure 6.2: Variation of ϵ' and $\tan\delta$ with frequency for $SrTiO_3$ thin film on stainless steel substrate.

guishable at higher temperatures. At higher frequencies, tan δ increases with increase in temperature.

Figure 6.3 shows variation of ϵ' and tan δ with temperature for frequencies 100 Hz, 1,10 and 100 kHz, and 1 MHz. It is seen that ϵ' decreases with increase in temperature for all measured frequencies, whereas tan δ shows a different nature at various frequencies. At low frequencies it increases continuously with an increase in temperature, whereas at higher frequencies it shows relaxation peaks with the peak positions shifting towards higher temperature region with increase in frequency.

Figure 6.4 shows variation of dielectric loss ϵ'' with temperature. ϵ'' shows broad peaks, the positions of which shift toward higher temperature as frequency is increased. For a Debye type relaxation

$$\epsilon''(\omega) = (\epsilon_s - \epsilon_{ea})\frac{\omega\tau}{1 + \omega^2\tau^2} \qquad (6.2)$$

where ϵ_s is the static dielectric constant, ϵ_{ea} is the instantaneous value of the dielectric constant, and τ is the relaxation time. It is observed that the dielectric loss exhibits a maximum for $\omega\tau = 1$; i.e., for an angular frequency equal to $\frac{1}{\tau}$. From the observed curves, the relaxation time τ at different temperatures are determined, which is related to the activation energy E_a as

$$\tau(T) = \tau_o \exp(E_a/kT) \qquad (6.3)$$

where τ_o is a constant. Figure 6.5 shows the plot of logτ(T) versus 1000/T, from the slope of which an activation energy $E_a = 0.38$ eV has been obtained.

6.1.2 Frequency dependence of conductivity

Figure 6.6 shows the dependence of ac conductivity σ_ω of the sample with frequency. At room temperature, the plot is a straight line with a slope of 1.13, whereas at higher temperatures, σ_ω shows frequency independent conductivity at low frequencies and a superlinear dependence at higher frequencies. The slope of the curves at higher frequencies was found to increase with increase in temperature.

The temperature dependence of conductivity of $SrTiO_3$ thin films was measured in the range of 305 to 500K. The results obtained are shown in figure 6.7 where

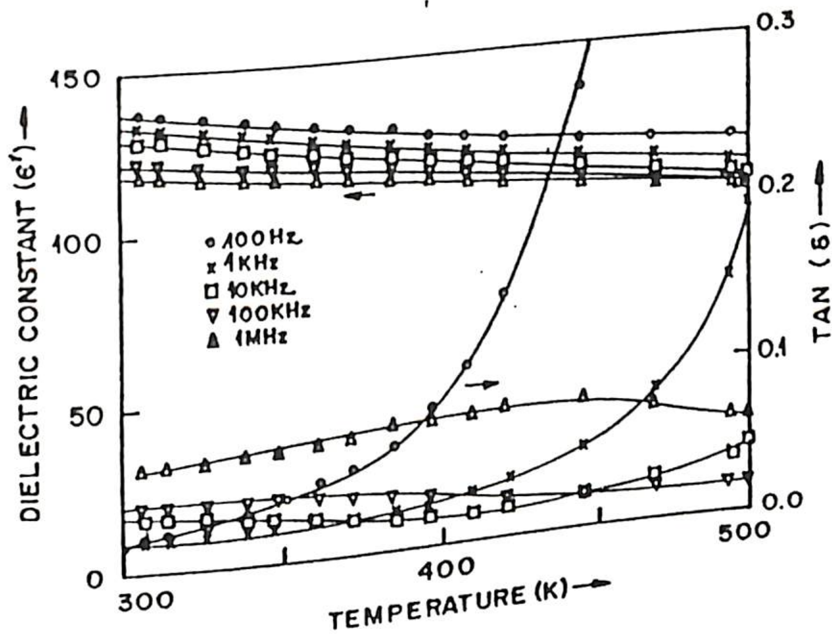

Figure 6.3: Variation of ϵ' and $\tan\delta$ for $SrTiO_3$ thin film on stainless steel substrate with temperature at various frequencies.

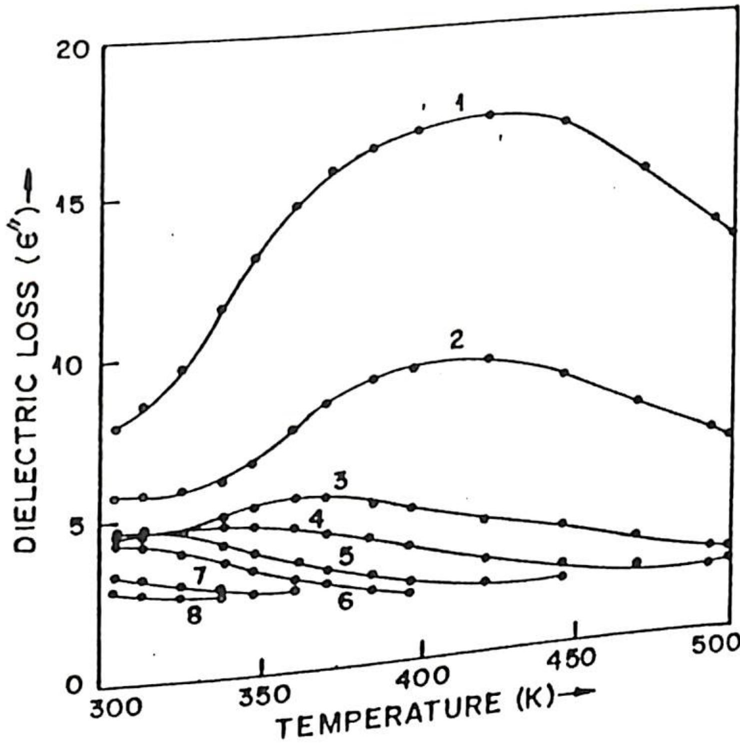

Figure 6.4: Variation of ϵ'' with temperature at various frequencies (1) 2 MHz. (2) 1 MHz. (3) 250 kHz. (4) 100 kHz. (5) 25 kHz. (6) 10 kHz. (7) 2.5 kHz and (8) 1 kHz.

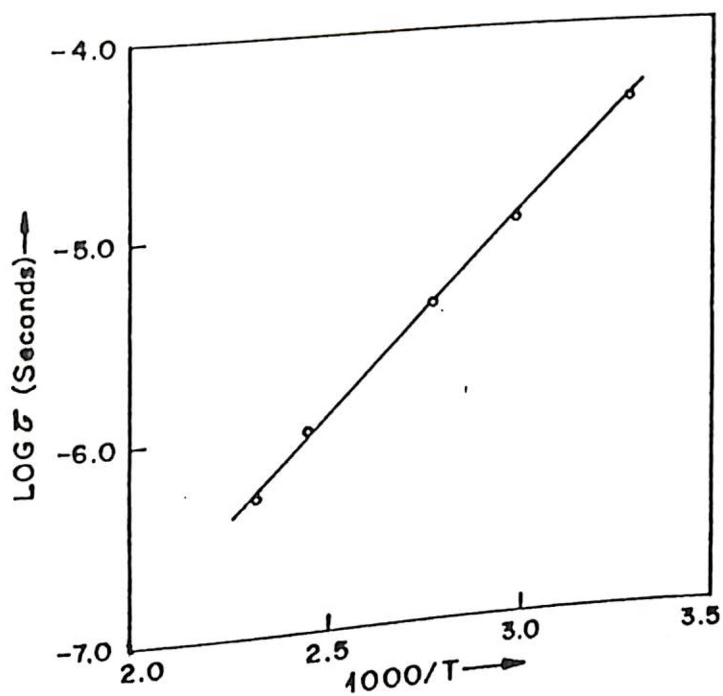

Figure 6.5: Relaxation time as a function of temperature.

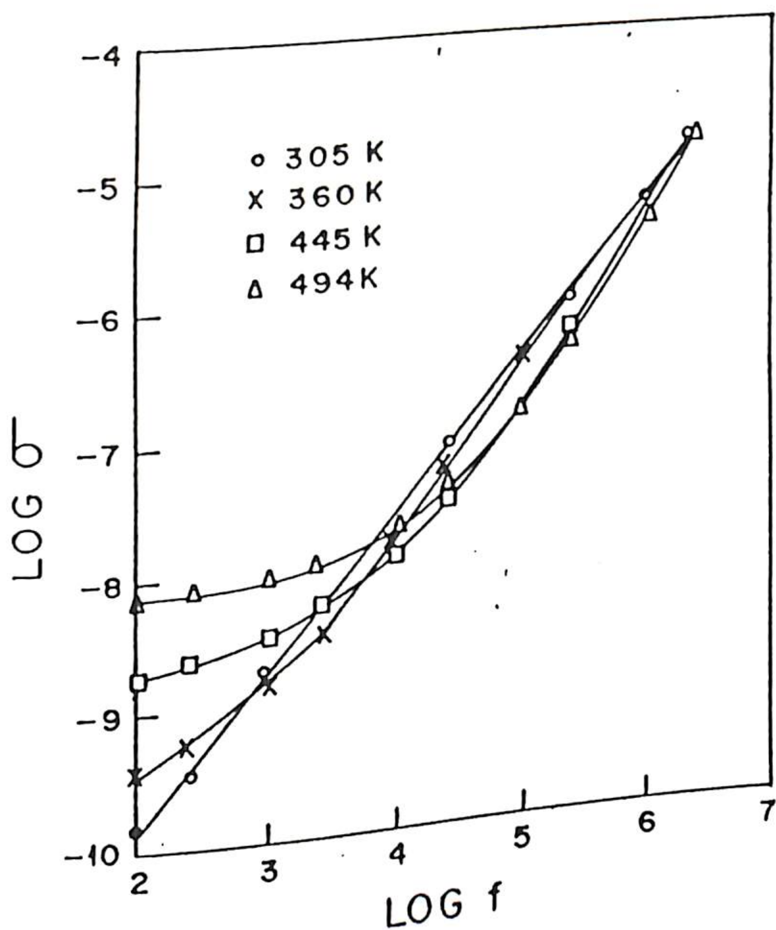

Figure 6.6: Variation of conductivity as a function of frequency.

$\log\sigma_{meas}$ is plotted as a function of 1000/T for different frequencies. As the temperature is increased, the ac conductivity approaches the dc conductivity asymptotically for all frequencies. Therefore, the frequency dependence decreases with increasing temperature. The activation energies for dc conduction were calculated from the straight portion of the plot showing $\log\sigma_{dc}$ versus 1000/T. The plot shows two slopes. The low temperature and high temperature parts give activation energies of 0.33 and 0.90 eV, respectively. Activation energy at high temperature, i.e., 0.90 eV is within experimental error to that of quenched single crystals of $SrTiO_3$ [6] i.e., 0.86 eV, and hence can be attributed to the crystalline phase of the thin film. $SrTiO_3$ single crystals do not show any activation energy values corresponding to 0.33 eV, but it is within the experimental error to that obtained for the relaxation peak (0.38 eV) considering that the relaxation peaks are broad. Therefore it is likely that room temperature resistivity as well as relaxation phenomenon are of the same origin and are due to the trapped carriers at the intercrystalline region.

6.1.3 C-V Characteristics

The capacitance of the sample was measured against dc bias (C-V) at 100 kHz and is shown in figure 6.8. The capacitance shows little variation with applied bias, and there was no hysteresis when the bias voltage was swept from positive to negative and back to positive voltage. The bias voltage independence of measured capacitance and the absence of hysteresis in the MIM structure reflect the pure paraelectric behaviour of the $SrTiO_3$ thin films at room temperature.

6.2 Conduction Mechanism in sol-gel processed $SrTiO_3$ Thin Films

It has been observed that the electrical conductivity of a dielectric thin film involving amorphous and crystalline phases may be expressed as the sum of a dc conductivity σ_{dc} and an ac conductivity σ_ω

$$\sigma_{meas} = \sigma_{dc} + \sigma_{ac} \tag{6.4}$$

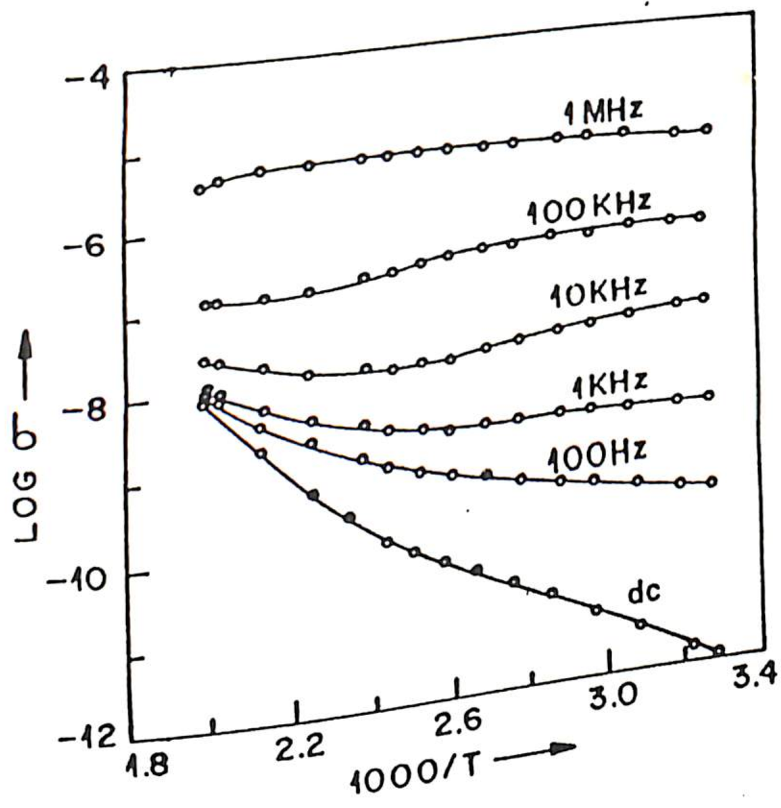

Figure 6.7: Variation of conductivity as a function of temperature.

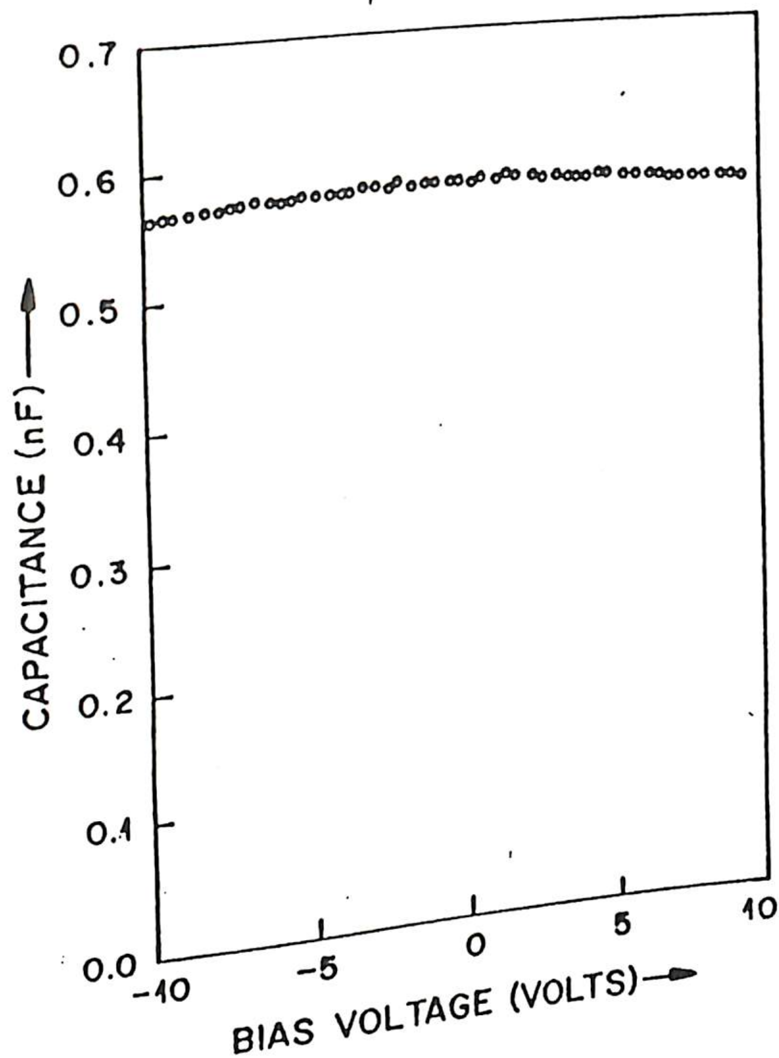

Figure 6.8: C-V characteristics of $SrTiO_3$ thin film on stainless substrate in MIM configuration.

The conductivity due to free carriers can be expressed as [7]

$$\sigma = \sigma_{dc} \frac{1}{1 + \omega^2 \tau^2} \qquad (6.5)$$

where ω is the frequency of the applied electric field and τ the relaxation time. Therefore the conductivity due to free carriers decreases with increase in frequency. In the present case, figure 6.6 shows that the conductivity increases with increase in frequency and therefore it can be inferred that the frequency dependent ac conductivity observed is due to bound carriers present in the sample.

The frequency dependent ac conductivity in $SrTiO_3$ thin films in the temperature range of 300-500K can conceivably be influenced by the following processes.

1. Schottky barrier at the metal dielectric interface
2. Hopping type conduction between localized states
3. Maxwell-Wagner-type dispersion due to inhomogeneities existent in the material, giving rise to a spatial variation of conductivity.

The presence of any appreciable metal dielectric barrier has not been detected at the metal dielectric interface, as seen from the thickness independent nature of the dielectric constant. (figure 6.1)

In dielectric materials which contain both amorphous as well as crystalline phases, there may be a large number of defect states in the band gap of the material due to impurities, imperfections, etc. The charge carriers in such a dielectric can hop from one localized state to another with the assistance of phonons. The frequency dependent conductivity in this case can be represented as

$$\sigma = A\omega^s \qquad (6.6)$$

Where A is a constant and s has a value of $0.8 < s < 1$ for randomly distributed hopping states and $s = 2$ for equivalent pair. Further, in case of randomly distributed pairs, s is slightly temperature dependent (s increases as temperature is decreased) [5] whereas the value of s is temperature independent in the case of equivalent pairs. In our investigations we found that the value of s at room temperature as 1.13, which

increased with increase in temperature. Hence the result is difficult to explain on the basis of hopping conduction.

The inhomogeneous $SrTiO_3$ thin films consisting of amorphous and crystalline phases will have regions differing in electrical conductivity which must give rise to frequency dispersion corresponding to Maxwell-Wagner (MW) type [7]. The sample can be considered as a series of homogeneous layers differing in electrical conductivity [figure 6.9(a)] and can be represented as a series of networks containing parallel connections of a resistor and a capacitor [figure 6.9(b)]. R_C and C_C are the resistance and capacitance of crystallite and R_A and C_A are the resistance and capacitance of the intercrystalline region connecting the crystallites. The parallel conductance G_P and the parallel capacitance C_P of such a network is given as,

$$G_p = \frac{R_C(1 + \omega^2 C_A^2 R_A^2) + R_A(1 + \omega^2 C_C^2 R_C^2)}{R_C^2(1 + \omega^2 C_A^2 R_A^2) + R_A^2(1 + \omega^2 C_C^2 R_C^2) + 2R_A R_C(1 + \omega^2 C_A C_C R_A R_C)} \quad (6.7)$$

and

$$C_p = \frac{C_C R_C^2(1 + \omega^2 C_A^2 R_A^2) + C_A R_A^2(1 + \omega^2 C_C^2 R_C^2)}{R_C^2(1 + \omega^2 C_A^2 R_A^2) + R_A^2(1 + \omega^2 C_C^2 R_C^2) + 2R_A R_C(1 + \omega^2 C_A C_C R_A R_C)} \quad (6.8)$$

If we take R_A to be a small but finite resistance, then at low frequencies the above network gives a constant value of conductivity and at higher frequencies an ω^2 dependence. The superlinear frequency dependence observed in the present case may be may be explained by considering the sample as a combination of large number of potential barriers having different barrier heights. This may give create different resistive regions.

The slight decrease in the measured ac conductivity with increase in temperature is due to the intercrystalline barrier relaxation effect. The ac conductivity of the sample shows maximum when the reciprocal of relaxation time ($\frac{1}{\tau}$) (which is determined by the temperature of the sample) is equal to the frequency of the applied field. Above this temperature the conductivity falls due to off resonance.

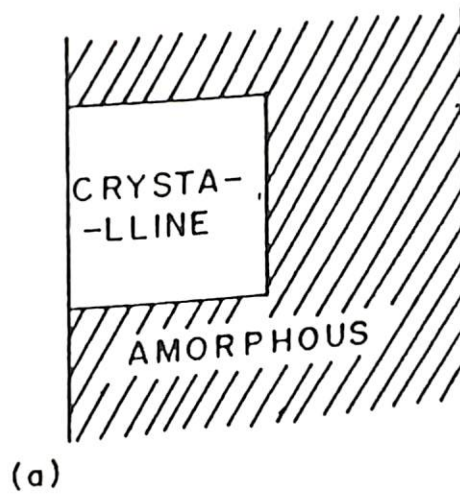

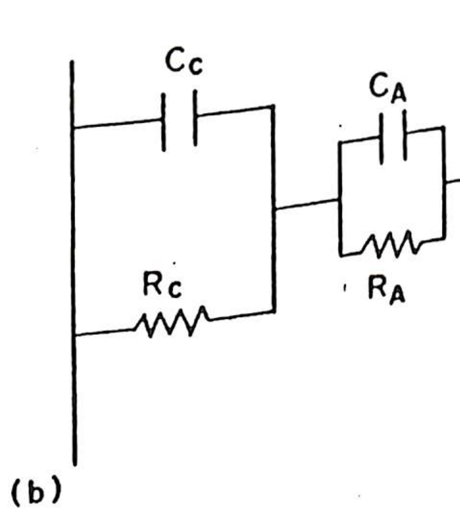

Figure 6.9: (a) Model of MIM capacitor based on $SrTiO_3$ thin film showing crystalline and amorphous regions and (b) equivalent network of crystalline regions and barriers.

6.3 MIS structure based on $SrTiO_3$ thin films on p-type silicon

The large dielectric constant and storage densities of ferroelectric thin films are highly valuable due to their suitability in developing DRAMs (dynamic random access memories) [8,9]. The dielectric constant of ferroelectric materials, in general, are many times larger than conventional gate dielectrics such as silicon dioxide and tantalum oxide. Their use as linear gate dielectrics, provides largely increased capacitance and offers the possibility to avoid trenching in submicron devices [1]. Strontium titanate is a ferroelctric exhibiting paraelectric phase at room temperature. It has a dielectric constant of about 300 [4] and can offer almost an order of magnitude higher capacitance density at relatively larger thickness, in a DRAM cell capacitor compared to other gate dielectrics such as silicon dioxide and tantalum oxide. $SrTiO_3$ has normally got a very small temperature coefficient of capacitance (figure 6.3), which makes them useful for operation in a wide range of temperatures. Due to the paraelectric phase of $SrTiO_3$ at room temperature, it is not affected by any mechanical stress (piezoelectric effect) as well. $SrTiO_3$ is compositionally very stable and hardly exist in any other phases under normal composition. These qualities make it very promising in memory applications.

6.3.1 C-V characteristics of $SrTiO_3$ thin films in MIS configuration

The figure 6.10 shows the typical C-V characteristics of $SrTiO_3$ thin film made in MIS configuration. The value of dielectric constant calculated from the curve for a film of thickness 200 nm was about 55. The anomalously low value of the dielectric constant observed in these films are due to their lower thickness [10]. For films of thickness more than 1 micron the dielectric constant approaches the bulk value. The plot shows a large negative flat band shift of 2.85 volts, as calculated from the value of flat band capacitance. This negative flat band shift indicates the presence of positive charged trap states existing in the film. The density of oxide trap states inside the film calculated using equation 5.13 (chapter 5) was about $10^{11}/cm^2$. The

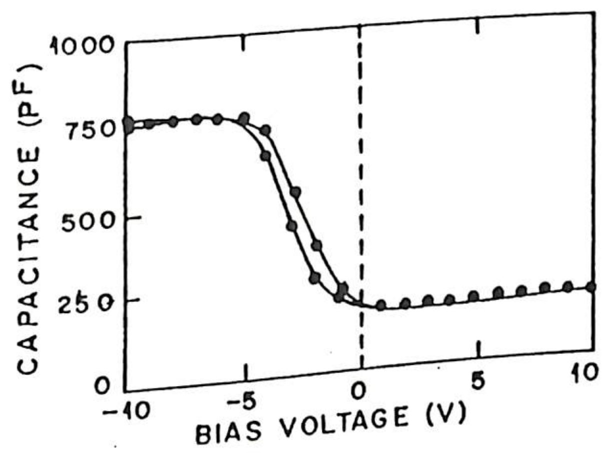

Figure 6.10: C-V characteristics of $SrTiO_3$ MIS thin film capacitor at a frequency of 10 kHz.

capacitance minimum measured from the C-V plot was 180 pF and the value of the same calculated using the equation 5.14 (chapter 5) was about 140 pF. The frequency dependence of dielectric constant and dielectric loss for $SrTiO_3$ thin films at a bias voltage of -5 V are shown in figure 6.11(a) and (b).

6.3.2 I-V characteristics

Figure 6.12 shows the I-V characteristics of $SrTiO_3$ thin film of thickness 200 nm. The leakage currents are of the order of microamperes, presumably due to the lower thickness of the films used. The large negative flat band voltage shift proposes a Poole-Frenkel type of conduction mechanism in these thin films [11]. To understand this, a graph has been plotted between $V^{1/2}$ and ln(I/V) as shown in figure 6.13. The slope of the straight line graph thus obtained was measured to be 0.936. The slope calculated from the relation representing the Poole-Frenkel conduction mechanism by substituting the value of dielectric constant calculated from the C-V characteristic was about 0.965. This indicates that the conduction mechanism in sol-gel derived $SrTiO_3$ thin films studied here can be satisfactorily explained on the basis of the Poole-Frenkel conduction mechanism.

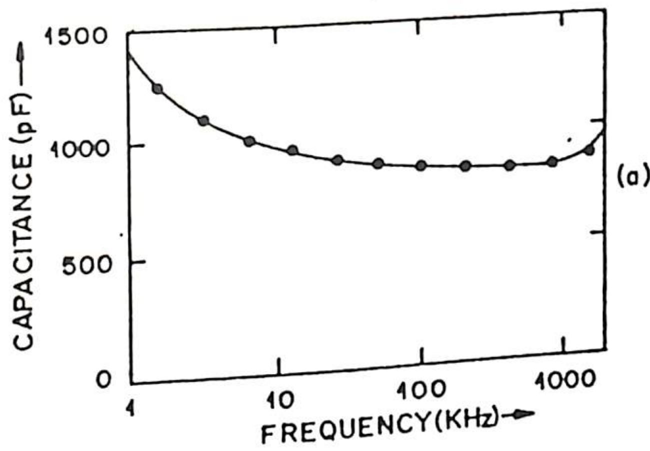

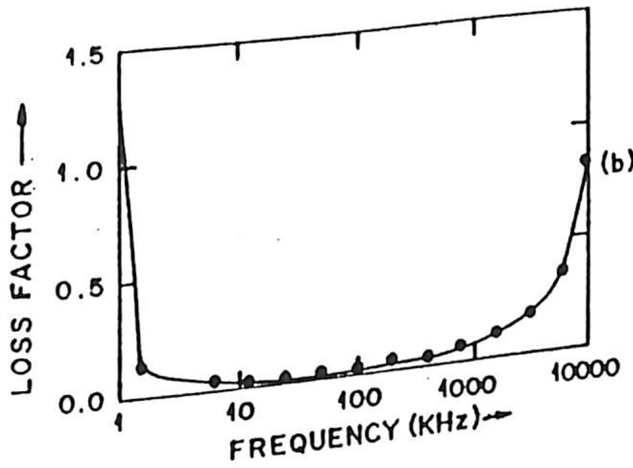

Figure 6.11: Dielectric dispersion in a $SrTiO_3$ MIS capacitor (a) variation of capacitance with frequency and (b) variation of loss factor with frequency.

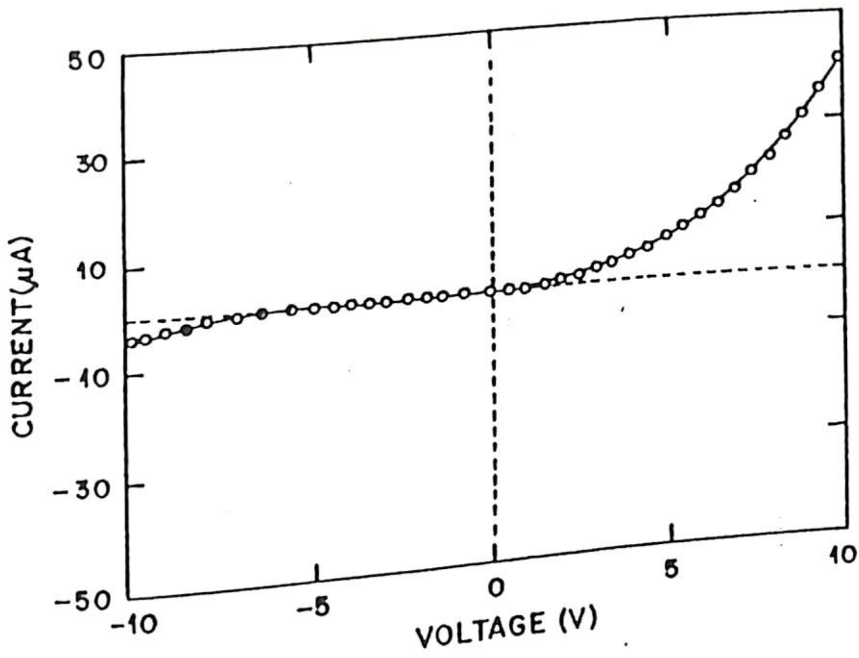

Figure 6.12: I-V characteristics of a 200 nm thick $SrTiO_3$ MIS capacitor.

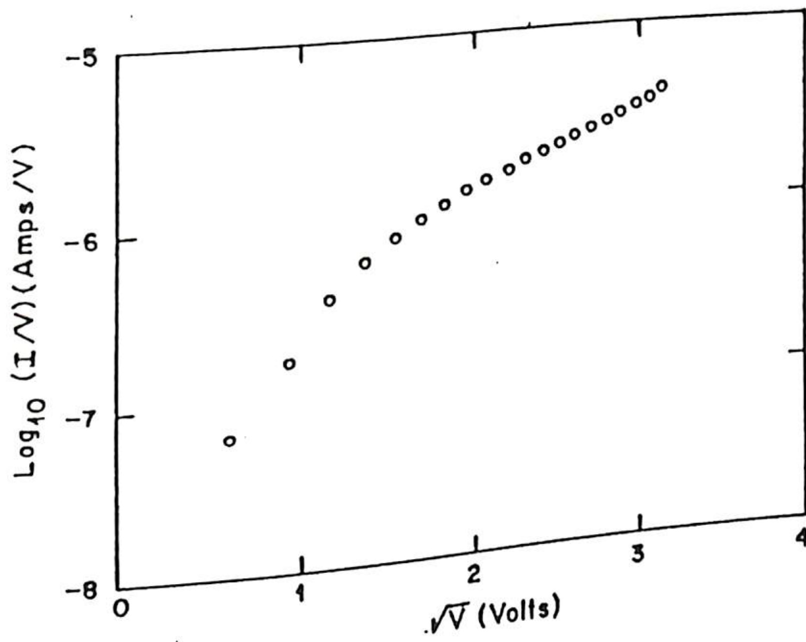

Figure 6.13: Curve representing Poole-Frenkel conduction mechanism in $SrTiO_3$ MIS capacitor.

References

1. L.H. Parker, A.F. Tassch, IEEE Circ. Dev. Mag. 17 (1990).
2. M. Sayer and K. Sreenivas, Science 247, 10056 (1990).
3. W. L. Warren, P. M. Lenanan, C. J. Brinker, C. S. Ashley, S. T. Reed, and G. R. Shaffer, J. Appl. Phys. 64, 4404 (1991).
4. J.A. Linz, Phys. Rev. 91,753 (1953).
5. A.I.Lakatos and M.Abkowitz, Phy.Rev.B3, 1791 (1971).
6. B. K. Choudhury, K. V. Rao, and R. P. N. Choudhury, J. Mater. Sci. 24, 3469 (1989).
7. M.Kitao,Jpn.J.Appl.Phys.11, 1472 (1972).
8. C.A. Araujo, L.D. McMillan, B.M. Melnick, J.D. Cuchiaro, and J.F. Scott, Ferroelectrics 104, 241 (1990).
9. Moazzami, C.Hu, and W.H.Shepherd, IEEE Electron Devices Lett. 11,454 (1990).
10. B.S. Krupanidhi and G. Mohan Rao, Thin Solid Films 249, 100 (1994).
11. A.K. Jonscher and R.M. Hill, in Physics of Thin Films, ed. Georg Hass (Academic, New York, 1975), Vol.8, P, 222.

Chapter 7

Conclusion

The feasibility of fabrication of multicomponent ceramic oxide thin films of $BaTiO_3$ and $SrTiO_3$ by sol-gel process are investigated in this work. Ferroelectric thin films of $BaTiO_3$ and $SrTiO_3$ has been deposited on varoius substrates using sol-gel process. These films are then characterized using different experimental techniques to optimize the growth properties. The sol-gel process being a chemical process, the nature of the final ceramic thin film can be largely depend on the selection of the starting materials and the preparation conditions. Therefore, these thin films are fabricated using different sets of starting materials. On the basis of the studies done on the samples made from different precursor combinations, the following conclusions are reached about the various physical, structural, and microstructural properties of sol-gel grown $BaTiO_3$ and $SrTiO_3$ ceramic thin films.

Thin films of barium titanate made from different precursors exhibit different properties, which revels that sol-gel process can be carefully manipulated to tailor different desired properties of these materials. The optical properties such as refractive index, optical transmission and thickness of the $BaTiO_3$ thin films made from different precursors can be varied largely,in fact this is useful when these optical properties have to be presicely controlled for certain applications. By the proper selection of precursors a desired crystalline phase can be achived for the same material under same processing conditions. Barium titanate thin films made from titanium isopropoxide and barium 2-ethyl hexanoate crystallized in to tetragonal phase (ferroelectric) on heating while the films made from titanium isopropoxide and barium 2-methoxyethoxide crystallized in to cubic phase. Cubic phase $BaTiO_3$ thin films

are supposed to have better long term stability than conventional tetragonal phase $BaTiO_3$ due to its higher symmetry. Cubic barium titanate suffer less aging effect and hence can retain its dielectric properties for longer duration without degradation.

The electrical and dielectric properties of sol-gel grown $BaTiO_3$ and $SrTiO_3$ thin films largely depend on the microstructure of the films and the nature of the electrodes used. Thin films of barium titanate made on stainless steel substrate has showed electrode barrier effect indicating the non-ohmic nature of the contact. Platinum substrates were found to ensure ohmic contact for these thin films. Electron microscopy observations showed the presence of a mixed amorphous and crystalline phase in these samples. The electrical equivalent modelled on the basis of the above observations could explain fiarly well the electrical and dielectric behaviour of the samples.

Barium titanate thin films made from titanium isopropoxide and barium 2-ehtyl hexanoate showed the ferroelectric behaviour indicating the formartion of tetragonal baruim titanate thin films. The nature of the hysteresis loop measured at ambient conditions were found to be different from that measured under humid free conditions. This observation again confirms the effect of humidity on the dielectric behaviour of $BaTiO_3$ thin films.

Finally, M-I-S capacitors made from amorphous $BaTiO_3$ and crystalline $SrTiO_3$ thin films as insulating layer are evaluated for their use in memory devices. Due to the high dielectric constant of these materials the storage density could be increased manyfold compare to devices based on conventional dielectrics. The leakage current measured for these films were also very small.

The work presented here, emphesize on the succesful fabrication of $BaTiO_3$ and $SrTiO_3$ thin films by sol-gel process. The tailoring of their properties are easly achieved by the proper selection of precursors and processing parameters.

Bio-Data

Born in Qulion, Kerala on 31st May 1967. Received M.Sc.(*Physics*) degree from the University of Kerala in 1990. Obtained the M.S.(*Physical Sciences*) from Birla Institute of Technology and Science, Pilani (Rajasthan) in 1993. Joined Material Division, National Physical Laboratory, New Delhi in 1991.

List of Publications

1. M. N. Kamalasanan, N. Deepak Kumar and Subhas Chandra, *J. Appl. Phys.* 74, 5579(1993).

2. M. N. Kamalasanan, **N. Deepak Kumar** and Subhas Chandra, *J. Appl. Phys.* 74, 679(1993).

3. M. N. Kamalasanan, **N. Deepak Kumar** and Subhas Chandra, *J. Appl. Phys.* 76, 4503(1994).

4. M. N. Kamalasanan, **N. Deepak Kumar** and Subhas Chandra, *J. Mater. Sci.* (Communicated).

5. U. Narang, P. N. Prasad, F. V. Bright, K. Ramanathan, **N. Deepak Kumar**, B. D. Malhotra, M. N. Kamalasanan and Subhas Chandra, *Anal. Chem.* 66, 3139(1994).

6. U. Narang, P. N. Prasad, F. V. Bright, A. Kumar, **N. Deepak Kumar**, B. D. Malhotra, M. N. Kamalasanan and Subhas Chandra, *Chem. Mater.* 6, 1596(1994).

7. **N. Deepak Kumar**, M. N. Kamalasanan and Subhas Chandra, *Appl. Phys. Lett.* 65(11), 1373(1994).

8. **N. Deepak Kumar**, M. N. Kamalasanan and Subhas Chandra, *J. Mater. Sci.* (Communicated).